PHOTOASSOCIATION OF ULTRACOLD ATOMS

Marius Lysebo

Thesis submitted for the degree of Master of Science

Department of Physics
University of Oslo

May 2006

Acknowledgements

After five years as a student at the physics department, I would like to take this opportunity to thank some of the people that are responsible for making these years enjoyable.

All students at the theory group that I have shared room with for the past two years deserves thanks for creating a good environment to work in. I also want to mention some of the great lecturers at the physics department; *Jon Magne Leinaas* for his course in non-relativistic quantum mechanics (FYS4110), *Morten Hjorth-Jensen* (FY102) and *Finn Ravndal* (FYS3110) for their courses also in quantum mechanics, *Øyvind Grøn* for his thorough and detailed lectures on general relativity (FYS4160) and *Yuri Galperin* for teaching me statistical mechanics (FYS3130) in his hard but rewarding manner.

My fellow student, Ken Tore Tallakstad deserves thanks for all the hours he put into proofreading this thesis, and for his useful input. Our close collaboration during several courses has also been appreciated.

Last but not the least, I would like to thank my supervisor prof. Leif Veseth for accepting me as a student and for all his comments and suggestions along the way. He has been a source of inspiration both as a supervisor during the last two years, but also as a lecturer with his fine lectures in both FYS2160 (thermodynamics) and especially FYS3140 (mathematical methods in physics) before that.

Marius Lysebo
Blindern, May 2006

Contents

Chapter 1

Cooling atoms and molecules

THis chapter is an introduction to the field of cold atoms and molecules. The formation of cold molecules will occupy much of this thesis and is the main subject throughout, our treatment of cold atoms will be less thorough and serve only as an introduction. Methods to cool and trap atoms are presented in section 1, while an introduction to cold molecules is provided in section 2.

To avoid any misunderstandings to the reader unknown to this field, let me emphasize that the word cold in the following is used differently from the everyday meaning of the word. Cold atoms and molecules have temperatures in the vicinity of $1\mathrm{K}$. This corresponds to temperatures of about $-272^{\circ}\mathrm{C}$, temperatures that are unknown to all of us in every day life. In this thesis and also in this chapter, atoms and molecules cooled to temperatures as low as $1\mathrm{nK}$, one milliard Kelvin above the absolute zero ($-273.15^{\circ}\mathrm{C}$), will be discussed.

As $T \rightarrow 0$, physical phenomena not seen at higher temperatures such as Bose-Einsten condensation appears. The study of this new cold physics and the increased accuracy possible in measurements for cold systems, are the main motivations for the ongoing search for increasingly cold atoms and molecules.

1.1 Cold atoms

The 1997 Noble prize in physics was awarded Steven Chu, Claude Cohen-Tannoudji and William D. Phillips for developing methods to cool and trap atoms with laser light. In this brief introductory section we present some of the different methods they worked with both theoretically and experimentally through the 80's and the 90's. All of these methods takes advantage of the interactions between atoms and photons to cool atoms to $\mu\mathrm{K}$ temperatures, and even further down to nK temperatures by evaporative cooling.

The atomic cooling methods are important also to cold molecule production since cold atoms play a key part to several of the molecular cooling methods described in later chapters. This is not so much because the methods used to cool atoms and molecules are the same, but because the basis of many cold molecule experiments are in fact cold atoms. As we will see in chapters to come, both photoassociation- and Feshbach molecules uses pre-cooled atoms as a starting point. Thus, for a complete picture of the molecular cooling techniques, the atomic cooling methods are relevant.

The theory behind atomic cooling is also rewarding in the sense that it represents a very

accessible theory, that can be understood by fundamental physical laws. For a deeper understanding several branches of physics are needed, both quantum mechanical effects and statistical mechanics are important. However, in this chapter we try to keep it simple. A full in dept treatment would easily fill the next 100 pages. As I will do throughout this chapter, I refer to two books on the subject: 1) *Atomic physics* by C. J. Foot [2] and 2) *Laser Cooling and Trapping* by H. J. Metcalf and P. van der Straten [3] for further details.

We start by considering the Doppler shift since in many ways the Doppler shift has a leading part (shared with the laser) in cooling and trapping atoms.

1.1.1 Doppler shift

The *Doppler shift* causes the frequency of light to shift when observed from reference frames moving with different velocities relative to each other. This has to be taken into account when studying for example the frequency of emitted light from an atom.

Consider a laboratory system and yet another reference system with speed v along the x-axis of the laboratory system. Imagine radiation with frequency ν being sent out in the laboratory system along the x-axis and observed in the moving system. The frequency seen in the moving system ν' will be shifted. The frequency shift is given by

$$\nu' = \nu\left(1 \pm \frac{v}{c}\right). \tag{1.1}$$

ν' is shifted upwards relative to ν when v is in the opposite direction of the propagating photons, and ν' is shifted downwards when v moves in the same direction as the photons. We may also write

$$\omega' = \omega - \mathbf{k}\cdot\mathbf{v}, \tag{1.2}$$

with $\mathbf{k}$ as the wave vector (for the light) and $\mathbf{v}$ as the velocity of the moving reference frame we are observing from. ω is defined as usual, $\omega \equiv 2\pi\nu$. Often we will attach the moving reference frame to the atom and $\mathbf{v}$ will then be equal to the atomic velocity. The Doppler shift plays a crucial part in exerting radiation pressure to slow and cool atoms, as will be apparent in sections to come.

1.1.2 Slowing atoms with photons

Let us consider atoms coming out from an atomic oven, and interacting with the photons in a laser beam (see figure 1.1, with the atomic source to the left, atoms in blue and the laser light illustrated as three coherent red waves). The atoms are all of the same kind and the laser frequency match the energy gap between two internal levels, $|1\rangle$ and $|2\rangle$. When a photon is absorbed the atom is excited into $|2\rangle$. Depending on the lifetime of this level, the atom will after some time return to $|1\rangle$ by spontaneous emission. When an atom absorbs a photon, momentum conservation requires the atom to be decelerated[1]

$$h\frac{\nu}{c} + mv = mv' \Rightarrow \Delta v = \frac{h\nu}{mc}. \tag{1.3}$$

[1]It is important that the photons in the laser beam and the atoms moves in opposite directions, otherwise the atoms will be heated by the opposite effect.

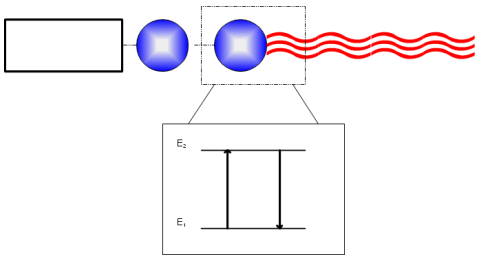

Figure 1.1. *Atoms effusing from an oven, absorbing light from a laser beam directed in the opposite direction. The atom returns to the ground state by spontaneous emission.*

Δv is the change in speed, m is the atomic mass, c is the speed of light while h is the Planck constant. The momentum change will be the same for spontaneous emission, but since this happens in all directions, the momentum changes due to spontaneous emission tend to cancel each other out. The whole process is limited by the rate of spontaneous emission, since an atom must absorb a significant number of photons to be slowed. This is seen from equation (1.3), since Δv will have to be small. The maximum rate of spontaneous emission is related to the natural lifetime τ of an exited level. If radiated with intense laser light, the populations in $|1\rangle$ and $|2\rangle$ will become equal, and the maximum rate of spontaneous emission will be $\frac{1}{2} \cdot \frac{1}{\tau}$. Thus, the maximum acceleration (retardation) is found to be

$$a_{\max} \simeq \frac{\Delta v}{\tau} = \frac{h\nu}{mc\tau}. \tag{1.4}$$

The magnitude of this acceleration is very large, for example with sodium atoms it is as large as $9 \times 10^5 \mathrm{m/s}^2$.

1.1.3 Zeeman cooling

There exists complication to the simple idea presented in the previous section. A fixed laser frequency will not be sufficient. This is because of the Doppler shift that brings the laser frequency out of resonance as the velocity is changed. Perhaps the most obvious way to correct this would be to continually tune the laser frequency, this is known as Chirp cooling. Here we present another method that utilizes the Zeeman effect. This so called Zeeman cooling, uses a varying magnetic field $\mathbf{B}(z)$ to Zeeman shift levels $|1\rangle$ and $|2\rangle$ into resonance, see figure 1.2.

The magnetic field used may be of the form

$$\mathbf{B}(z) = B_0 \left(1 - \frac{z}{L_0}\right)^{1/2} \mathbf{k}, \tag{1.5}$$

with L_0 as the length of the solenoid and B_0 as the magnetic field strength at $z = 0$ (where the atoms enter the solenoid). The interaction between this B field and the atom is given by

$$\hat{H} = -\hat{\boldsymbol{\mu}} \cdot \mathbf{B}(z) \tag{1.6}$$

with $\boldsymbol{\mu}$ as the atomic magnetic moment with both spin and orbital contributions. The Zeeman shift can be found to be

$$E_z = g_J \mu_B B(z) M_J, \tag{1.7}$$

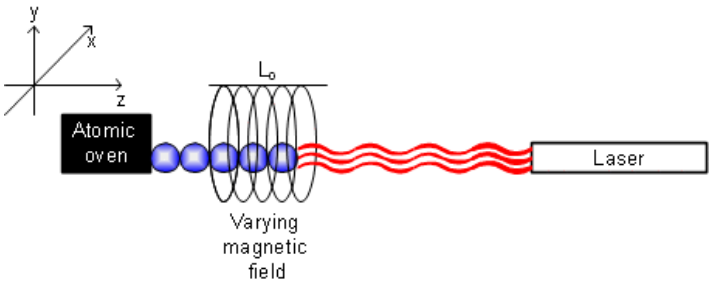

Figure 1.2. *A solenoid is used to set up a spatially varying magnetic field. The atomic levels are Zeeman shifted so that the effects of the Doppler shift is canceled for all v below a limiting velocity v_0. Depending on the magnetic field, the atoms can either come to a complete stop within the solenoid or come out with a small velocity.*

with g_J as the Lande' g-factor given by

$$g_J = \frac{3}{2} + \frac{S(S+1) - L(L+1)}{2J(J+1)}. \tag{1.8}$$

In equation (1.8) it has been assumed that $g_s = 2$. The main idea behind Zeeman cooling can now be summarized with the equation

$$\hbar\omega_0 + \Delta E_z = \hbar\omega + kv. \tag{1.9}$$

On the left side is the resonance energy plus the energy shift caused by the Zeeman shift. On the right side we have the laser energy plus the contribution kv from the Doppler shift. The interpretation of equation (1.9) becomes especially simple if $\omega = \omega_0$. In this case the Zeeman shift should equal the Doppler shift at all times. This is made possible by the varying magnetic field $\mathbf{B}(z)$, reducing the Zeeman shift at the same rate as the Doppler shift. By this mechanism the atoms will, for as long as they are in the solenoid, be kept in resonance with the laser frequency.

Zeeman cooling is of course not a possible method to use if the two levels considered, $|1\rangle$ and $|2\rangle$, have equal Zeeman shifts, since ΔE_z will be zero in this case.

In any experiment involving Zeeman cooling there exists a critical speed v_0, determined by the magnetic field. Atoms with initial velocities $v < v_0$ will be shifted into resonance by the Zeeman shift (atoms with speeds $v < v_0$ will travel a bit down the solenoid before having their speeds reduced). Atoms with speeds $v > v_0$ will not be decelerated, since they will be out of resonance when entering the solenoid, and never be Zeeman shifted into resonance. Because of this the fastest atoms will escape, and the final velocity distribution will be sharply peaked around a low velocity. This final velocity is determined by the magnetic field.

1.1.4 Optical molasses technique

We now consider the slightly more complicated situation where atoms are moving in a gas. This is a much more chaotic situation than what has been considered so far. Luckily the solution is in principle not very complex. It turns out that by using six laser beams that

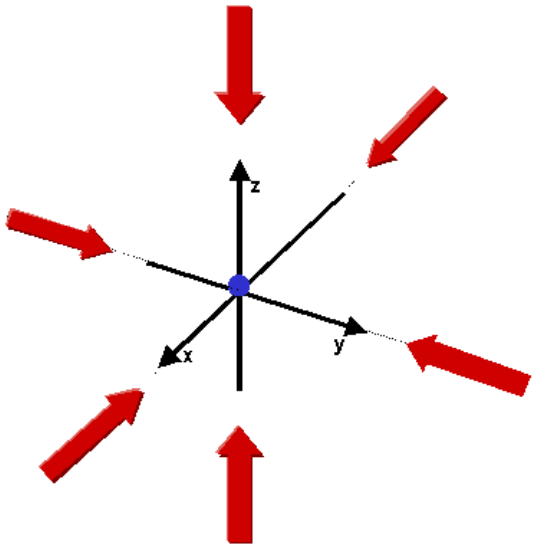

Figure 1.3. *Three pairs of counter propagating laser beams affect moving atoms with a damping force opposite to the atomic velocity* $\mathbf{v}$*. The lasers are illustrated as red arrows. Their frequency is tuned below the resonance frequency.*

makes up standing waves in three orthogonal directions, it is possible to achieve cooling also in a gas. See figure 1.3 for a sketch of the setup.

The frequency on the laser beams are crucial. They need to be tuned below the atomic resonance frequency. To see why, consider first a stationary atom. The symmetry of the laser beams arrangement indicates that there can be no net force on a stationary atom. Consider now an atom moving with velocity $\mathbf{v}$. Because of the Doppler shift, photons propagating in the direction opposite to $\mathbf{v}$ will be observed with a higher frequency than photons moving in the same direction as $\mathbf{v}$, when observed in a reference frame attached to the atom. Since the photons have a frequency tuned below resonance, photons moving in the opposite direction to $\mathbf{v}$ will be observed in the atomic system with a frequency closer to resonance than photons moving parallel to $\mathbf{v}$. This is because of the Doppler shift. The probability of absorbing a photon with momentum directed in the opposite direction of $\mathbf{v}$ is thus enhanced. The result is a net force acting on the atoms in the opposite direction of the atomic velocity $\mathbf{v}$. This setup is usually called optical molasses ("optisk sirup"), and the force acting on the atoms can be written as [2]

$$\mathbf{F}_{\text{om}} = -\alpha \mathbf{v}. \tag{1.10}$$

α is a constant that may be calculated, see [2].

The optical molasses setup is usually not considered a trap since there is no restoring force acting on an atom at rest.

1.1.5 Doppler cooling limit

A fundamental question is whether or not there exists a lowest attainable temperature for cooling experiments, in other words a lower temperature one can not cool beyond. The

answer to this is that no such limit exists, besides $T = 0$ of course. However, the cooling methods investigated so far that rely on scattering of photons has a lower reachable limit. This is the so called Doppler cooling limit.

When an atom is scattering photons it will be decelerated as we have seen. We must however not forget that there will be a heating effect, an acceleration, from recoil in the emission and absorption processes. This is of no importance before the atoms are cooled to temperatures were the recoil speed is of the same order as the atomic speed. When this happens, the system settles down to equilibrium, where the heating is comparable to the cooling.

For each absorption process the atom experiences a change in momentum by $\Delta p = \hbar k$, from which it follows a recoil kinetic energy of $\Delta E = \frac{(\Delta p)^2}{2m} = \frac{\hbar^2 k^2}{2m} = \hbar\omega_r$. This recoil energy is the same also for the emission process. This again implies that the light field looses an energy amount of $2\hbar\omega_r$ for each scattering event. This energy lost from the light field is converted into kinetic energy for the atom, through the scattering process. This represents heating that competes with the cooling, and at steady state the heating must equal the cooling. Once again I refer to [2] for details. However, the result that emerges from these consideration is the Doppler cooling limit

$$\boxed{k_B T_D = \frac{\hbar\Gamma}{2}}. \tag{1.11}$$

T_D represents the cooling limit for experiments that rely on the Doppler shift to cause radiation pressure. $\Gamma = \frac{1}{\tau}$ is the spontaneous emission rate and τ is the natural lifetime of level $|2\rangle$.

For over ten years, scientists doing laser cooling experiments with atoms believed this to be the lowest attainable temperature. However, in 1988 Lett *et al.* published a paper [4] where they reported cooling below the Doppler limit. This was achieved for a gas of sodium atoms using the optical molasses technique. In this experiment they measured the temperature to be as low as $43 \pm 20\mu$K, while the theoretical limit, T_D, was calculated to be about 240μK. They had no explanation as to how this could , this *sub-Doppler* cooling was later explained by Dalibard and Cohen-Tannoudji [5]. Part of their explanation is the Sisyphus cooling mechanism. See for example [2].

1.1.6 The magneto-optical trap

The magneto-optical trap (MOT) is basically an optical molasses arrangement with a magnetic field. The magnetic field is used in addition to create a trap, and is inhomogeneous but time independent. The magnetic field is set up by two coils with currents I. The magnetic field induces a restoring force on the atoms, directed towards the origin. See figure 1.4 for a crude illustration of the MOT setup.

An atom with magnetic moment $\boldsymbol{\mu}$ will in a magnetic field have potential energy $V = -\boldsymbol{\mu} \cdot \mathbf{B}$. Because of this, atoms will experience a force, $\mathbf{F} = \nabla(\boldsymbol{\mu} \cdot \mathbf{B})$. In the MOT this force is directed towards the origin. To see why, consider the Zeeman shift along the z-axis and examine the $J = 1 \rightarrow J = 0$ transition. $\mathbf{J} = \mathbf{L} + \mathbf{S}$ with $\mathbf{L}$ as angular moment and $\mathbf{S}$ as spin. In the $J = 1$ level there exists three sub levels with quantum numbers $M_J = \pm 1$ and $M_J = 0$. The Zeeman shift

$$E_z = g_J M_J B(z)\mu \tag{1.12}$$

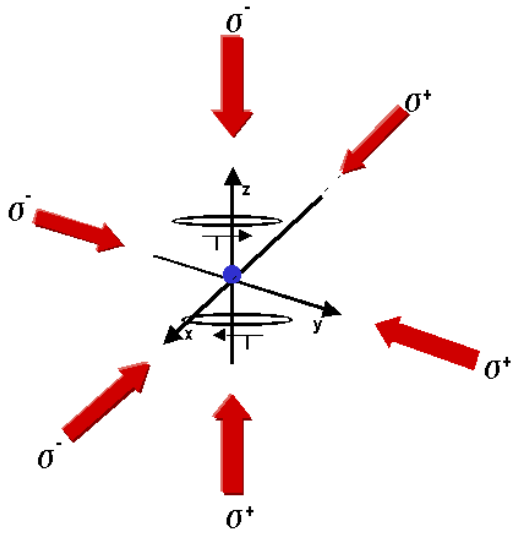

Figure 1.4. *Two coils with currents I running in opposite directions are placed along the z-axis. This induces a force on the atoms directed towards the origin. The laser beams decelerates the atoms by the same mechanism as in the optical molasses. The magnetic field causes atoms to accumulate at the origin. The laser beams needs to have a specific polarization, for reasons discussed in the text. σ^+ and σ^- denotes respectively right handed and left handed polarization.*

increases the energy of the $M_J = 1$ level when $B(z) > 0$. The energy shift increases with magnetic field. In the $M_J = -1$ level the situation is reversed, and the energy is lowered with increasing magnetic field $B(z)$. In the $M_J = 0$ level there is no Zeeman shift. Further, light with right handed polarization has the selection rule $\Delta M_J = 1$, while light that have left handed polarization has the selection rule $\Delta M_J = -1$. It can also be shown that the quadruple magnetic field used in the MOT increases linearly for small distances from the origin along the z-axis [3]. Thus, an atom placed a distance from the origin along the z-axis will interact more with the σ^- beam than the σ^+ beam. Because of this there will be a net force towards the origin. Figure 1.5 sums up the discussion.

The force acting on an atom in a MOT can be found to be [3]

$$\boxed{\mathbf{F}_{\text{MOT}} = -\alpha\mathbf{v} - \kappa\mathbf{r},} \tag{1.13}$$

with α and κ as constants. α and κ are different for different MOTs and for different atomic species. We may observe that the first term is equal to the force in the optical molasses, while the last term gives a restoring force towards the origin also if $\mathbf{v} = \mathbf{0}$.

Equation (1.13) is often compared with the damped harmonic oscillator, since it can be written

$$\ddot{\mathbf{r}} + \frac{\alpha}{m}\dot{\mathbf{r}} + \frac{\kappa}{m}\mathbf{r} = 0, \tag{1.14}$$

with m as the atomic mass. One may identify the factor κ as a damping factor equivalent to the spring constant in classical mechanics. The typical for a MOT is to have an overdamped motion with an oscillation frequency of a few Hertz.

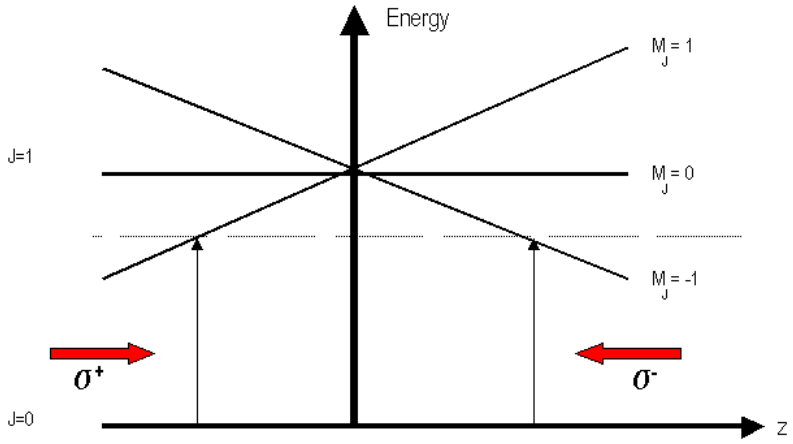

Figure 1.5. *The principle of a MOT. The laser beams has a frequency $\omega < \omega_0$ shown as the dotted horizontal line. An atom is placed at the positive z-axis and absorption from the laserbeam with σ^- polarization is thus enhanced. This induces $\Delta M_J = -1$ transitions. For an atom placed at the negative z-axis, the same is true, but now it is $\Delta M_J = +1$ transitions that are induced.*

The steady-state temperature in a MOT may be below the Doppler cooling limit by the effect of Sisyphus cooling. A MOT also captures atoms with much greater velocities then what is possible using the optical molasses technique. Velocities up to $70\mathrm{m/s}$ may be within the capture range of a MOT. In many experiments to produce cold molecules, the MOT is used as a starting point to cool atoms down to temperatures around the Doppler cooling limit. For cooling significantly below the Doppler limit, down to Bose-Einstein temperatures, evaporative cooling must be used.

1.1.7 Evaporative cooling

So far the methods discussed has not been able to cool atoms down to temperatures lower than approximately 1 μK (the so called recoil limit). This is not sufficient for Bose-Einstein condensation (BEC) that requires temperatures in the nK range. To get to these temperatures, evaporative cooling is used. When a Bose-Einstein condensate first was observed in June 1995 [8], evaporative cooling was a necessity.

Evaporative cooling consists of selective removal of the hottest atoms, thereafter the remaining atoms are allowed to thermalize by collisions. By repeating this cycle over and over a significant reduction in temperature may be the result . We can think of this process in terms of the Maxwell speed distribution. In each step the tail of the distribution is removed, making the distribution after thermalization narrower and centered towards lower speeds. Two "cuts" in the speed distribution are shown in figure 1.6. Notice however that although this way of thinking is instructive and describes the process schematically, the use of the Maxwell distribution is not correct since the trapped atoms are not an ideal gas.

Accompanying a reduction in temperature is also an increase in phase-space density[2], this may happen if the volume occupied by the remaining atoms is reduced to an extent that

[2]Phase space density $\rho(\mathbf{r}, \mathbf{p}, t)$ is defined as the probability of finding a single particle in position $\mathbf{r}$ with momentum $\mathbf{p}$ at time t. The phase space density of N particles is the sum of the one particle phase space

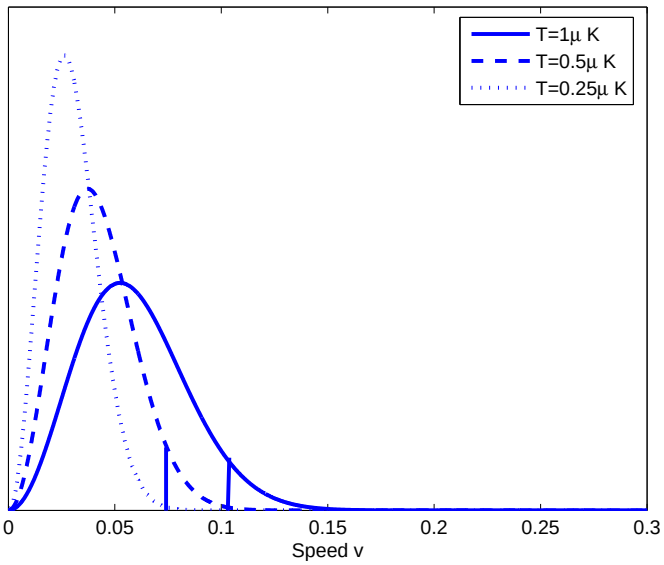

Figure 1.6. *The most energetic atoms are removed from the Maxwell distribution of an ideal gas (solid line) at $T = 1\mu$K. After thermalization the remaining atoms have a left shifted and more narrow distribution. This distribution is again cut to relieve the atoms with the greatest velocities. The resulting distribution is also shown.*

overcompensates for the lost atoms. Eventually, this together with a low temperature may lead to BEC.

The atoms used in evaporative cooling experiments are usually pre-cooled by one of the already mentioned cooling methods and kept in a trap. The removal of the hottest atoms are then achieved by lowering the trap depth, allowing the hot molecules to escape from the trap [3]. The lowering of the trap depth can be done in steps or continually, in the last case the process is sometimes called *forced* evaporative cooling.

Model of the evaporation process

The theory used to describe the evaporative process here is based on a model presented in [6]. The evaporative cooling is described as a discrete process. The trapping potential is lowered in discrete steps with thermalization of the remaining atoms in the trap before lowering the potential further. Assume a trapping potential of the form

$$U(x,y,z) = a\left|\frac{x}{L_x}\right|^{s_1} + b\left|\frac{y}{L_y}\right|^{s_2} + c\left|\frac{z}{L_z}\right|^{s_3}, \tag{1.16}$$

densities divided by N. $\rho(\mathbf{r},\mathbf{p},t)$ is normalized so that

$$\int \rho(\mathbf{r},\mathbf{p},t)\mathrm{d}^3r\mathrm{d}^3p = 1. \tag{1.15}$$

[3] All readers should visit *http://www.colorado.edu/physics/2000/bec/evap_cool.html* for a game of evaporative cooling.

with L_x, L_y and L_z as the length of the trap in each direction, a, b and c are constants. Define a parameter ξ

$$\xi \equiv \frac{1}{s_1} + \frac{1}{s_2} + \frac{1}{s_3}. \tag{1.17}$$

It can be proven, [7], that the volume occupied by the trapped atoms are

$$V \propto T^{\xi}. \tag{1.18}$$

We now consider one evaporative step. The potential is lowered to $\eta k_B T$, the value on η (the so called cutting parameter) determines the height of the potential. Atoms with energies above $\eta k_B T$ are lost. The remaining atoms are allowed to thermalize in an infinitely high potential. We now introduce two very central parameters in this model

$$\nu \equiv \frac{N'}{N}, \qquad \gamma \equiv \frac{\log(T'/T)}{\log \nu}, \tag{1.19}$$

with primed quantities indicating values after the potential is lowered and thermalization has taken place. N is the number of atoms, T is temperature. Other central quantities can be found in terms of γ and ν, we summarize

$$T' = T\nu^{\gamma}, \qquad N' = N\nu, \qquad V' = V\nu^{\gamma\xi}, \tag{1.20}$$

$$n' = n(1-\gamma\xi), \qquad \rho' = \rho\nu^{1-\gamma(\xi+3/2)}, \qquad k' = k\nu^{1-\gamma(\xi-1/2)}. \tag{1.21}$$

$n \equiv \frac{N}{V}$, ρ is the phase space density and k is the elastic collision rate. ν and γ can be calculated from

$$\nu = \frac{\Gamma_{\text{inc}}(\xi+3/2,\eta)}{\Gamma(\xi+3/2)}, \qquad \gamma = \frac{\log(\overline{\epsilon}'/\overline{\epsilon})}{\log \nu}, \tag{1.22}$$

with

$$\bar{\epsilon} = \xi + \frac{3}{2}, \qquad \bar{\epsilon}' = \frac{\Gamma_{\text{inc}}(\xi+5/2,\eta)}{\Gamma_{\text{inc}}(\xi+3/2,\eta)}, \tag{1.23}$$

where $\bar{\epsilon}$ is the total average energy of the atoms divided by $k_B T$. Γ is the usual gamma function while Γ_{inc} is the incomplete gamma function[4]. Obtaining equations (1.22) and (1.23) are far from trivial and we will not attempt this here. See [3] and [6] for details.

In figure 1.7 we investigate one evaporative step and plot key quantities such as temperature, number of atoms, phase space density and elastic collision rate as a function of the normalized cutting parameter η''. η'' is related to η by

$$\eta'' = \frac{\eta}{\bar{\epsilon}} = \frac{\eta}{\xi+3/2}. \tag{1.24}$$

By plotting against this parameter we are measuring energy in units of the average total energy $\bar{E} = \bar{\epsilon} k_B T = (3/2+\xi) k_B T$. In figure 1.7 we investigate two trapping geometries, the 3D harmonic trap and the 3D linear trap with $\xi = 3/2$ and $\xi = 3$ respectively. From figure 1.7 we see minor differences in temperature and number of atoms for the different trapping geometries. For the phase space density and elastic collision rate there are significant differences. A large elastic collision rate is important to speed up the cooling process, and it

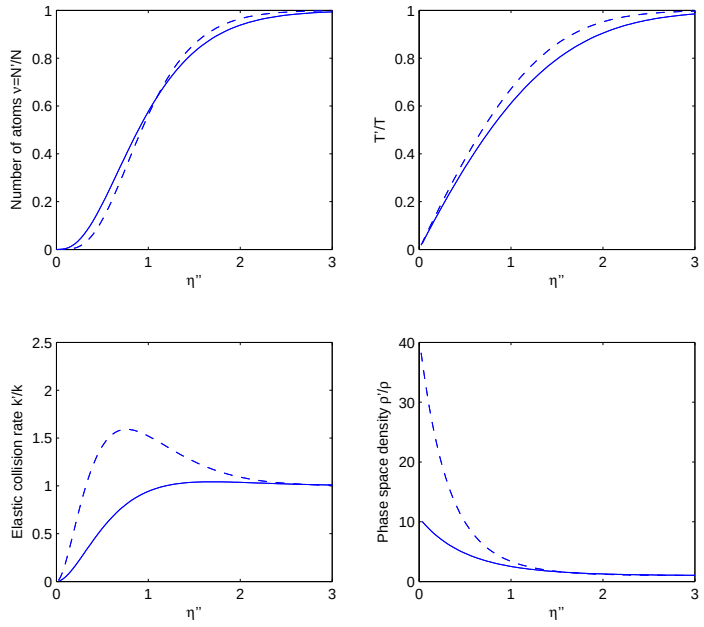

Figure 1.7. *Key quantities to evaporative cooling. The dotted lines are plotted with* $\xi = 3$ *wile the solid lines are plotted with* $\xi = 3/2$.

is also important that the collision rate does not decrease for all η since this indicates that the cooling process eventually stops. Figure **??** certainly indicates that a linear potential is to prefer over a harmonic one, and this is also one of the findings in [7].

Using a trapping potential for which ξ is large enough so that the evaporative process does not stop, one might think, based on our discussed model, that the evaporative cooling process can go on forever without any lower limit. This is however not true. We have made an error by not considering inelastic collisions, this error becomes more significant as the temperature is lowered. This is because the inelastic collision rate is independent of speed while the elastic collision rate depends on speed. As the inelastic and elastic collision rates become equal the cooling process stops. For alkali atoms the elastic cross sections are large, and temperatures down to $1n$K may be obtained.

1.2 Formation of cold molecules

We have seen how atoms can be cooled and trapped and now we shift our focus to consider molecules. The rest of this thesis will in different ways consider the realization of cold molecules. The term *cold* will be used to describe temperatures of a couple of Kelvin and below, while *ultra*cold is reserved for temperatures below 1μK. Be aware that it is also common to reserve the word cold for temperatures below 1K.

We will throughout have our main-focus directed towards how the cold and ultracold

[4]Defined as $\Gamma_{\text{inc}}(a,x) \equiv \int_x^\infty t^{a-1}e^{-t}dt$.

molecules can be created, and not so much their properties once they are formed. In the very last chapter we will however also touch this subject, then dominantly in a qualitative way.

This section serves two purposes. 1) It is as a general introduction to cold molecules, 2) it describes some of the different cooling techniques that exists for molecules, but that are not investigated further in the next chapters. We limit ourselves to neutral molecules in the following. Production of cold and ultracold molecules with photoassociation and through Feshbach resonances are treated in chapters 3 and 6 respectively, and are therefore *not* included in this section. The four cooling techniques described here have all recently been successfully implemented and are currently being further developed by different groups worldwide. The reader should however be aware that there exists many more cooling proposals than what can be presented here.

At the end of this chapter we compare the different cooling methods. Included in this comparison is also cold molecule production by photoassociation and Feshbach resonances.

We begin by motivating the search for cold and ultracold molecules.

1.2.1 Why cold molecules?

The intensive search for cold molecules is motivated by several new possibilities in the cold and ultracold temperature regime.

- The possibility of obtaining new/more precise spectroscopic information. Cold molecules have significantly reduced Doppler shifts, making precise measurements possible. Cold molecules are also used in the search for an electric dipole moment. In the feature, as colder molecules are produced, the upper limit on the dipole moment will either be reduced or a finite dipole moment will be found.
- Realization of a molecular (BEC). This requires very low temperatures, obtainable only by Feshbach resonance molecules. See also chapter 6.
- A phase transition from a BEC to a superfluid phase is observed at sub-Bose-Einstein temperatures. This is again treated in more detail in chapter 6.
- Quantum computing. Cold molecules may be used as q-bits in a quantum computer.
- Interferometry with molecules.
- Molecule lasers.

There may also be cold effects and physics yet unknown to us, waiting to be exposed at low enough temperatures. Cold molecules and cold atoms have also paved the way for a new field, namely cold chemistry.

1.2.2 Laser cooling

What makes cooling of molecules more than an extension of the methods that already exists for atoms, is the fact that laser cooling is not an option. This may be surprising since we have seen that laser cooling has been used with great success for atoms. It would therefore be natural to explore this possibility also for molecules. However, laser cooling has proven hard or impossible to implement for most molecules. The main reason for this is the much

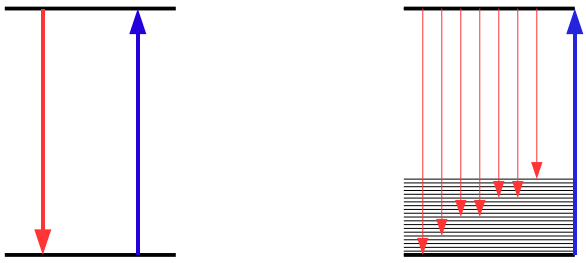

Figure 1.8. *The simple two level closed cycle in atoms (to the left) together with the much more complex internal structure of a molecule (to the right). Laser light tuned to match the energy difference between two states excites (blue arrow) the atom/molecule. The decay (red arrows) can populate a number of internal levels in a molecule. Thus, only a fraction of the population will return to the initial level to be re-pumped.*

more complex internal structure of the molecules, opposed to the atoms. Remember that when scattering of photons were used to cool atoms we relied on an effective two level system, a closed cycle between the ground state and an excited state. With molecules we may still populate an excited state by the use of a laser, the decay will however be spread out to a series of levels. Thus, it is very hard to obtain an effective two level closed cycle that can be used for laser-cooling molecules. See also figure 1.8.

Proposals do however exist for laser-cooling certain molecules, and work is currently ongoing to find new laser cooling schemes applicable also for molecules [10]. It is however my understanding that this, at present time, seems like a dead end. Does this mean that we can not utilize the methods that were so successful in cooling atoms at all? No, it does not. Cold atoms may be used as a starting point for the making of cold molecules, this is accomplished by letting the cold atoms form (cold) molecules. This is indeed the principle behind both photoassociation and Feshbach resonance molecules. What separates these two methods is the mechanism for coupling the two atoms to a molecule. In photoassociation a laser is used while Feshbach molecules are formed using a magnetic field.

1.2.3 Buffer gas cooling

Buffer gas cooling can be used to cool about any molecule as long as the molecule does not dissociate because of collisions with the buffer gas. The idea behind this type of cooling is to elastically collide the molecules with a cold gas, the so called buffer gas. In these collisions the molecules dissipates energy and is therefore slowed and cooled.

The molecules are introduced into a chamber with the buffer gas present, figure 1.9. It is important that the number of collisions with the buffer gas is sufficient to slow the molecules significantly before hitting the walls, otherwise molecules may stick to the walls. Most used as a buffer gas is Helium, both isotopes ^{3}He and ^{4}He have been used. ^{4}He has the advantage of yielding lower temperatures than ^{3}He, and temperatures may typically be in the mK range. The Helium isotopes are especially suitable because of their high vapor pressures also at low temperatures.

We assume in the following m to be the mass of the buffer gas atoms, and M to be the mass of the molecules that are to be cooled. It is possible to calculate the difference in temperature before and after a collision ΔT (for the molecule) [9]

$$\Delta T = \alpha(T_i - T_b), \tag{1.25}$$

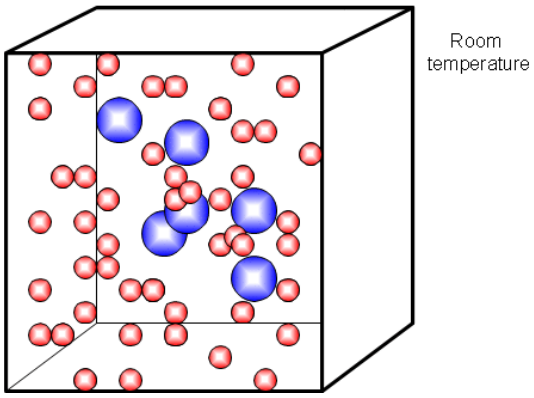

Figure 1.9. *Buffer gas (red atoms) cools the blue molecules through elastic collisions. A real experimental setup is much more complex. All real setups involves a device called a cryostat that maintains a low temperature on the buffer gas. Outside the box we may have room temperature.*

with

$$\alpha = \frac{2Mm}{(M+m)^2}, \tag{1.26}$$

and T_b as the temperature of the buffer gas and T_i as the initial temperature of the molecules. Equation (1.25) is found by considering momentum and energy conservation and by thermal averaging. It is assumed elastic collisions. Further, the temperature after n (elastic) collisions can be found to be [9]

$$T_n = (T_i - T_b)e^{-n\alpha} + T_b. \tag{1.27}$$

The limiting temperature is of course the buffer gas temperature T_b (as $n \to \infty$). This temperature can not be reduced without reducing the density of the buffer gas, something that has consequences. This is because the density of the gas is important to ensure that the molecules collide with a sufficient number of atoms before hitting the walls. T_b must therefore also be chosen with this in mind.

Buffer gas cooling has advantages opposed to other molecular cooling techniques. There are practically no limitations as to which molecules that can be cooled. Other cooling methods may rely on optical transitions or a resonance to work, this is not the case with buffer gas cooling. In fact, the whole Maxwell distribution can be loaded in and cooled directly. This enables the production of many more molecules than by other methods.

The downside is the experimental setup. This is technically complicated, and these complications becomes more severe as the temperature is lowered. Unfortunately this means that the buffer gas cooling method looses out to other cooling techniques. since it is unable to produce molecules with ultracold temperatures. To the best of my knowledge, buffer gas cooling has never been able to cool molecules below $1\mathrm{mK}$ (April 2006).

1.2.4 Stark deceleration

Stark deceleration is a quite general cooling method that works for all polar molecules (molecules with electrical poles). The method is based on the interaction between the molecular dipole moment and electric fields. By letting a molecule pass through a series of rods setting up varying electric fields between them, it is possible to bring the molecule to a near stand still.

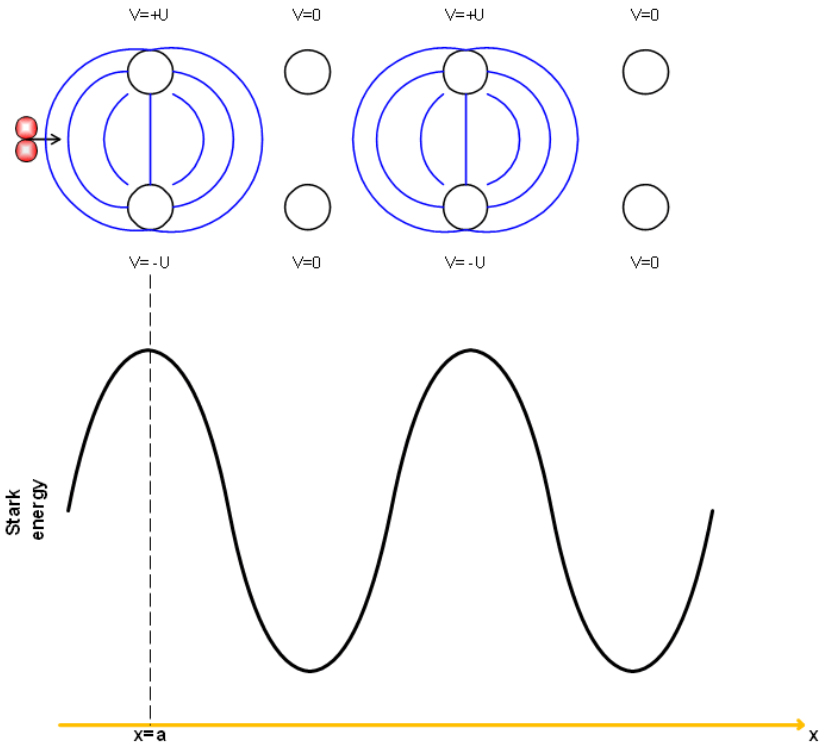

Figure 1.10. *Operation principle for the Stark decelerator. The molecule is shown as two red spheres entering the electric field between two rods. The Stark energy is also plotted with maximum values corresponding to positions with maximum electric fields. See the text for a discussion.*

The reason for this is the Stark effect which in ceratin appropriate quantum states may turn kinetic energy into Stark energy or potential energy when subjected to an electrical field. When entering an electrical field the speed is thus reduced as the kinetic energy is converted into potential energy. When the electric field is gradually turned off the potential energy is lost and converted back into kinetic energy, leaving the speed unchanged after passing the electric field. If however the electric field is switched off suddenly, the kinetic energy that has been converted into potential energy will be lost. A series of these sudden electric field changes is the main principle exploited to cool molecules in a Stark decelerator.

In a Stark decelerator a series of $\simeq 100$ pair of rods are used. Figure 1.10 tries to explain the mechanism. In the figure the rods are pointing into the paper with the circular ends drawn. We number each pair of rods with a number 1 to 100 from left to right. Pair of rods number $1, 3, 5 \ldots$ are connected together with equal voltage applied on each pair. Pair number $2, 4, 6 \ldots$ are also connected with the same voltage applied. However, either the even numbered rods or the odd numbered rods will be grounded at a given time. Voltage is never applied to all rods at the same time.

Consider now the situation in figure 1.10. When the molecule illustrated reaches the position $x = a$, the pair of rods with voltage $V = \pm U$ (pair number 1 and 3 in the figure, numbering from left to right) will be turned off. At the same time the pair number 2 and 4 in figure 1.10 will be turned on. As the molecule reaches the next rod, the same procedure is repeated. By this mechanism, the molecules always travel uphill in the Stark energy, and

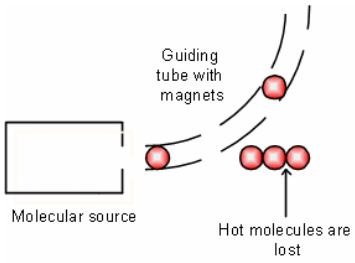

Figure 1.11. *Sketch of the velocity selection process. Magnets guide the molecules with small speeds through a tube. Hot molecules moves to quickly to be deflected and are lost.*

kinetic energy is constantly lost.

Maybe surprisingly this method was not experimentally demonstrated until 1999 when a pulse of CO molecules were slowed from 225 $\mathrm{m/s}$ to 98$\mathrm{m/s}$. It is sometimes emphasized that the narrowing of the Maxwell distribution is not accomplished by the Stark decelerator. The narrowing of the distribution is instead a result of the selection process, choosing molecules with a certain speed to form the beam sent into the Stark decelerator. Because of this, Stark deceleration is sometimes not defined as a cooling method. The definition most often used defines a cooling method as a technique that both center the Maxwell distribution towards lower velocities *and* makes it narrower.

1.3 Velocity selection

Velocity selection is perhaps a less used and less known method than the two presented so far. The idea is to select the slowest moving molecules in the speed distribution. We know that in a gas kept at room temperatures, a small fraction of the molecules will have velocities corresponding to very low temperatures. The main idea is to isolate these molecules.

A simplified sketch of the setup to accomplish this is shown in figure 1.11. The isolation of the slowest moving molecules works by having a molecular vapor source sending molecules into an arrangement of magnets. These magnets form a tube, or are inserted into a tube, to give maximal magnetic fields at the edges of the tube. In the middle of the tube, the magnetic field vanishes or is greatly reduced. Atoms and molecules in a favorable quantum state will then be exposed to a potential set up by the Zeeman shift

$$V = -\boldsymbol{\mu} \cdot \mathbf{B}, \tag{1.28}$$

with $\boldsymbol{\mu}$ as the magnetic moment. The force will be given by

$$\mathbf{F} = -\nabla V, \tag{1.29}$$

and be directed towards the center of the tube for molecules in a Zeeman state where the energy is lowered with decreasing field (a so called low-field-seeking state). For the slowest moving particles effusing from the molecular source, the force in equation (1.29)is sufficient to keep them in the tube, while the hot molecules are lost.

This method is rather easy to use, but as the temperature is lowered the number of molecules produced is drastically reduced. In recent years there has been reported successful cooling of molecules down to a few Kelvin with this method. For further details, see [17].

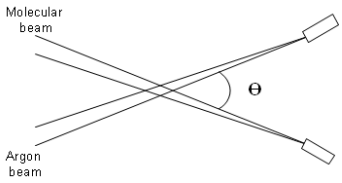

Figure 1.12. *Sketch of the billiard cooling method. The argon atoms and the molecules to be cooled intersects in an angle θ. A real experimental setup is more complex since one typically wants to collect or detect the cooled molecules in some way.*

1.3.1 Billiard cooling

Cooling molecules with billiard like collisions was first proposed and demonstrated by Elioff *et al.* in 2003 [18]. The method relies on a simple idea, *one* collision between a molecule and an argon atom should bring the molecule to a near stand still. This resembles billiard, hence the name billiard cooling. See also figure 1.12.

Any experienced billiard player knows that the angle and the energy in a collision is crucial. So is also the case here. The collision needs to be "tuned" in such a way that the molecule are brought to a complete stop in the laboratory system. There are two parameters we can tune to accomplish this, the energy involved in the collision and the collision angle. We denote the velocity of the center of mass system in the laboratory system for $\mathbf{v}_{\text{cm}}$. The velocity of the molecule in the center of mass system is $\mathbf{u}$ before the collision, and $\mathbf{u}'$ after the collision. We must demand (velocities in the center of mass system is labeled $\mathbf{u}$ and velocities measured in the laboratory system is labeled $\mathbf{v}$)

$$\mathbf{v}' = \mathbf{u}' + \mathbf{v}_{\text{cm}} = \mathbf{0} \tag{1.30}$$

with $\mathbf{v}'$ as the molecular velocity (in the lab. system) after the collision. Primed letters are used for velocities *after* the collision. Equation (1.30) can be used to obtain an expression for the energy and collision angel (subjected to condition (1.30)) [18]

$$E'_{\text{int}} = \left(1 - \frac{M}{m}\right) E_{\text{mol}}, \tag{1.31}$$

with E'_{int} as the energy that must be deposited into the internal modes of the molecule for it to come to a complete stop in the lab. frame. E_{mol} is the kinetic energy of the molecule *before* collision. M is the molecular mass while m is the mass of an argon atom. For the scattering angle, equation (1.30) dictates [18]

$$\cos(\theta_{\text{cm}}) = \frac{E_{\text{Ar}} - E_{\text{mol}}}{\sqrt{\left(E_{\text{mol}} + \frac{M}{m}E_{\text{Ar}}\right)\left(E_{\text{mol}} + \frac{m}{M}E_{\text{Ar}}\right)}}, \tag{1.32}$$

with E_{Ar} as the kinetic energy of the argon atom before collision. This method has been successfully used to produce a great number (10^8) of NO molecules at a temperature below 1K.

1.3.2 Comparison of the different cooling methods

At present time (April 2006) table 1.1 sums up the accomplishments of each of the molecular cooling techniques presented in this thesis. The values in table 1.1 should be representable for all the different techniques.

Method	Number of molecules	Temperature	Molecule	References
Photoassociation	10^6	$\simeq 1\mu$K	Li_2	[11]
	-	150μK	KRb	[20]
	-	100μK	RbCs	[12]
Feshbach resonances	3×10^5	150nK	K_2	[13]
	10^5	30nK	Na_2	[19]
Buffer gas cooling	10^8	400mK	CaH	[14]
	10^{12}	4K	PbO	[15]
Stark deceleration	10^8	30mK	ND_3	[16]
Velocity selection	-	a few Kelvin	H_2CO	[17]
Billiard collisions	10^8	400mK	NO	[18]

Table 1.1. *Known accomplishments for the different cooling methods. In some of the papers the number of molecules created is not explicitly given, this is indicated with -.*

From table 1.1 we see that cold molecule production by photoassociation and Feshbach resonances have temperature advantages, opposed to the other cooling methods. One should however notice that both of these methods, to my knowledge, so far has only been successfully implemented with molecules composed of alkali atoms (both homonuclear and heteronuclear).

For the other cooling methods there seems to be a long way to the μK range, however there are work currently ongoing to improve also these methods. Especially the buffer gas cooling method has attracted considerable interest. One group at Harvard is especially active in this research (see *http://www.doylegroup.harvard.edu/*). From table 1.1 we may conclude that for the alkalis we have methods to cool below BEC temperatures. However, at present time we seem to be without a method to cool any molecule to *ultra*cold temperatures. There are no fundamental reasons why cold molecule production by photoassoication and Feshbach resonances should not work for a general molecule. However, both techniques requires detailed spectroscopic information. This may be hard to obtain for a general molecule, while the alkalis form molecules that are spectroscopically well known.

Chapter 2

Numerical methods

In chapter 3 we want to investigate different photoassociation schemes possible in Li_2. To do this we need to obtain both the electronic states and the vibrational levels of each electronic state. All calculations are done *ab initio*, but the programs used for the numerical calculations are mostly developed by others. This does *not* mean that obtaining the interatomic potential curves are without challenges. Many hours went into this work since the basis set must be chosen with special care.

Three programs have been used to obtain both the electronic states and the vibrational levels. A brief summary of the principles behind each program is presented in what follows. The programming details are not commented at all. Where I have found it appropriate I have included some comments based on my experience with the different programs. In particular I have included a summary of my search for good atomic basis sets.

All results obtained are referred to the next chapter. We begin by simply writing down the Hamilton operator for a diatomic molecule. We are throughout searching for the eigenstates of this operator.

2.1 Equations to be solved

Consider the Hamiltonian for a diatomic molecule

$$\hat{H} = -\sum_{i=1}^{N+2} \frac{\hbar^2}{2m_i}\nabla_i^2 + \hat{V}(\mathbf{r}_A, \mathbf{r}_B, \mathbf{r}), \tag{2.1}$$

$\mathbf{r}_A$ and $\mathbf{r}_B$ are the positions of the two nuclei, while $\mathbf{r} = (\mathbf{r}_1, \mathbf{r}_2, \ldots, \mathbf{r}_i, \ldots \mathbf{r}_N)$ contains positionvectors to the N electrons. m_i is the mass of each particle. Relativistic effects (spin-orbit coupling, spin-spin coupling and so on) are ignored in what follows, but relativistic effects are important to Feshbach resonances that will be considered in chapter 6.

The sum in equation (2.1) is over the N electrons and the two nuclei. By separating the translational movement of the center of mass and using a coordinate transformation it is possible to write, see also [27]

$$\hat{H} = \hat{H}_e(R, \mathbf{r}) + \hat{H}_n(R, \theta, \phi), \tag{2.2}$$

with

$$\hat{H}_e = -\frac{\hbar^2}{2m}\sum_{i=1}^{N}\nabla_i^2 - \frac{\hbar^2}{2(m_A+m_B)}\sum_{i,j=1}^{N}\nabla_i\cdot\nabla_j + \hat{V}(R,\mathbf{r}), \tag{2.3}$$

and

$$\hat{H}_n = -\frac{\hbar^2}{2\mu}\nabla^2_{R,\theta,\phi}. \tag{2.4}$$

R is the internuclear distance, θ and ϕ describes the orientation of the molecular axis. The $\mathbf{r}_i$ vectors, describing the positions of each electron, refers to a coordinate system with origin at the center of mass position and z-axis along the molecular axis. m is the electron mass, while m_A and m_B are the masses of the two nuclei. μ is the reduced mass. The nuclear motion is in equations (2.3) and (2.4) described as one-particle moving at the center of mass position. The wavefunction is within the Born-Oppenheimer approximation written as a product

$$\psi(\mathbf{r},R,\theta,\phi) = \psi_e(R,\mathbf{r})\psi_n(R,\theta,\phi). \tag{2.5}$$

This is motivated by the fact that $\hat{H}_n$ does not contain any electron coordinates. ψ_e and ψ_n must satisfy two *decoupled* equations

$$\hat{H}_e\psi_e(R,\mathbf{r}) = E_e(R)\psi_e(R,\mathbf{r}), \tag{2.6}$$

$$[\hat{H}_n + E_e(R)]\psi_n(R,\theta,\phi) = E_v\psi_n(R,\theta,\phi). \tag{2.7}$$

In the simple Born-Oppenheimer approximation it is assumed that $\langle\psi_e|\hat{H}_n|\psi_e\rangle = \hat{H}_n$ in order to obtain equation (2.7)[1]. Born and Oppenheimer calculated that the effects of this approximation are to neglect terms of order m/μ [32]. However, it turns out that most of these terms can be included in $E_e(R)$ to give the so called adiabatic Born-Oppenheimer approximation.

To find $E_e(R)$ in equation (2.6) we use Hartree-Fock theory along with so called multireferance many-body theory [22], while equation (2.7) is solved using Numerovs method once $E_e(R)$ is known. $E_e(R)$ describes the electronic states and will be referred to as the potential energy or the potential curve. E_v is the energy of the vibrational levels corresponding ta an electronic state $E_e(R)$.

2.2 Hartree-Fock theory

The Hartree-Fock theory plays an important role in quantum chemistry and is often used as a starting point for other more refined methods. This is also the case here, with the Hartree-Fock calculations as a necessary basis for the MultiMOD[2] program.

The Hamiltonian for a diatomic molecule with infinitely heavy nuclei can be written (follows from equation (2.2))

$$\hat{H} = \sum_{i=1}^{N}\left\{-\frac{\hbar^2}{2m}\nabla_i^2 - \sum_{k=1}^{2}\frac{Z_k}{\hat{r}_{ki}} + \sum_{j<i}\frac{1}{\hat{r}_{ij}}\right\} = \sum_{i=1}^{N}\left\{\hat{h}(i) + \sum_{j<i}\hat{g}(i,j)\right\}, \tag{2.8}$$

[1]The physical argument for the Born-Oppenheimer (BO) approximation is that the nuclear motion is very slow compared to the electronic. In the BO approximation the electronic motion is decoupled from the motion of the nuclei.

[2]The name of the program is somewhat uncertain. P. Sannes, who wrote the program, refers to it as MULMOD or MULTIMOD/MultiMOD in his thesis [21]. I will refer to it throughout as MultiMOD.

with

$$\hat{h}(i) \equiv -\frac{\hbar^2}{2m}\nabla_i^2 - \sum_{k=1}^{2}\frac{Z_k}{\hat{r}_{ki}}, \qquad \hat{g}(i,j) \equiv \frac{1}{\hat{r}_{ij}}. \tag{2.9}$$

We write $\hat{h}(i)$ to emphasize that this operator acts on the coordinates of electron i. The first term in equation (2.8) represents the kinetic energy of each electron, N in total. The second term is the electrostatic interaction between electron i and the nuclei. The third and last term is again an electrostatic interaction, between the N electrons. To avoid including any interaction twice, we keep summing over j as long as $j < i$.

The time-independent Schrödinger equation to be solved for this system reads

$$\hat{H}\Phi = E\Phi. \tag{2.10}$$

We can not solve this system exact. Instead an antisymmetric trial-wavefunction Φ obtained from a Slater determinant is used

$$\Phi = \frac{1}{\sqrt{N!}}\begin{vmatrix} \psi_a(1) & \psi_a(2) & \psi_a(3) & \dots & \psi_a(N) \\ \psi_b(1) & \psi_b(2) & \psi_b(3) & \dots & \psi_b(N) \\ \dots & \dots & \dots & \dots & \dots \\ \dots & \dots & \dots & \dots & \dots \\ \psi_x(1) & \psi_x(2) & \psi_x(3) & \dots & \psi_x(N) \end{vmatrix}. \tag{2.11}$$

Here $a, b, c, \dots, x$ are the possible set of quantum numbers for the individual electrons while $1, 2, \dots, N$ are electron labels. $\psi_k(i)$ are molecular orbitals given by

$$\psi_k(i) = \sum_{\alpha=1}^{M} c_{k\alpha}\phi_\alpha. \tag{2.12}$$

In equation (2.12) the molecular orbitals have been expanded as linear combinations of atomic orbitals ϕ (so called LCAO). The number M is the number of atomic orbitals included in the sum. We must of course have $M \geq N$. In theory the expansion (2.12) would be exact if M was large enough so that the atomic orbitals formed a complete set. Numerically we must however choose a finite set. Thus it is important that this set provides a reasonably accurate expansion for the molecular orbitals.

The atomic orbitals are often taken as Slater orbitals, also the case in our Hartree-Fock program. These Slater orbitals are given by

$$\phi_{nlm_lm_s} = r^{n-1}e^{-kr}Y_{lm_l}(\theta,\varphi)\begin{cases}\alpha & \text{Spin}\uparrow \\ \beta & \text{Spin}\downarrow\end{cases}. \tag{2.13}$$

The parameter k (in the exponential) are dependent upon the n, l and m_l quantum numbers, $k = k(n, l, m_l)$. When building a basis to use in calculations, the user must provide n, l, m_l and the k parameter for each atomic orbital.

In the Hartree-Fock method one seeks the Slater determinant that minimizes the expectation energy

$$E = \langle\Phi|\hat{H}|\Phi\rangle, \tag{2.14}$$

and at the same time require the molecular orbitals to be orthonormal

$$\langle\psi_k(i)|\psi_l(i)\rangle = \delta_{kl}. \tag{2.15}$$

By inserting equation (2.8) into equation (2.14) one obtains for the energy E

$$E = \sum_{k=1}^{N}\langle\psi_k(i)|\hat{h}(i)|\psi_k(i)\rangle + \sum_{k>l}^{N}\sum_{l=1}^{N}\left[\left\langle\psi_k(i)\psi_l(j)\left|\frac{1}{\hat{r}_{ij}}\right|\psi_k(i)\psi_l(j)\right\rangle - \left\langle\psi_k(i)\psi_l(j)\left|\frac{1}{\hat{r}_{ij}}\right|\psi_l(i)\psi_k(j)\right\rangle\right]. \tag{2.16}$$

The second term in equation (2.16) is often referred to as a *Coulomb* term. This is interpreted as the electrostatic repulsion between electron i and the other electrons (electron j summed over all orbitals). Thus the two-electron operator $\hat{g}(i,j)$ is replaced with an averaged one-electron potential.

The third term in equation (2.16) has no clear interpretation, it has to do with the correlations between electrons in molecular orbits k and l. It is often referred to as the *exchange* term since it involves an exchange of electron i and j. Often the coulomb operator $\hat{J}_l$ and the exchange operator $\hat{K}_l$ are defined as

$$\hat{J}_l(i)\psi_k(i) = \left[\int \mathrm{d}q_j\psi_l^*(j)\frac{1}{\hat{r}_{ij}}\psi_l(j)\right]\psi_k(i), \quad \hat{K}_l(i)\psi_k(i) = \left[\int \mathrm{d}q_j\psi_l^*(j)\frac{1}{\hat{r}_{ij}}\psi_k(j)\right]\psi_l(i). \tag{2.17}$$

The integrals should be taken over the spatial coordinates $\mathbf{r}_j$ and summed over the spin coordinates, indicated by $\mathrm{d}q_j$. We may now define the Fock operator $\hat{f}$

$$\hat{f} \equiv \hat{h}(i) + \sum_{l=1}^{N}\left[\hat{J}_l(i) - \hat{K}_l(i)\right] \equiv \hat{h}(i) + \hat{v}(i), \tag{2.18}$$

where the sum is over all the molecular orbitals. $\hat{v}(i)$ is often referred to as the Hartree-Fock potential. The Fock operator makes it possible to write down the Hartree-Fock equation

$$\hat{f}|\psi_k\rangle = \varepsilon_k|\psi_k\rangle \tag{2.19}$$

with ε_k as the orbital energy. Equation (2.19) is central to the next section on perturbation theory.

If equation (2.12) is inserted into the energy equation (2.16) we find the energy as a function of the unknown coefficients $c_{k\alpha}$. The coefficients that minimizes the energy can be found from (see also [29] and [28])

$$\sum_{\beta=1}^{M}(H_{\alpha,\beta} - \varepsilon_k S_{\alpha,\beta})c_{k,\beta} = 0, \tag{2.20}$$

for $\alpha = 1, 2, \ldots, M$, with

$$H_{\alpha,\beta} = \langle\phi_\alpha(i)|\hat{h}(i)|\phi_\beta(i)\rangle + \sum_{l=1}^{N}\sum_{\gamma,\delta=1}^{M} c_{l,\gamma}^* c_{l,\delta}\Big[\langle\phi_\alpha(i)\phi_\gamma(j)|\hat{g}(i,j)|\phi_\beta(i)\phi_\delta(j) - \langle\phi_\alpha(i)\phi_\gamma(j)|\hat{g}(i,j)|\phi_\beta(j)\phi_\delta(i)\rangle\Big], \tag{2.21}$$

and

$$S_{\alpha,\beta} = \langle \phi_\alpha(i) | \phi_\beta(i) \rangle. \tag{2.22}$$

Equation (2.20) is not as easy to solve as it may seem at first glance. It is important to remember that the coefficients to be determined is embedded in $H_{\alpha,\beta}$ itself. Because of this, equation (2.20) does not represent an ordinary system of linear equations. The equations must instead be solved by iterations. The process begins with a set of guessed coefficients. With these, the orbital energies ε_k can be calculated by solving the equation

$$|H_{\alpha,\beta} - \varepsilon_k S_{\alpha,\beta}| = 0. \tag{2.23}$$

Knowing the orbital energies ε_k we can obtain new coefficients using equation (2.20). The new coefficients are then used to calculate $H_{\alpha,\beta}$ and to obtain yet another set of coefficients until self-consistency is achieved.

2.2.1 Symmetries and configurations, closed shells and open shells

The molecular orbitals are ordered into groups depending on their symmetry properties. Atoms have the well known spherical symmetry. For diatomic molecules the spherical symmetry is replaced by cylindrical symmetry because the internuclear axis of a diatomic molecule favors one direction in space. As a consequence, $\hat{\mathbf{L}}^2$ is no longer a quantized operator.

It is standard to let the internuclear axis of the molecule be the z-axis. If we neglect the spin-orbit coupling (A $\hat{\mathbf{L}} \cdot \hat{\mathbf{S}}$), M_L is still a good quantum number and $[\hat{H}, \hat{L}_z] = 0$. The same is true for M_S which is also well defined when spin-orbit coupling is neglected. M_L and M_S are described by the quantum numbers Λ and Σ, defined by

$$\Lambda = |M_L| = 0, 1, 2, \ldots, L, \qquad \Sigma = M_S = S, S-1, \ldots, -S. \tag{2.24}$$

Each of the possible values the quantum number Λ can take have a spectroscopic label. We list here the labels corresponding to $\Lambda = 0, 1, 2, 3$.

$$\Lambda = 0 \leftrightarrow \Sigma, \qquad \Lambda = 1 \leftrightarrow \Pi, \qquad \Lambda = 2 \leftrightarrow \Delta, \qquad \Lambda = 3 \leftrightarrow \Phi.$$

Sometimes we are interested in the quantum numbers of an individual electron. For this purpose lowercase notation $\lambda = |m_l|$ is used, with the corresponding spectroscopic notation

$$\lambda = 0 \leftrightarrow \sigma, \qquad \lambda = 1 \leftrightarrow \pi, \qquad \lambda = 2 \leftrightarrow \delta, \qquad \lambda = 3 \leftrightarrow \phi.$$

On occasions one may also see notation like π^- with the meaning $m_l = -1$ for a single electron.

There are also other symmetries that need to be considered. For homonuclear molecules we have an additional $g/\ u$ symmetry. g and u represents the two possible eigenvalues for the operator $\hat{I}_e$ that inverts the electron coordinates. Obviously

$$\hat{I}_e^2 \psi = \psi, \tag{2.25}$$

from which it follows that the only possible eigenvalues are ± 1. For some reason the $+1$ eigenvalue is labeled g for *gerade* and the -1 eigenvalue is labeled u for *ungerade*.

For diatomic molecules (not necessarily homonuclear), each plane containing the internuclear axis is a valid mirror plane. The operator for reflection of the electrons in one of these planes is σ

$$\sigma\psi = \pm\psi, \tag{2.26}$$

with $\pm$ as the possible eigenvalues. The eigenvalue of this operator is included in the notation by a $\pm$. It is common to include also the total spin $|\mathbf{S}| = \sum_i \mathbf{s}_i$ in the notation. Thus, to characterize an electronic state we write

$$^{2S+1}\Lambda^{\pm}_{g/u}. \tag{2.27}$$

Sometimes we may also want to express explicitly that an electronic state is the ground state. This is achieved by adding an X in front of (2.27). The electronic state lowest in energy accessible through an optical transition from the ground state is labeled A, the next one B and so on. For the ground state in Li_2, we may write

$$Li_2(\text{ ground state}) : X^1\Sigma^+_g, \tag{2.28}$$

with the electronic configuration,

$$Li_2(\text{ground state electron configuration}): (1\sigma_g)^2(1\sigma_u)^2(2\sigma_g)^2. \tag{2.29}$$

The basis in the Hartree-Fock program is specified in terms of n, l and m_l quantum numbers for the atomic orbitals. The possible symmetries of the molecular orbitals follows from those of the atomic orbitals.

The Hartree-Fock literature makes a distinction between closed shell Hartree-Fock, also called restricted Hartree-Fock theory, and open shell Hartree-Fock. A shell is closed if all spin-orbitals are occupied by an electron. For example, the Li_2 ground state has only closed shells. A shell that is partially occupied is open, consider for example Li_2^+ with configuration

$$Li_2^+: (1\sigma_g)^2(1\sigma_u)^2(2\sigma_g). \tag{2.30}$$

Here the $2\sigma_g$ shell is only partially filled, and thereby open. The unrestricted Hartree Fock method to treat also these systems is more complex than the closed shell theory presented in this section. The complications arise from the fact that there may be more than one Slater determinant that needs to be varied to minimize the energy. See [21] for a further discussion of the open shell problem. We will however use the fact that also with open shells it is possible to construct a Fock operator $\hat{f}$

$$\hat{f}(i) \equiv \hat{h}(i) + \hat{u}(i), \tag{2.31}$$

with $\hat{u}$ as a one-electron operator analog to $\hat{v}$. The explicit form of $\hat{u}$ will not be considered. We only remark that the Hartree-Fock program used has options for open shells based on a Fock operator as given in equation (2.31).

2.2.2 Input and output

The Hartree-Fock program was originally developed at the Chemical Institute in Bergen as early as 1975 [29]. It can be used for both atoms and diatomic molecules. To run, it requires a formatted input file containing the following information:

- Specification of the atomic orbitals to be included, also referred to as the basis . The input file is arranged as a list with the k parameters to be used in the Slater orbitals along with quantum numbers n, l and m_l for each atomic orbital.
- Number of symmetries in the basis, number of electrons, the nuclear charge and also the internuclear distance when the program is used for molecules.
- Information on which orbitals to be filled, open and empty.
- If there exists open orbitals, a set of coefficients is needed to describe the coupling between the different states within the same configuration.
- Initialization of the coefficients in equation (2.12).

With this input, output are the following

- The total energy:
- Coefficients and the orbital energy for each molecular orbital.
- A variety of one electron integrals $\langle\psi_1|\mathcal{O}|\psi_2\rangle$, with a menu of possible one-electron operators $\mathcal{O}$.
- The two electron integrals $\left\langle \psi_1\psi_2\left|\frac{1}{\hat{r}_{12}}\right|\psi_3\psi_4\right\rangle$ are printed to file.

An example of an input file used in the calculations for Li_2 is provided in appendix A.

2.2.3 Obtaining a good basis for Li_2

During my work to obtain the interatomic potential curves for Li_2, much time went into optimizing the basis. Here I give a short résumé of this process and also try to extract some general conclusions from the whole process.

The basis orbitals were first optimized with k-parameters found to be well suited for Hartree-Fock calculations on the Li atom. These were taken mainly from [30] but we also ran the Hartree-Fock program for the Li atom to optimize orbitals not included in [30]. With this kind of atomic optimization we were able to determine the orbitals with the larger values on the k parameters. The more diffuse orbitals that must be included to described a molecule, needs to be optimized with an element of try and fail. With diffuse orbitals I mean Slater orbitals with a small k value. These will extend further out from the nucleus (remember that the Slater orbitals are proportional to e^{-kR}). To make optimization of these diffuse orbitals easier, we used the so called even tempered basis rule

$$k_i = k_0\xi^{i-1}, \tag{2.32}$$

for optimizing coefficients belonging to the same symmetry. ξ was originally equal to 1.5, but I often found better results using a somewhat larger ξ. The advantage of equation (2.32) is the large reduction in the number of variables to vary (only k_0 for each symmetry).

One of the most important considerations to make when constructing the basis is the number of atomic orbitals to include. To include too many causes numerical problems, since it gets increasingly hard to make the orbitals orthogonal to each other. If on the other hand

the number of basis orbitals are too few, the results obtained may never correspond to the known dissociation limits and be seriously in error. To include the correct number of orbitals probably requires some experience. I needed to try several different basis sets (of different size), before I found a good basis. To sum up, the following steps may be useful to complete when making a basis

1. Optimize the large k parameters from atomic data.
2. Include diffuse orbitals, and optimize with the even tempered rule.
3. Compare results with known dissociation limits. If the results are seriously in error, try to change the number of basis orbitals. Make sure that the molecular orbitals remains orthogonal at all times. Finally, to improve results further, some fine-tuning of the k-parameters may be needed.

2.3 Multidimensional model space

Obtaining the interatomic potential for any diatomic molecule is in general not an easy task. In this section multi-reference many-body theory is used for this purpose. This section is named after the MultiMOD (multidimensjonalt modellrom) program, used to find the interatomic potential curves after having completed a Hartree-Fock calculation. MultiMOD was originally written by Pål Sannes for the cand.scient degree [21]. He wrote a large program based on the perturbation theory developed by Hose and Kaldor [24]-[26]. The program and the programming details are of course also more thoroughly described in his thesis [21].

2.3.1 Degenerate Perturbation theory

Consider a time-independent Hamiltonian that can be split in two parts

$$\hat{H} = \hat{H}_0 + \hat{V}. \tag{2.33}$$

We seek eigenvectors and eigenvalues to the Schrödinger equation

$$\hat{H}|\Psi\rangle = E|\Psi\rangle. \tag{2.34}$$

We assume to know both the eigenvalues and eigenvectors of $\hat{H}_0$

$$\hat{H}_0|\Phi_k\rangle = E_k|\Phi_k\rangle. \tag{2.35}$$

A Hartree-Fock calculation has been performed and we can therefore use

$$\hat{H}_0 = \sum_{i=1}^{N}[\hat{h}(i) + \hat{u}(i)], \tag{2.36}$$

$$\hat{V} = \sum_{i<j}\frac{1}{\hat{r}_{ij}} - \sum_{i=1}^{N}\hat{u}(i). \tag{2.37}$$

Φ_k is different Slater determinants built from the set of orbitals $\{\psi_i\}$ provided by the Hartree-Fock calculations. All symbols and operators used in equation (2.36) and equation (2.37) are

defined in the previous section. $\hat{V}$ is regarded as a perturbation and should be small. We will not assume that the energies are non-degenerate, so it may happen that g eigenvectors correspond to the same eigenvalue in equation (2.35).

We continue to define the *model space* M. M is spanned by one or more of the eigenvectors for $\hat{H}_0$. The model space must be chosen in such a way that approximations to the eigenfunctions for $\hat{H}$ that we are interested in, are within M.

To continue, a projection operator is defined

$$\hat{P} = \sum_{|\Phi_k\rangle \in M} |\Phi_k\rangle\langle\Phi_k|, \tag{2.38}$$

where the meaning of the subscript $|\Phi_k\rangle \in M$ is; sum over the $|\Phi_k\rangle$ that are in the M-space. Another projection operator (the orthogonal projection) is also defined

$$\hat{Q} = \sum_{|\Phi_k\rangle \notin M} |\Phi_k\rangle\langle\Phi_k|, \tag{2.39}$$

where the sum is taken over the $|\Phi_k\rangle$ that are not in the M-space. This operator projects into a space orthogonal to the M-space. There exists several properties for the operators $\hat{P}$ and $\hat{Q}$, $\hat{P} + \hat{Q} = 1$ is obvious from the completeness relation. We also have

$$\hat{P}^2 = \sum_{|\Phi_k\rangle \in M} \sum_{|\Phi_{k'}\rangle \in M} |\Phi_k\rangle\langle\Phi_k|\Phi_{k'}\rangle\langle\Phi_{k'}| = \sum_{|\Phi_k\rangle \in M} |\Phi_k\rangle\langle\Phi_k| = \hat{P}, \tag{2.40}$$

$$\hat{Q}^2 = \hat{Q}, \tag{2.41}$$

$$\hat{P}\hat{Q} = \sum_{|\Phi_k\rangle \in M} \sum_{|\Phi_{k'}\rangle \notin M} |\Phi_k\rangle\langle\Phi_k|\Phi_{k'}\rangle\langle\Phi_{k'}| = 0. \tag{2.42}$$

Let me now rewrite the Schrödinger equation in two different ways. Multiply equation (2.34) with $\hat{P}$ from left and multiply equation (2.34) with $\hat{Q}$, also from the left, keeping in mind the properties of the projection operators. The goal is to obtain an effective Hamiltonian acting only *inside* the M-space and having $\dim(M)$ eigenvalues equal to those of the complete Hamiltonian $\hat{H}$.

$$\hat{H}|\Psi\rangle = E|\Psi\rangle, \tag{2.43}$$

$$\hat{P}\hat{H}|\Psi\rangle = E\hat{P}|\Psi\rangle, \tag{2.44}$$

$$\hat{Q}\hat{H}|\Psi\rangle = E\hat{Q}|\Psi\rangle. \tag{2.45}$$

We insert the completeness relation $\hat{P} + \hat{Q} = 1$, and use the properties $\hat{P}^2 = \hat{P}$ and $\hat{Q}^2 = \hat{Q}$

$$\hat{P}\hat{H}(\hat{P}^2 + \hat{Q}^2)|\Psi\rangle = E\hat{P}|\Psi\rangle, \tag{2.46}$$

$$\hat{Q}\hat{H}(\hat{P}^2 + \hat{Q}^2)|\Psi\rangle = E\hat{Q}|\Psi\rangle. \tag{2.47}$$

If we define $|\Psi^0\rangle = \hat{P}|\Psi\rangle$, equations (2.46) and (2.47) takes the form

$$\hat{P}\hat{H}\hat{Q}^2|\Psi\rangle + \hat{P}\hat{H}\hat{P}|\Psi^0\rangle = E|\Psi^0\rangle, \tag{2.48}$$

$$\hat{Q}\hat{H}\hat{P}|\Psi^0\rangle + \hat{Q}\hat{H}\hat{Q}^2|\Psi\rangle = E\hat{Q}|\Psi\rangle. \tag{2.49}$$

Using equation (2.49) to eliminate $\hat{Q}|\Psi\rangle$ in equation (2.48) yields

$$\left\{\hat{P}\hat{H}\hat{P} + \hat{P}\hat{H}\hat{Q}[E - \hat{Q}\hat{H}\hat{Q}]^{-1}\hat{Q}\hat{H}\hat{P}\right\}|\Psi^0\rangle = E|\Psi^0\rangle. \tag{2.50}$$

The expression in the brackets is referred to as an effective Hamiltonian, defined by

$$\hat{H}_{\text{eff}} \equiv \hat{P}\hat{H}\hat{P} + \hat{P}\hat{H}\hat{Q}[E - \hat{Q}\hat{H}\hat{Q}]^{-1}\hat{Q}\hat{H}\hat{P}. \tag{2.51}$$

Equations (2.50) and (2.51) combined reads

$$\hat{H}_{\text{eff}}|\Psi^0\rangle = E|\Psi^0\rangle. \tag{2.52}$$

The eigenvectors of the effective Hamiltonian represents the model functions within the M (model) space. This means that we have made a transition from equation (2.43) defined over the whole Hilbert space, to equation (2.52) defined over a finite model space M. It is useful to ease the further development of perturbation theory by introducing a reference energy E_0 (equal to the degenerate energy). To avoid complications in the case of a partially degenerate model space[3], a shifted zero-order Hamiltonian $\hat{H}_{\text{s0}}$ is introduced to make M a (completely) degenerate subspace of $\hat{H}_{\text{s0}}$.

$$\hat{H}_{\text{s0}} = \hat{H}_0 + \sum_{|\Phi_k\rangle \in M} (E_0 - \hat{H}_0)|\Phi_k\rangle\langle\Phi_k|. \tag{2.53}$$

To see why this work, consider

$$\hat{H}_{\text{s0}}|\Phi_k\rangle = \hat{H}_0|\Phi_k\rangle + \sum_{|\Phi_{k'}\rangle \in M} (E - \hat{H}_0)|\Phi_{k'}\rangle\langle\Phi_{k'}|\Phi_k\rangle \tag{2.54}$$

$$= \hat{H}_0|\Phi_k\rangle + E_0|\Phi_k\rangle - \hat{H}_0|\Phi_k\rangle = E_0|\Phi_k\rangle, \tag{2.55}$$

with $|\Phi_k\rangle \in M$.

We also need to introduce $\hat{V}_{\text{s}}$ to meet the requirement $\hat{H} = \hat{H}_{\text{s0}} + \hat{V}_{\text{s}}$. In order to define the so called effective interaction $\hat{W}$, calculate

$$\langle\Phi_{k'}|\hat{H}_{\text{eff}} - \hat{H}_{\text{s0}}|\Phi_k\rangle = \langle\Phi_{k'}|\hat{P}\hat{H}\hat{P} + \hat{P}\hat{H}\hat{Q}[E - \hat{Q}\hat{H}\hat{Q}]^{-1}\hat{Q}\hat{H}\hat{P} - \hat{H}_{\text{s0}}|\Phi_k\rangle, \tag{2.56}$$

$$= \langle\Phi_{k'}|\hat{P}\hat{V}_{\text{s}}\hat{P} + \hat{P}(\hat{H}_0 + \hat{V})\hat{Q}[E - \hat{Q}\hat{H}\hat{Q}]^{-1}\hat{Q}(\hat{H}_0 + \hat{V})\hat{P}|\Phi_k\rangle \tag{2.57}$$

($|\Phi_k\rangle$ and $|\Phi_{k'}\rangle$ are in M). This expression simplifies considerably if we realize that

$$\langle\Phi_{k'}|\hat{P}\hat{H}_0\hat{Q} = 0, \qquad \hat{Q}\hat{H}_0\hat{P}|\Phi_k\rangle = 0. \tag{2.58}$$

Equation (2.58) is true since neither $\hat{P}$ nor $\hat{H}_0$ projects any part of $|\Phi_k\rangle$ or $|\Phi_{k'}\rangle$ outside of M. The projection operator $\hat{Q}$ will therefore give zero. Thus

$$\langle\Phi_{k'}|\hat{H}_{\text{eff}} - \hat{H}_{\text{s0}}|\Phi_k\rangle = \langle\Phi_{k'}|\hat{P}\hat{V}_{\text{s}}\hat{P} + \hat{P}\hat{V}\hat{Q}[E - \hat{Q}\hat{H}\hat{Q}]^{-1}\hat{Q}\hat{V}\hat{P}|\Phi_k\rangle$$

$$= \langle\Phi_{k'}|\hat{W}(\Delta E)|\Phi_k\rangle, \tag{2.59}$$

[3] A partially degenerate model space is a model space where at least two of the zero order energies are different. If all zero order energies are the same, the space is degenerate

with

$$\hat{W}(\Delta E) \equiv \hat{P}\hat{V}_{\rm s}\hat{P} + \hat{P}\hat{V}\hat{Q}[\Delta E + E_0 - \hat{Q}\hat{H}\hat{Q}]^{-1}\hat{Q}\hat{V}\hat{P}, \tag{2.60}$$

$\Delta E \equiv E - E_0$. Note that

$$(\hat{H}_{\rm eff} - \hat{H}_{\rm s0})|\Psi^0\rangle = (E - E_0)|\Psi^0\rangle. \tag{2.61}$$

In equation (2.61) we have used

$$\hat{H}_{s0}|\Psi_k^0\rangle = \hat{H}_{\rm so}\sum_{i=1}^{M} c_{ki}\Phi_i = E_0|\Psi_k^0\rangle, \tag{2.62}$$

which follows from equation (2.55)[4]. Equations (2.59) and (2.61) then yields the eigenvalue equation

$$\hat{W}(\Delta E)|\Psi^0\rangle = \Delta E|\Psi^0\rangle. \tag{2.63}$$

The key idea to perturbation theory is that it may be possible to get reasonable approximations for some solutions by expanding $\hat{W}$ as a power series in the perturbation $\hat{V}$. We can however notice two complications with the expression (2.60) for $\hat{W}(\Delta E)$:

1. $\hat{W}$ is dependent upon its own eigenvalue.

2. $\hat{W}$ has unkown poles.

By recursion, a power series in the perturbation $\hat{V}$ for the inverse operator in equation (2.60) can be obtained [24]. This enables us to write the $\hat{W}$ operator as an infinite series

$$\hat{W}(\Delta E) = \sum_{n=1}^{\infty}\hat{W}_n, \tag{2.64}$$

with $\hat{W}_n$ as the n'th order term in $\hat{V}$. For $\hat{W}_1$, $\hat{W}_2$ and $\hat{W}_3$ we have

$$\hat{W}_1 = \hat{P}\hat{V}_{\rm s}\hat{P}, \tag{2.65}$$

$$\hat{W}_2 = \sum_{|\Phi_k\rangle\in M}, \hat{P}\hat{V}\hat{G}_k\hat{V}\hat{P}_k \tag{2.66}$$

$$\hat{W}_3 = \sum_{|\Phi_k\rangle\in M}\hat{P}\left[\hat{V}\hat{G}_k\hat{V}\hat{G}_k\hat{V} - \sum_{|\Phi_{k'}\rangle\in M}\hat{V}\hat{G}_k\hat{G}_{k'}\hat{V}\hat{P}_{k'}\hat{V}\right]\hat{P}_k, \tag{2.67}$$

with $\hat{P}_k = |\Phi_k\rangle\langle\Phi_k|$ and $\hat{G}_k = [E_k - \hat{H}_0]^{-1}\hat{Q}$.

[4]We also use the fact that since $|\Psi_k^0\rangle$ is in the M-space, it can be written as a linear combinations of the Φ_i that spans M.

2.3.2 Hose-Kaldors method

MultiMOD is based on the multi-reference many-body perturbation theory developed by Hose and Kaldor. Why exactly this method was chosen is discussed in [21]. The discussion will not be repeated here, we only mention some advantages with Hose-Kaldors method:

- Hose-Kaldors method does *not* require complete model spaces.
- Problems with so called intruder states are reduced. This is intimately linked with the first point.
- The method converges fast and requires reasonable running time.

To understand this, some definitions are needed. *Nuclear orbitals* are spin orbitals occupied in all Slater determinants. *Virtual orbitals* are spin orbitals not occupied in any Slater determinants. *Valence orbitals* are all other orbitals (sometimes occupied, sometimes not). A *complete model space* is defined as a space spanned by all Slater determinants that can be formed by distributing the valence electrons on the valence orbitals.

Ideally one would want an energy gap between the eigenvalues of the effective Hamiltonian $\hat{H}_{\text{eff}}$ and the eigenvalues of the Hamiltonian $\hat{H}$. In other words the energy range spanned by determinants in the M-space should be well separated from the energy range of the determinants in the Q-space. Often however, it is impossible to choose the Q-space in such a way. As a consequence, there will be determinants within the Q-space that lie close to or perhaps within the range of the M-space eigenvalues. See also the illustration in figure 2.1

Figure 2.1. *Horizontal lines represents eigenvalues of the M-space and the Q-space. In the situation illustrated to the left the eigenvalues of the model space and the Q-space are well separated. To the right we illustrate a situation where eigenvalues of the Q space intrudes the energy range of the model states. These are intruder states.*

Intruder states might cause the expansion of $\hat{W}$ to diverge, or to converge to a intruder state, instead of a real eigenstate of $\hat{H}_{\text{eff}}$.

To find the energy, ΔE in equation (2.63) we need to evaluate the matrix element

$$\langle \Phi_k | \hat{W} | \Phi_l \rangle, \tag{2.68}$$

with $|\Phi_k\rangle$ and $|\Phi_l\rangle$ being Slater determinants consisting of single-particle states. MultiMOD is concerned with the elements of $\hat{W}$ through second order in the perturbation. These matrix

Figure 2.2. *One-electron interactions as in equation (2.70) are represented with the diagram to the left. Two-electron interactions as in equation (2.71) are represented with the diagram to right. The diagram to the right corresponds to the first term in (2.71).*

elements are

$$\langle\Phi_k|\hat{W}_1|\Phi_l\rangle = \langle\Phi_k|V_s|\Phi_l\rangle, \qquad \langle\Phi_k|\hat{W}_2|\Phi_l\rangle = \sum_{\beta\in Q}\frac{\langle\Phi_k|\hat{V}|\beta\rangle\langle\beta|\hat{V}|\Phi_l\rangle}{E_l - E_\beta}, \tag{2.69}$$

with E_l and E_β as zero order energies. It is interesting to see that in the second order element of $\hat{W}$, effects from the Q-space are included. We also see from equation (2.69) that if there exists states in the Q-space within the energy range of the M-space, the denominator may be small and cause divergence.

The matrix elements in (2.69) can be calculated from Slaters rules [31]. These rules allows us to write the matrix elements in (2.69) as a sum over matrix elements of the one-electron operator $\hat{u}(i)$ and the two electron operator $\frac{1}{\hat{r}_{ij}}$ between different single-particle states composing the determinants Φ_k and Φ_l. For example, if Φ_k and Φ_l differ by one single particle state ψ_a being replaced by ψ_r in Φ_k, Slaters rules dictates for the one-electron part of $\hat{V}$

$$\left\langle \Phi_k \middle| \sum_{i=1}^{N} \hat{u}(i) \middle| \Phi_l \right\rangle = \left\langle \psi_r \middle| \hat{u}(i) \middle| \psi_a \right\rangle. \tag{2.70}$$

Similar rule exists for two-electron operators and also for Φ_k and Φ_l differing by more than one single particle state. If Φ_k differ from Φ_l by the single particle states ψ_a, ψ_b being replaced by ψ_r and ψ_s, Slaters rules dictates

$$\left\langle \Phi_k \middle| \sum_{i<j} \frac{1}{\hat{r}_{ij}} \middle| \Phi_l \right\rangle = \left\langle \psi_r\psi_s \middle| \frac{1}{\hat{r}_{ij}} \middle| \psi_a\psi_b \right\rangle - \left\langle \psi_s\psi_r \middle| \frac{1}{\hat{r}_{ij}} \middle| \psi_a\psi_b \right\rangle. \tag{2.71}$$

In principle it is possible to rely simply on Slaters rules, however for higher order terms it is often favorable to use diagrams to express the different elements of $\hat{W}_n$. To second order there are 21 such diagrams to be evaluated. Diagrammatic representations of one-electron interactions as in equation (2.70) and two-electron interactions as in equation (2.71) are illustrated in figure 2.2. For a more thorough discussion of the diagrams I refer to [21] and references therein.

2.3.3 Input/Output

To run, MultiMOD needs a formatted input file from the user. An example of such a file is given in appendix A. Certain information must be provided in the input file

- Number of symmetries, number of orbitals, and the "potnuc number" $\frac{Z_A Z_B}{R}$. Notice that the "potnuc number" must be changed for each internuclear distance R.

- The different electronic configurations to be included. These are specified with numbers 0 and 1 under the FI heading. 1 indicates occupied while 0 indicates unoccupied.

- Ordering of the orbitals ψ_a, ψ_b, ψ_c.... must be specified in the vector NRO.

As seen in appendix A, some additional information is also listed but this is mostly constants that are left unchanged when working on Li_2.

We have used M-spaces with up to 20-30 different configurations when running MultiMOD, since it is important to have a large model space. This is important in order to include the interactions between as many states as possible.

The program will however on its own further expand the model space to include all Slater determinants with the same M_L and M_S as the ones specified by the user. By this mechanism the correct symmetry for the eigenvectors of $\hat{H}_{\text{eff}}$ is ensured. This must be done since a Slater determinant automatically will be an eigenstate for the $\hat{S}_z$ and $\hat{L}_z$ operator, but not necessarily for $\hat{\mathbf{S}}^2$ and $\hat{I}_e$. With the expansion of the model space, $\hat{H}_{\text{eff}}$ will have the same symmetry properties as the original Hamilton operator $\hat{H}$.

It is all the time assumed that a Hartree-Fock calculation has been performed before MultiMOD is used. One-electron integrals and two electron integrals together with the spin orbitals are read from a file created when the Hartre-Fock calculations has converged.

As output MultiMOD gives first- and second order eigenvalues and eigenvectors. Also included are the transition probabilities. To be more specific, what is actually calculated are the matrix elements $\langle\Psi_2|\hat{d}_z|\Psi_1\rangle, \langle\Psi_2|\hat{d}_x|\Psi_1\rangle$ and $\langle\Psi_2|\hat{d}_y|\Psi_1\rangle$ with Ψ_1 and Ψ_2 as eigenstates of the effective Hamiltonian. $\hat{d}_x, \hat{d}_y, \hat{d}_z$ are the transition dipole elements in the respective directions. See also next chapter for a further discussion of the transition dipole moments.

By first running the Hartree-Fock program and second the MultiMOD program for different electronic states and for different R-values, we were able to obtain the potential curves, $E_e(R)$, for the ten lowest laying states in Li_2.

2.4 Calculating vibrational-levels with Numerov's method

Equation (2.72) describes the movement of the nuclei in the potential $E_e(R)$ (see also (2.7)). In this section we investigate the solutions to this equation.

$$\left\{-\frac{\hbar^2}{2\mu}\nabla^2 + E_e(R)\right\}\psi_n(R,\theta,\phi) = E_v\psi_n(R,\theta,\phi). \tag{2.72}$$

Equation (2.72) formally corresponds to the Schrödinger equation for the hydrogen atom. Thus, we know that equation (2.72) is exact separable (in spherical coordinates), and we write

$$\psi_n(R,\theta,\phi) = \frac{1}{R}\psi_v(R)\psi_J(\theta,\phi) \tag{2.73}$$

with $\psi_J(\theta,\phi)$ as eigenfunctions of the operators $\hat{\mathbf{J}}^2$ and $\hat{\hat{J}}_z$ where $\mathbf{J}$ is the quantum number of the total angular momentum. $\psi_v(R)$ must therefore satisfy[5]

$$\left\{-\frac{\hbar^2}{2\mu}\frac{d^2}{dR^2}+E_e(R)-\frac{\hbar^2 J(J+1)}{2\mu R^2}\right\}\psi_v(R)=E_v\psi_v(R), \tag{2.74}$$

and this is the equation we have to solve.

The solution to equation (2.74) are found using a third program, *Vibra*. Vibra is based on Numerovs algorithm and was originally developed by Leif Veseth. The program is used without, or with minor modifications.

2.4.1 Numerovs method

Numerovs method is designed to solve second order differential equations without any first order derivatives. This is differential equations of the form

$$\frac{d^2y}{dx^2}=F(x,y). \tag{2.75}$$

The method is well designed for problems in physics, since both Newtons second law and the Schrödinger equation are of the desired form (2.75). Let us now concentrate on the Schrödinger equation (2.74) (with $J=0$)

$$\frac{d^2}{dR^2}\psi_v(R)=\frac{2\mu}{\hbar^2}\left[E_e(R)-E_v\right]\psi(R)=f(R)\psi(R). \tag{2.76}$$

μ is the reduced mass and $f(R)\equiv\frac{2\mu}{\hbar^2}\left[E_e(R)-E_v\right]$. We now expand $\psi(R+h)$ and $\psi(R-h)$ in Taylor series

$$\psi(R+h)\simeq\psi(R)+h\psi'(R)+\frac{h^2\psi^{(2)}(R)}{2}+\frac{h^3\psi^{(3)}(R)}{6}+\cdots, \tag{2.77}$$

$$\psi(R-h)\simeq\psi(R)-h\psi'(R)+\frac{h^2\psi^{(2)}(R)}{2}-\frac{h^3\psi^{(3)}(R)}{6}+\cdots. \tag{2.78}$$

h is the steplength, not to be confused with the Planck constant. Terms of order h^4 and higher are neglected. Adding equations (2.77) and (2.78), subtracting $2\psi(R)$ yields

$$\psi(R+h)+\psi(R-h)-2\psi(R)=h^2\psi^{(2)}(R). \tag{2.79}$$

Now we introduce a new notation[6]

$$\psi(R+h)=\psi_{n+1}\qquad\psi(R)=\psi_n\qquad\psi(R-h)=\psi_{n-1}\qquad. \tag{2.80}$$

The second derivative $\psi^{(2)}(R)$ can be expressed in terms of E_v from equation (2.76). Using this, equation (2.79) yields a recurrence relation

$$\psi_{n+1}+\psi_{n-1}-\left(2+h^2f_n\right)\psi_n=0. \tag{2.81}$$

[5] $\psi_v(R)$ is of course not equal to Laguerre functions, since $E_e(R)$ is not a Coulomb potential.

[6] This notation is often used in computational physics to emphasize the evaluation of functions in discrete points, and as a shorthand notation.

If we knew ψ_0 and ψ_1 we could in principle generate the whole wavefunction from the equation above. However, we want to impose the conditions $\psi_0 = \psi_N = 0$ where N is the total number of steps. These boundary conditions ensures that the bound state wavefunction can be normalized. We observe that equation (2.81) can be written as a tridiagonal matrix

$$\begin{pmatrix} a_1 & 1 & 0 & & \dots & 0 \\ 1 & a_2 & 1 & 0 & \dots & 0 \\ 0 & 1 & a_3 & 1 & \dots & 0 \\ & & \dots\dots\dots\dots & & & \\ & & \dots\dots\dots\dots & & & \\ 0 & . & 0 & 1 & a_{N-2} & 1 \\ 0 & & \dots & 0 & 1 & a_{N-1} \end{pmatrix} \begin{pmatrix} \psi_1 \\ \psi_2 \\ \psi_3 \\ \dots \\ \dots \\ \psi_{N-2} \\ \psi_{N-1} \end{pmatrix} = 0, \tag{2.82}$$

with $a_n \equiv 2 + h^2 f_n = 2 + \frac{2\mu h^2}{\hbar^2}[E_e(R)]_n - \frac{2h^2\mu}{\hbar^2}E$. The tridiagonal matrix will give $N-1$ eigenvalues. When an eigenvalue is found we can find the corresponding eigenvector by solving equation (2.82) as a system of linear equations.

2.4.2 Calculating matrix elements

Vibra can also calculate matrix elements of the form

$$\langle \psi_{v'} | \hat{Y} | \psi_v \rangle = \int_{R_{\min}}^{R_{\max}} \psi^*_{v'}(R) \hat{Y}(R) \psi_v(R) \mathrm{d}R \tag{2.83}$$

with $\hat{Y}$ as an operator. The integral is performed with Simpsons method. In the next chapter we use this possibility to calculate numerous matrix elements.

2.4.3 Input/Output

As input, the program Vibra requires a file with the following information:

- A number of data points (decided by the user) on two potential curves (can also be the same potential curve read in twice). The potential curves are read in from two columns, one for the internuclear distance R and one for the corresponding potential energy in electron volts.
- Equilibrium distance for the two electronic states that are read in.
- $\langle n_l \Omega_l | Y | n_k \Omega_k \rangle = Y(R)$ for different R values are listed. The program can interpolate the function $Y(R)$ and integrate over a specified interval.
- Specification of the step length h to be used in Simpsons method.
- Number of vibrational levels to be calculated for the two potentials.

Output is given by:

- Eigenvalues for the different vibrational levels for both potential curves.
- Matrix elements $\langle \psi_{v'} | Y(R) | \psi_v \rangle$ for the operator $Y(R)$ for all possible combinations of v' and v.

An example of an input file is given in appendix A.

Chapter 3

Ultracold molecules with photoassociation

In chapter one we presented a variety of methods available for cold molecule production. In this chapter we investigate one method more thoroughly, namely photoassociation. Photoassociation is a very powerful tool for cold molecule formation, and it can be used to produce molecules with ultracold temperatures. We focus on Lithium and especially the $^6Li_2$ molecule. This molecule was chosen because $^6Li_2$ has been subject to a lot of interest in recent years, both for photoassociation experiments and because of a Feshbach resonance. Heteronuclear molecules involving Li such as LiNa and $^6Li^7Li$ are also currently being studied by different groups worldwide. Our plans were in addition to work with the LiNa molecule, but time did not allow for this. We will throughout this chapter assume to have access to pre-cooled atoms. These are cooled by one of the methods discussed in chapter 1.

With the aid of our three programs presented in the previous chapter we are able to predict numerous properties of the molecules produced by photoassociation and subsequent spontaneous decay. In this chapter we report calculations of the ten lowest laying electronic states in $^6Li_2$, as well as the vibrational levels in all bound electronic states. We are also in a position to calculate both Franck-Condon factors, and transition dipole moments between different vibrational levels, belonging to different electronic states.

Finally, formation rates will be worked out, along with the probability for populating the various vibrational levels. We will also approximate what fraction of the total decay that actually produces molecules, and what fraction that represents molecules lost. Usually the fraction that is lost is by far dominant, the question is how dominant. We begin this chapter by introducing photoassociation as a method to produce cold molecules and present relevant theory for the calculations to come.

3.1 Photoassociation of laser-cooled atoms

The idea of using cold and trapped atoms to make cold molecules through photoassociation came originally from Torsheim, Weiner and Julienne [33] in 1987. They studied sodium atoms that collided with each other in the presence of a laser. The laser frequency ω_1 was tuned to match the energy difference between the molecular ground state and a vibrational level of an excited state. This process is known as photoassociation because it associates two

atoms to a bound molecular state with the aid of one photon.

To understand how cold molecules can be produced, assume that we have access to ultracold atoms ($T \approx 1\mu$K). These atoms will make up the molecules that we seek to produce. Very often the MOT technique is used to cool the atoms used in photoassociation experiments. The atoms are in their ground state an are allowed to approach each other. At large internuclear separations (how large depends on the atomic species) the atoms are excited to a vibrational level of an excited electronic state. The cold molecule production occurs as the excited state molecules decay into vibrational levels of the molecular ground state. Figure 3.1 shows this process schematically. The laser frequency ω_1 used to excite the long-range

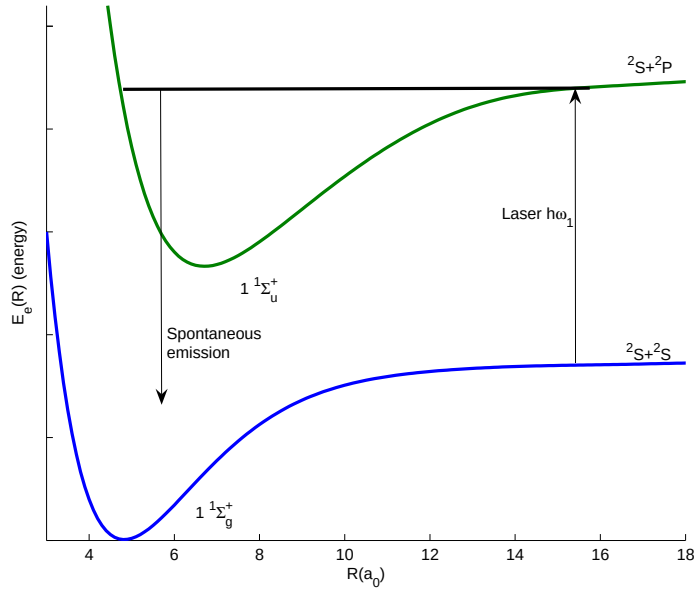

Figure 3.1. *Two ground state atoms approaching each other along the asymptotic* $^2S + ^2S$ *ground state molecular potential curve* $E_e(R)$*. With a laser the two atoms are excited to a bound vibrational level of an excited electronic state. From this vibrational level spontaneous emission brings the molecule down to a ground state vibrational level.*

molecule must satisfy

$$\hbar\omega_1 + \varepsilon = E_r. \tag{3.1}$$

Here ε is the kinetic energy of the unbound continuum state and E_r is the energy difference between the ground electronic state and the vibrational level of the excited electronic state. ε is typically small at low temperatures and of order $\varepsilon \simeq k_B T$. We may also define the detuning Δ

$$\Delta \equiv E_r - \hbar\omega_1. \tag{3.2}$$

3.1.1 Transition probabilities and selection rules

Temperature is related to translation, vibration and rotation in a diatomic molecule. Translation is the main contributor, with vibration and rotation following in that order. All molecules produced from translationally cold atoms will be equally translationally cold. Rotational heating is not a problem since only the lowest partial waves can contribute at ultracold temperatures. However, we also want to produce vibrationally cold molecules. It is thus of some importance that the vibrational levels that are populated through spontaneous decay are as low in energy as possible. To determine which vibrational levels that will be populated, we need to calculate the transition probabilities for the spontaneous decay. The probability for a spontaneous transition between $|\psi_i\rangle$ and $|\psi_k\rangle$ is given by

$$A_{ik} = \frac{\omega_{ik}^3}{3\varepsilon_0 \pi c^3 \hbar} |\langle \psi_k | \hat{\mathbf{d}} | \psi_i \rangle|^2, \tag{3.3}$$

which simplifies by introducing the fine structure constant $\alpha \equiv \frac{e^2}{4\pi\varepsilon_0 \hbar c}$,

$$A_{ik} = \frac{4\alpha}{3e^2c^2} \omega_{ik}^3 |\langle \psi_k | \hat{\mathbf{d}} | \psi_i \rangle|^2. \tag{3.4}$$

In equations (3.3) and (3.4) the dipole operator $\hat{\mathbf{d}}$ is defined as

$$\hat{\mathbf{d}} \equiv -e \sum_i \hat{\mathbf{r}}_i + Z_1 e \hat{\mathbf{R}}_1 + Z_2 e \hat{\mathbf{R}}_2, \tag{3.5}$$

in the molecular reference frame. The sum is over the electrons, and all other symbols in equations (3.3)-(3.5) have their usual meaning. $\mathbf{R}_1$ and $\mathbf{R}_2$ are the position vectors to the two nuclei. For a homonuclear molecule the nuclear part of equation (3.5) will be zero.

Since we are working in the Born-Oppenheimer approximation we can separate the total wavefunction ψ in two parts, an electronic ψ_e and a nuclear ψ_n, $\psi = \psi_e \psi_n$. We can therefore write for the matrix element

$$\mathbf{D}_{ik} \equiv \langle \psi_k | \hat{\mathbf{d}} | \psi_i \rangle = \langle \psi_n^k \psi_e^k | \hat{\mathbf{d}} | \psi_e^i \psi_n^i \rangle = \langle \psi_n^k | \hat{\mathbf{d}}(R) | \psi_n^i \rangle, \tag{3.6}$$

with

$$\hat{\mathbf{d}}(R) \equiv \int \psi_e^{k*} \hat{\mathbf{d}} \psi_e^i \mathrm{d}\tau_{\mathrm{el}}. \tag{3.7}$$

$\mathrm{d}\tau_{\mathrm{el}}$ indicates integration over the spatial electronic coordinates. From the previous chapter, equation 2.73 we have $\psi_n = \frac{1}{R} \psi_v \psi_J$. Thus, we find from equation (3.6) in spherical coordinates

$$\mathbf{D}_{ik} = \int \psi_v^{k*} \hat{\mathbf{d}}(R) \psi_v^i \mathrm{d}R \int \int \psi_{J_k} \psi_{J_i} \sin\phi \mathrm{d}\phi \mathrm{d}\theta. \tag{3.8}$$

We will be concerned with the first integral. The second integral does not depend on the vibrational levels involved, and is therefore not relevant for the population of them. We merely note that summing over M_{J_k} and M_{J_i} and squaring, gives the so-called *Hönl-London factor*. The matrix elements we will consider in the following are therefore

$$\mathbf{D}_{vv'} = \langle v' | \hat{\mathbf{d}}(R) | v \rangle, \tag{3.9}$$

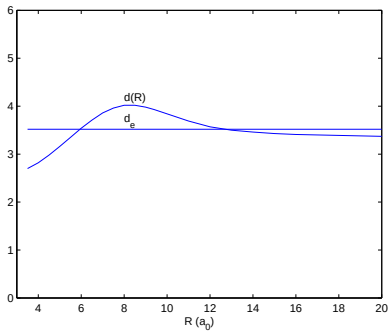

Figure 3.2. *$d(R)$ and the zero order Taylor approximation d_e for the electronic transition $^1\Sigma_u^+ \rightarrow ^1\Sigma_g^+$ in Li_2*

with $|v\rangle$ and $|v'\rangle$ as shorthand notation for $|\psi_v^i\rangle$ and $|\psi_v^k\rangle$ respectively. $|v\rangle$ and $|v'\rangle$ are in the following assumed to be vibrational levels corresponding to different electronic states.

Sometimes the spontaneous decay is expressed in terms of Franck-Condon factors. See for instance [35] and [36]. The Franck-Condon factor $p_{vv'}$ is simply defined as the overlap integral

$$p_{vv'} = |\langle v'|v\rangle|^2 = \left| \int \psi_{v'}^* \psi_v \mathrm{d}R \right|^2. \tag{3.10}$$

Consider again equation (3.9) and use a Taylor expansion of one of the components of $\mathbf{d}(R)$, for example d_z

$$d_z(R) = d_z(R_E) + \left.\frac{\mathrm{d}d_z}{\mathrm{d}R}\right|_{R=R_E} (R - R_E) + \cdots . \tag{3.11}$$

If we only keep the zero order term we find

$$D_{vv'} \approx d_z(R_e)\langle v'|v\rangle. \tag{3.12}$$

This expression may represent a reasonable approximation since $d(R)$ is expected to vary slowly with R. Our calculations confirm this, and $d_z(R)$ is found to vary slowly with R for the transition $A^1\Sigma_u^+ \rightarrow X^1\Sigma_g^+$ as shown in figure 3.2.

Not all electronic states can be active participants in photoassociation experiments. Electronic states with dipole-forbidden transitions to the ground state are useless for such experiments. For these transitions the matrix elements $\langle\psi_k|\hat{\mathbf{d}}|\psi_i\rangle$ will be zero. Which transitions $\phi_i \rightarrow \phi_k$ that are dipole forbidden can be deduced from general symmetry considerations, see for instance [27]. The selection rules that follows from such considerations are

$$\Delta J = 0, \pm 1, \qquad \Delta\Lambda = 0, \pm 1, \qquad \Delta\Sigma = 0, \qquad \Delta S = 0, \qquad g \leftrightarrow u \tag{3.13}$$

These selection rules apply when the respective quantum numbers are well-defined.

If we neglect the Hönl-London factor we can write the spontaneous decay rate as

$$A_{v'v''} = \frac{4\alpha}{3e^2c^2}\omega_{v'v''}|\langle v''|\mathbf{d}(R)|v'\rangle|^2, \tag{3.14}$$

for the decay from vibrational level v' of an excited state to vibrational level v'' in a lower state. If we on the other hand is interested in the total spontaneous decay rate from an excited

state vibrational level v' we find

$$A_{v'} = \frac{4\alpha}{3e^2c^2}\left(\sum_{v''}\underbrace{\omega^3_{v'v''}|\langle v''|\hat{\mathbf{d}}(R)|v'\rangle|^2}_{\text{bound-bound decay}} + \int\underbrace{\omega^3_{v'\varepsilon}|\langle u_\varepsilon|\hat{\mathbf{d}}(R)|v'\rangle|^2\mathrm{d}\varepsilon}_{\text{bound-free decay}}\right). \tag{3.15}$$

Thus, the spontaneous decay rate split in two parts, either to the continuum of states or to the bound vibrational levels v''. To find the total decay rate, we sum over the discrete vibrational levels and integrate over the continuum functions $|u_\varepsilon\rangle$ of the ground state asymptote. These continuum functions satisfies (see also equation (2.74))

$$\left(\frac{\mathrm{d}^2}{\mathrm{d}R^2} + k^2 - \frac{2\mu}{\hbar^2}E_e(R) - \frac{J(J+1)}{R^2}\right)u_\varepsilon(R) = 0, \tag{3.16}$$

with $u_\varepsilon(R)$ normalized to obey

$$\int_0^\infty u^*_{\varepsilon'}(R)u_\varepsilon(R)\mathrm{d}R = \delta(\varepsilon' - \varepsilon). \tag{3.17}$$

$\delta(x)$ is the Dirac delta function. Equation (3.16) is impossible to solve analytically with $E_e(R)$. An asymptotic form of the solution is however possible to obtain, since $E_e(R)$ can be taken as a constant V_0 for large R values. Equation (3.16) simplifies further if $J = 0$, and can then be solved by inspection

$$u_\varepsilon = A\sin(\kappa R + \delta(\kappa)), \tag{3.18}$$

with A as an unknown constants and δ as the phase shift. $\kappa^2 = \frac{2\mu}{\hbar^2}(\varepsilon - V_0)$. We will return to equation (3.16) and its solutions in chapter 5, then related to scattering lengths. However, the solutions obtained there will not obey the normalization in equation (3.17). We have made several attempts to calculate matrix elements such as $\langle v|\hat{\mathrm{d}}_i(R)|u_\varepsilon\rangle$, but this has not yet been successful. The motivation for these attempts is to predict exactly how much of the decay that are to the continuum states. The problem is to obtain solutions with the correct normalization. Equation (3.16) is rather easy to solve numerically, but the normalization is problematic.

An attempt to use vibrational eigenfunctions $|v\rangle$ with energies above the dissociation limit failed. The results were rather unstable and not in agreement with other results reported for similar matrix elements [60] . This approach was therefore abandoned, and wavefunctions u_ε with correct normalization were never obtained.

The bound-free matrix elements we were unable to calculate represents transitions where molecules are lost. This term should therefore be minimized. However, most often the number of atoms lost by this mechanism is substantial (>90%).

Molecules in the excited vibrational level v' may also return to the ground state by *stimulated* emission. This is nothing we will be concerned with, we simply state that the probability for this process is proportional to the photon flux and the square of the matrix element $\langle u_\varepsilon|\hat{\mathbf{d}}(R)|v'\rangle$ in the simplest model [44]. Usually this represents a modest contribution to the total decay.

3.1.2 Two color photoassociation

The idea of two color[1] photoassociation came originally from Band and Julienne [38] in 1995. The main motivation for their proposal was the possibility of producing vibrationally colder molecules than what was possible by one color photoassociation. Already in 1987 Torsheim *et al*. [33] had found that sometimes most of the bound-bound transitions lead to states with high vibrational quantum numbers. At the same time much of the spontaneous emission was to continuum states. Band and Julienne sought to minimize these problems by the use of *two* lasers instead of one. Two lasers makes it possible to create cold molecules in a two step process. In the original paper Band and Julienne described a two-color process with sodium atoms.

Similar proposals now exists also for Lithium. Côté and Dalgarno [36] have proposed a two color scheme for producing cold triplet molecules. The first laser with frequency ω_1 is used to photoassociate two ^{7}Li atoms,

$$^7\mathrm{Li} + {}^7\mathrm{Li} + \hbar\omega_1 \rightarrow {}^7\mathrm{Li}_2(1^3\Sigma_g^+, v' = 58). \tag{3.19}$$

A significant fraction of the bound-bound decay from this level is to the $v'' = 10$ level of the $^3\Sigma_u^+$ electronic state,

$$1^3\Sigma_g^+(v' = 58) \rightarrow 1^3\Sigma_u^+(v'' = 10) + \hbar\omega_s. \tag{3.20}$$

A second laser is now used to excite molecules into $v' = 10$ of the $1^3\Sigma_g^+$ electronic state,

$$1^3\Sigma_u^+(v'' = 10) + \hbar\omega_2 \rightarrow 1^3\Sigma_g^+(v' = 10). \tag{3.21}$$

From $v' = 10$ of the $1^3\Sigma_g^+$ electronic state, more than 50% of the bound-bound decay is to $v'' = 0$ of the $1^3\Sigma_u^+$ state,

$$1^3\Sigma_g^+(v' = 10) \rightarrow a^3\Sigma_u^+(v'' = 0) + \hbar\omega_s'. \tag{3.22}$$

See also figure 3.3 for an illustration of this two photon process.

All two color experiments rely heavily on a ”R-transfer”. A ”R-transfer” usually occurs through an excitation with the second laser that changes the internuclear distance R of the molecule. This distance should be changed to be similar to the distance in the low vibrational levels of the ground state. A ”R-transfer” will increase the spontaneous decay to the lower ground state vibrational levels by increasing the overlap between the wavefunctions.

In comparison with the one-color scheme and the problems with high vibrational quantum numbers, two-color photoassociation may seem like a big improvement. The efficiency of the process can however be questioned. Relying on a number of excitations and decay processes will cause extensive loss of molecules. Sometimes excitations to high laying electronic states are also used as an effective way to induce a ”R-transfer”. This again may open for a new problem; will the spontaneous decay mainly populate other electronic states than the ground state? If there exists several dipole allowed electronic states, this is certainly a possibility. It is however often possible to argue that most of the decay will be to the ground state by looking at the spontaneous decay rates. Let us assume there exists two electronic states ψ_{e1} and ψ_{e2} with allowed transition dipole moments between them, and

[1] The name two color photoassociation reflects the fact that two lasers with different frequencies are used.

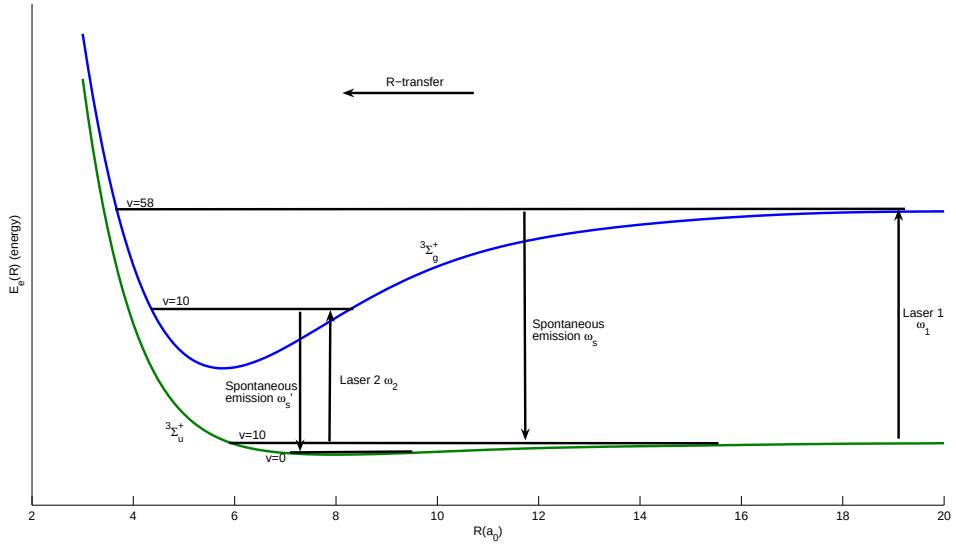

Figure 3.3. *Two photon photoassociation for* $^7\mathrm{Li}_2$ *as proposed in [36]. This is only a sketch and the vibrational levels are not correctly positioned. Two color photoassociation processes may also involve three different electronic states.*

$E_{\mathrm{e1}}(R) > E_{\mathrm{e2}}(R)$. In addition ψ_{e1} can decay to the ground state, ψ_{X}. The decay rates from ψ_{e1} to ψ_{X} and ψ_{e2} are respectively

$$A_{1\mathrm{X}} \propto \omega_{1\mathrm{X}}^3 |\langle \psi_{\mathrm{X}} | \hat{\mathbf{d}}(R) | \psi_{\mathrm{e1}} \rangle|^2, \tag{3.23}$$

$$A_{12} \propto \omega_{12}^3 |\langle \psi_{\mathrm{e2}} | \hat{\mathbf{d}}(R) | \psi_{\mathrm{e1}}|^2. \tag{3.24}$$

We may now argue that the decay from ψ_{e1} will be dominantly to the ground state ψ_{X} because $\omega_{1\mathrm{X}}^3$ will be larger than ω_{12}^3. This argument assumes that there are no big differences in the electronic dipole moments. Still, these considerations signals that there necessarily will be some loss of molecules. Often this is the prize to pay to produce vibrationally really cold molecules.

The production rates for cold molecule production by two-photon photoassociation are typically somewhat less than the corresponding rates for one-color photoassociation. It has however been reported production rates as high as 10^5 molecules per second with a two color scheme in Na_2. Two color photoassociation has also been demonstrated in Rb_2.

Even though two-color photoassociation may be useful to increase production of cold molecules in favorable vibrational levels, there still exits limitations. Two-color photoassociation, just as one color photoassociation, rely heavily on spontaneous emission. Spontaneous emission will in general populate series of vibrational levels. Thus, the outcome will be molecules with different vibrational quantum numbers and perhaps even molecules in different electronic states. If this becomes a big problem, it may call for a way to remove the vibrationally hot molecules. This has also motivated cold molecule production that rely on stimulated emission, instead of spontaneous emission [36].

3.2 Producing ultracold $^6Li_2$ molecules

In this section we point out the possible photoassociation schemes in $^6Li_2$, and we calculate matrix elements to predict the decay spread to the various vibrational levels of the ground state. First we calculate the potential curves of the ten lowest electronic states, with corresponding vibrational levels.

3.2.1 Potential curves for $^6Li_2$

With the programs and methods described in the previous chapter we have been able to obtain the potential curves for the states asymptotically corresponding to the ^2S + ^2S and ^2S + ^2P atomic limits.

The electronic states corresponding to the ^2S + ^2S limit have

$$\Lambda = 0, \tag{3.25}$$
$$S = \{0, 1\}, \tag{3.26}$$

since $l_1 = l_2 = 0$ and $s_1 = s_2 = 1/2$ ($\Lambda = |M_L|$ and S is the total spin). Thus, the possible electronic states corresponding to the $^2S + {}^2S$ asymptote are $^1\Sigma$ and $^3\Sigma$. Considering now the $^2S + {}^2P$ asymptotic limit we find

$$\Lambda = \in \{1, 0\}, \tag{3.27}$$
$$S = \in \{0, 1\}, \tag{3.28}$$

yielding $^1\Sigma$, $^3\Sigma$, $^1\Pi$ and $^3\Pi$ electronic states. Further we need to obtain the eigenvalues for the electron inversion operator $\hat{I}_e$ and the reflection operator $\hat{\sigma}_v$ for all the electronic states. It is in general not an easy task to find corresponding eigenvalues for the operators $\hat{\mathbf{S}}^2$, $\hat{\sigma}_v$, $\hat{I}_e$ to characterize the relevant symmetries of the electronic states. Thus we refer to Landau and Lifshiftz [1] for a further discussion on this point. In table 3.1 we list the result; all the electronic states corresponding to the ^2S+^2S and ^2S+^2P dissociation limits.

^2S+^2S	$1^1\Sigma_g^+$, $1^3\Sigma_u^+$
^2S+^2P	$2^1\Sigma_g^+$, $1^1\Sigma_u^+$, $1^3\Sigma_g^+$, $2^3\Sigma_u^+$, $1^1\Pi_g$, $1^1\Pi_u$, $1^3\Pi_g$, $1^3\Pi_u$

Table 3.1. *Electronic states in* Li_2 *with corresponding dissociation limits.*

With the Hartree-Fock program and MultiMOD, both described in chapter 2, the potential curves for the ten electronic states in table 3.1 were worked out. Due to limitations in the Hartree-Fock program we have not been able to calculate potential curves for internuclear distances larger than approximately $20a_0$. The curves are displayed in figure 3.4.

The potential curves in figure 3.4 are expected to be very accurate. Especially the singlet and triplet ground state curves should be reliable. Generally the higher laying curves is probably the most inaccurate. This is because it is harder to get an adequate model space for the higher laying states. Especially the $2^3\Sigma_u^+$ electronic state was hard to obtain. Many data points could not be calculated due to singularities in the perturbation expansion (intruders).

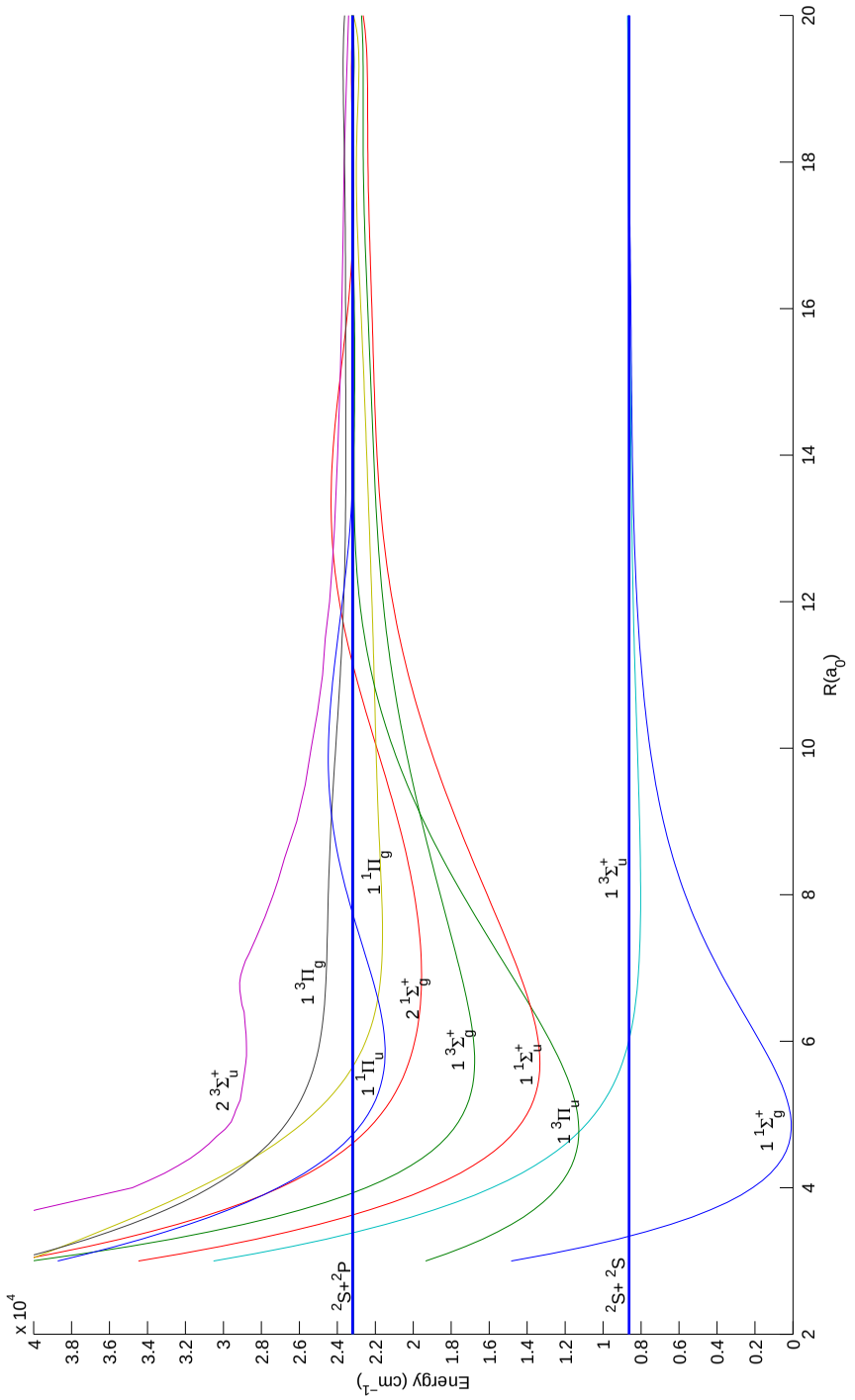

Figure 3.4. *Potential curves for all electronic states corresponding to the* $^2S+^2S$ *and* $^2S+^2P$ *dissociation limits in* $^6Li_2$.

This is however an electronic state completely useless for photoassociation experiments and cold molecule production.

Li_2 is one of the spectroscopically best known molecules in the literature. Thus, it has been possible to compare the potential curves obtained with curves calculated by others. Konowalow and Fish [40],[39] have published potential curves for the 26 lowest lying states in Li_2. Their curves are also found from *ab inito* calculations and are known to be very accurate, the curves are in agreement with data obtained experimentally and are regarded as "correct". Comparing the curves obtained by Konowalow and Fish with the ones calculated here, reveals the differences in table 3.2.

State	Deviations
$1^1\Sigma_g^+$	No known.
$1^3\Sigma_u^+$	No known.
$1^3\Pi_u$	No substantial deviations known.
$1^1\Sigma_u^+$	No known.
$1^3\Sigma_g^+$	No substantial deviations known.
$2^1\Sigma_g^+$	Calculated to have about $600\mathrm{cm}^{-1}$ higher dissociation energy than what is found in [39].
$1^1\Pi_g$	Calculated to have about $500\mathrm{cm}^{-1}$ higher dissociation energy than what is found in [39].
$1^1\Pi_u$	No known.
$1^3\Pi_g^+$	No known.
$2^3\Sigma_u^+$	No known (our curve has few data points).

Table 3.2. *Comparison between our potential curves and the curves found by Konowalow and Fish [40] for the ten lowest laying states in* Li_2.

The comparison shows that the deviations are small, and that our work yield similar accuracies. The ground state dissociation energy tends to be accurately known. It is given as $D_e = 8517.0369\mathrm{cm}^{-1}$, see [42]. Our calculated value is $D_e = 8552.6\mathrm{cm}^{-1}$.

3.2.2 Electronic transition dipole moments

The electronic dipole moments $\mathbf{d}(R)$ (see also equation (3.7)) between states of interest are calculated. We write the electronic dipole operator $\hat{\mathbf{d}}$ as (see also equation (3.5))

$$\hat{\mathbf{d}} = e(\hat{x}\mathbf{e}_x + \hat{y}\mathbf{e}_y + \hat{z}\mathbf{e}_z), \tag{3.29}$$

where $\mathbf{e}_i$ are unit vectors in the respective directions. For transitions with $\Delta\Lambda = 0$, only the z component will contribute. For transitions with $\Delta\Lambda = 1$, only the x and y components will contribute. In table 3.3 we list $|\langle\psi_2|z|\psi_1\rangle|^2$ for $\Lambda = 0$ transitions and $|\langle\psi_2|x|\psi_1\rangle^2 = |\langle\psi_2|y|\psi_1\rangle|^2$ for the $\Lambda = 1$ transition. Some entries in table 3.3 could not be calculated, due to divergence in the perturbation series. This divergence occurs for R-values where electronic states of different symmetry intersects. We therefore believe that the divergence may be due to only a finite representation of the symmetry of each state, causing a divergence when two electronic states have the same energy (although their symmetries are different). There are also some

problems with the software (MultiMod and Hartree-Fock program) we are using for large R values.

$R(a_0)$	$1^1\Sigma_u^+ \rightarrow 1^1\Sigma_g^+$	$1^3\Sigma_g^+ \rightarrow 1^3\Sigma_u^+$	$1^1\Pi_u \rightarrow 1^1\Sigma_g^+$
3.5	8.34	13.12	2.90
4.0	9.01	13.58	3.12
4.4	9.80	-	3.27
5.0	11.34	17.09	3.50
5.5	12.50	17.15	3.63
6.0	13.62	17.23	3.64
6.4	14.87	17.18	3.81
7.0	15.99	17.17	3.92
7.5	17.11	17.02	4.05
8.0	17.48	16.76	4.28
8.5	17.55	16.21	4.49
9.0	17.39	15.65	-
9.5	16.87	15.60	4.72
10.0	16.29	15.02	4.88
11.0	15.44	15.08	4.91
12.0	14.67	15.11	5.12
13.0	13.53	14.87	5.16
14.0	13.21	14.62	5.19
15.0	13.07	14.15	5.28
16.0	12.96	14.21	5.34
17.0	12.96	14.22	5.33
18.0	12.94	14.20	5.33
19.0	-	14.19	5.33
20.0	12.85	14.27	5.33

Table 3.3. *Calculated electronic transition moments* $[\mathbf{D}(R)]^2$*. The moments are given in terms of atomic units,* a_0^2*. Entries that could not be obtained are indicated with -.*

The electronic transition moments are compared with values obtained by Ratcliff *et al*. in [41]. The potentials obtained by Konowalow and Fish is used in their calculations. The results in table 3.3 are in good agreement with [41]. However, there are some minor differences in all the transition moments, typically they find somewhat lower values than what is calculated in our work. The differences are however not large, and are of no importance for the calculation of matrix elements such as $\langle v'|d(R)|v\rangle$.

3.2.3 Vibrational levels

Vibrational levels for all bound electronic states have been calculated. See chapter 2, section 4.1 for a description of the algorithm used.

To have knowledge of the positions to the vibrational levels is crucial for doing photoassociation. All vibrational levels corresponding to the same electronic state is given a quantum number v, starting with $v = 0$ from the lowest level of each electronic state. The

vibrational levels will fill up each electronic state and go over into continuum levels above the dissociation limit. In the ground state we find the vibrational levels as shown in figure 3.5. We see from the figure that the vibrational levels at the top lay closer and closer together before going over to continuum states.

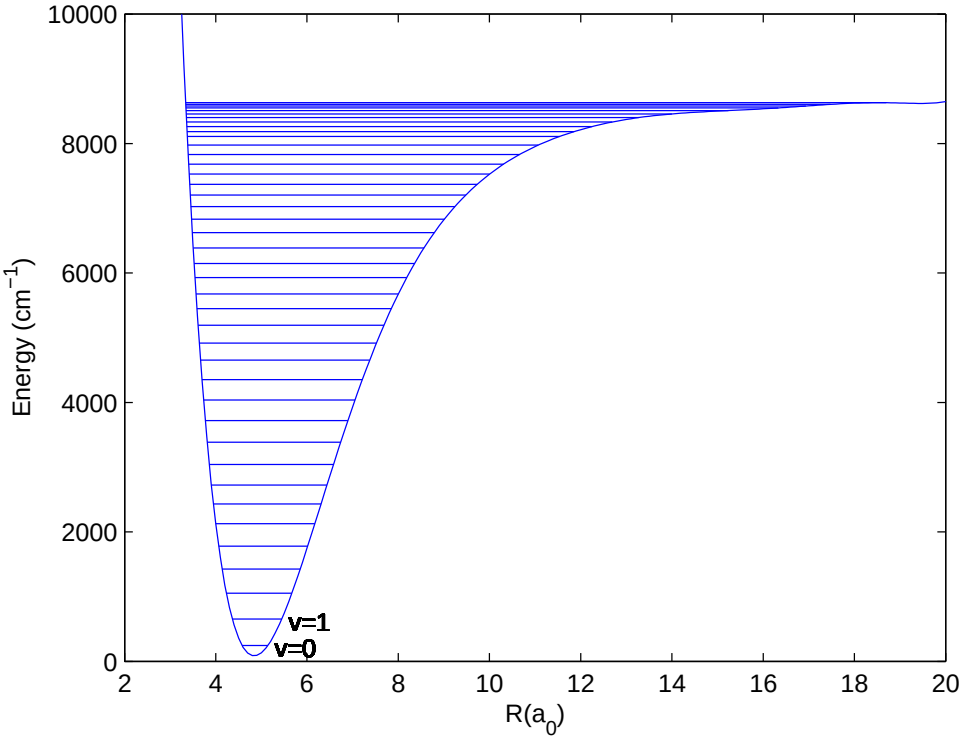

Figure 3.5. *Vibrational levels in the ground molecular state. The $v = 0$ and $v = 1$ levels are explicitly marked on the figure. The 41 lowest vibrational levels are shown.*

All calculated vibrational levels for all electronic states are tabulated in table 3.4.

Caution: Table 3.4 must be read downwards at all times. The vibrational levels of one electronic state are always tabulated downwards.

Note however, that the number of vibrational levels in each state is uncertain, due to the fact that by extending the potential curves to higher R-values, the number of bound levels close to the continuum might increase. The vibrational levels tabulated below are found with potential curves ranging between $R = 3.50a_0$ and $R = 20.00a_0$. Two exceptions to this are the $1^1\Sigma_u^+$ and $1^3\Sigma_g^+$ states in which the potentials were extended to $30\mathrm{a}_0$ with values taken from [39]. This was necessary because these electronic states approaches the continuum limit very slowly, by extending the potential we were able to calculate also the topmost vibrational levels.

Vibrational levels

Continued on next page

$1^1\Sigma_g^+$ (0)		$1^3\Sigma_u^+$ (7991cm^{-1})		$1^3\Pi_u$ (12022cm^{-1})		$1^1\Sigma_u^+$ (13313cm^{-1})	
v	Energy (cm^{-1})	v	Energy(cm^{-1})	v	Energy(cm^{-1})	v	Energy(cm^{-1})
0	245.16	0	107.51	0	168.40	0	148.69
1	652.81	1	215.98	1	437.25	1	404.67
2	1053.73	2	283.39	2	770.02	2	702.23
3	1425.16	3	368.95	3	1113.00	3	976.89
4	1780.46	4	431.67	4	1446.74	4	1256.62
5	2126.01	5	483.76	5	1784.18	5	1529.40
6	2430.69	6	531.62	6	2113.97	6	1790.23
7	2722.71	7	560.91	7	2440.79	7	2043.35
8	3042.66	$2^1\Sigma_g^+$ (19283cm^{-1})		8	2762.46	8	2291.56
9	3385.72	v	Energy(cm^{-1})	9	3080.14	9	2534.61
10	3718.60	0	139.36	10	3392.05	10	2775.18
11	4037.42	1	389.70	11	3696.24	11	3014.92
12	4353.23	2	618.91	12	3989.39	12	3254.03
13	4655.85	3	841.65	13	4265.70	13	3491.31
14	4918.79	4	1049.44	14	4539.24	14	3726.37
15	5193.49	5	1223.95	15	4827.03	15	3959.21
16	5449.61	6	1389.03	16	5109.38	16	4189.48
17	5677.11	7	1553.09	17	5378.65	17	4416.35
18	5939.35	8	1712.78	18	5651.80	18	4640.22
19	6146.73	9	1875.97	19	5916.33	19	4860.03
20	6387.61	10	2042.44	20	6182.18	20	5075.96
21	6624.36	11	2209.17	21	6453.40	21	5288.32
22	6832.92	12	2373.30	22	6729.38	22	5496.65
23	7027.55	13	2532.15	23	7009.78	23	5700.69
24	7205.92	14	2684.22	24	7286.10	24	5900.12
25	7371.42	15	2832.16	25	7556.91	25	6094.60
26	7528.65	16	2980.77	26	7815.11	26	6283.22
27	7672.22	17	3134.43	27	8059.08	27	6466.13
28	7831.28	18	3293.16	28	8297.95	28	6643.92
29	7976.07	19	3455.63	29	8533.62	29	6816.61
30	8110.58	20	3619.26	30	8764.95	30	6983.93
31	8183.75	21	3778.23	31	8995.13	31	7146.49
32	8261.92	22	3848.21	32	9221.96	32	7304.19
33	8332.86	$1^1\Pi_g$ (21496cm^{-1})		33	9448.59	33	7456.96
34	8401.41	v	Energy(cm^{-1})	34	9672.72	34	7604.11
35	8457.75	0	183.377	35	9893.28	35	7745.30
36	8509.77	1	327.958	36	10110.3	36	7879.84
37	8550.63	2	420.096	37	10322.2	37	8006.75
38	8579.40	3	524.361	38	10529.0	38	8126.51
39	8605.38	4	594.926	39	10729.9	39	8240.10
40	8631.17	5	647.946	40	10923.5	40	8348.18

Continued on next page

$1^3\Sigma_g^+$ (16621cm^{-1})		6	709.598	41	11108.5	41	8451.41
v	Energy(cm^{-1})	7	767.358	42	11282.9	42	8548.48
0	150.27	8	824.240	43	11443.2	43	8638.10
1	444.37	9	881.424	44	11584.9	44	8719.07
2	728.05	10	938.301	45	11691.3	45	8790.85
3	1006.57	11	995.548	46	11741.3	46	8852.89
4	1251.05	12	1051.62	47	11791.4	47	8900.57
5	1443.15	13	1106.00	48	11833.3	48	8936.98
6	1664.92	14	1159.09	49	11869.9	49	8975.97
7	1882.75	15	1210.79	50	11900.4	50	9016.98
8	2083.07	16	1261.36	51	11926.3	51	9060.29
9	2289.63	17	1310.82	52	11946.8	52	9105.82
10	2477.95	18	1459.27	53	11966.8	53	9153.89
11	2669.40	19	1406.66	54	11986.0	54	9204.67
12	2852.76	20	1452.94	55	12004.4	55	9250.14
13	3034.11	21	1497.88	56	12021.7	56	9300.21
14	3211.33	22	1541.24			57	9349.16
15	3382.91	23	1582.64			58	9396.89
16	3553.83	24	1622.23			59	9442.62
17	3721.15	$1^1\Pi_u$ (21004cm^{-1})				60	9485.580
18	3884.24	v	Energy(cm^{-1})			61	9526.18
19	4040.15	0	478.791			62	9560.74
20	4185.04	1	1047.95			63	9586.11
21	4321.90	2	1431.35			64	9608.51
22	4455.46	3	1720.03			65	9633.32
23	4588.00	4	1965.97			66	9659.71
24	4721.31	5	2204.36			67	9687.04
25	4854.96	6	2404.40			68	9715.00
26	4985.93	7	2588.10			69	9742.82
27	5109.89	8	2749.80			70	9770.44
28	5202.55	9	2870.07			71	9798.09
29	5259.79	10	2913.73			72	9825.67
30	5344.27	11	3019.20			73	9852.97
31	5422.85	12	3080.80			74	9880.36
32	5501.07	13	3213.79			75	9907.71
33	5573.68	14	3243.93			76	9935.52
34	5641.08	15	3405.68			77	9964.17
35	5705.56	16	3442.49			78	9993.89
36	5766.01	17	3543.89			79	10002.50
37	5823.94					80	10005.70
38	5877.13						
39	5926.28						
40	5971.38						

Continued on next page

41	6013.04						
42	6051.66						
43	6087.07						
44	6119.28						
45	6148.62						
46	6176.22						
47	6203.56						
48	6231.06						
49	6258.75						
50	6286.35						
51	6313.96						
52	6341.77						
53	6369.75						
54	6397.81						
55	6425.86						
56	6453.75						
57	6481.58						
58	6509.32						
59	6536.99						
60	6564.46						
61	6591.57						
62	6618.14						
63	6644.16						
64	6669.83						
65	6695.88						

Table 3.4. *Vibrational levels calculated for the bound electronic states in $^6Li_2$. All numbers are in cm^{-1}, measured above minima of each electronic state. The electronic state minimas are given in parentheses behind the spectroscopic notation of all electronic states. All minimas are measure above ground state minima. The colored vibrational level of the $1^1\Pi_u$ electronic state will be closely investigated in the next chapter.*

3.2.4 One color photoassociation in Li_2

We investigate further one color photoassociation and look for possible routes to produce both singlet ground state molecules and triplet $1^3\Sigma_u^+$ state molecules. From the dipole selection rules (3.13) and the potential curves in figure 3.4, we single out three possible schemes

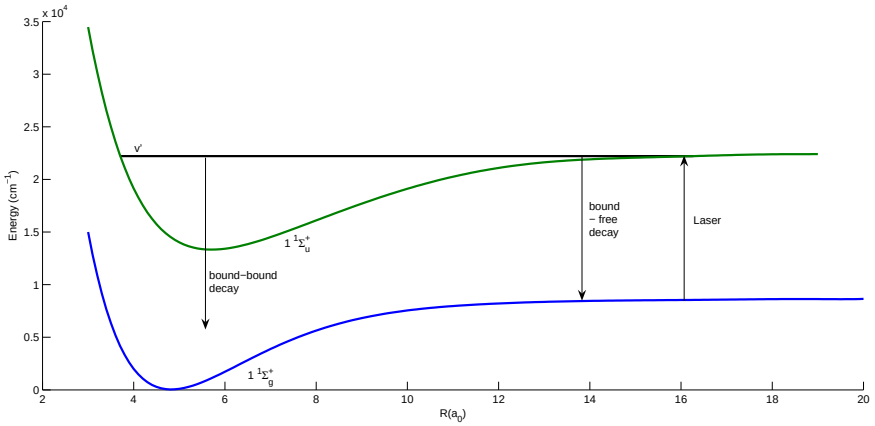

Figure 3.6. *A laser is used to photoassociate two atoms to a bound vibrational level v' of the excited electronic state $1^1\Sigma_u^+$. Cold ground state molecules are formed as molecules decay to a vibrational level v'' of the ground state.*

for cold molecule production,

$$\begin{aligned} &1)\ \mathrm{Li} + \mathrm{Li} + \hbar\omega_1 \rightarrow 1^1\Sigma_u^+(v'), \\ &\quad 1^1\Sigma_u^+(v') \rightarrow \hbar\omega_s + X^1\Sigma_g^+(v''), \end{aligned} \tag{3.30}$$

$$\begin{aligned} &2)\ \mathrm{Li} + \mathrm{Li} + \hbar\omega_2 \rightarrow 1^1\Pi_u^+(v'), \\ &\quad 1^1\Pi_u(v') \rightarrow \hbar\omega_s' + 1^1\Sigma_g^+(v''), \end{aligned} \tag{3.31}$$

$$\begin{aligned} &3)\ \mathrm{Li} + \mathrm{Li} + \hbar\omega_3 \rightarrow 1^3\Sigma_g^+(v'), \\ &\quad 1^3\Sigma_g^+(v') \rightarrow \hbar\omega_s'' + 1^3\Sigma_u^+(v''). \end{aligned} \tag{3.32}$$

$\omega_1, \omega_2, \omega_3$ are laser frequencies, while $\omega_s, \omega_s', \omega_s''$ are frequencies of the photons emitted in the different spontaneous emission processes. Note that transition 3) produces triplet ground state molecules. The $1^1\Pi_u$ state involved in scheme 2) has a maximum on its potential for R values in between $8 - 14a_0$, making it hard to access the vibrational levels. Transition 2 will be closely investigated in the next chapter, and for now we restrict the treatment to transitions 1) and 3).

3.2.5 Cold ground state molecules with $A^1\Sigma_u^+(v') \rightarrow X^1\Sigma_g^+(v'')$ transitions

The cold molecule production scheme to be examined is schematically illustrated in figure 3.6. We will especially investigate the decay process

$$1^1\Sigma_u^+(v') \rightarrow X^1\Sigma_g^+(v'') + \hbar\omega_s, \tag{3.33}$$

for all vibrational levels v' and v''. Dipole matrix elements $\langle v''|d(R)|v'\rangle$, and Franck-Condon factors $\langle v''|v'\rangle$ have been calculated for all possible combinations of v' and v''. In these calculations we have extended the potential of the $X^1\Sigma_g^+$ electronic state to $30a_0$. The potential was at long range assumed to be

$$V(R) = \frac{C_6}{R^6}, \tag{3.34}$$

with a C_6 value taken from [48]. A long range potential of this form is often used to describe the van-der Waals interactions between the two atoms in the molecule. The van-der Waals interaction exists also for small internuclear distances, but are then completely suppressed by other interactions. For a more complete discussion of the van-der Waals interactions, see Landau and Lifshitz [1], page 343. We will however also use the result that two similar atoms in different states have a van-der Waal interaction proportional to $1/R^3$,

$$V(R) = \frac{C_3}{R^3} + \frac{C_6}{R^6}. \tag{3.35}$$

Sometime we will also include higher order terms like $\frac{C_8}{R^8}$ and $\frac{C_{10}}{R^{10}}$. By extending the ground state potential with equation (3.34) we were able to include also the highest vibrational levels. We also tried to extend both the excited state potential (with equation (3.35)) and the ground state potential beyond $30a_0$, but it seemed sufficient to stop at $30a_0$.

In $1^1\Sigma_u^+$ all vibrational levels $v' > 47$ can be reached at relatively long range ($v' = 47$ at $R \approx 14a_0$). This indicates a large number of vibrational levels accessible for photoassociation. The possible spontaneous decay from the $1^1\Sigma_u^+$ state is only to the ground state. There exists no other dipole allowed electronic states to compete with the ground state. However, the total decay will be both to the continuum (bound-free) and to different vibrational levels in the ground state (bound-bound). To estimate the decay to the continuum (bound-free) we assume that the probability of making a (bound-bound) transition $v' \rightarrow v''$ is given by the corresponding Franck-Condon factor $p_{v'v''} \equiv |\langle v''|v'\rangle|^2$. If we assume that a vibrational level will decay to either the continuum or to a bound vibrational state, this immediately yields

$$1 \simeq \sum_{v''} p_{v'v''} + P(\varepsilon''). \tag{3.36}$$

$P(\varepsilon'')$ is the probability for decay to the continuum states and $\sum_{v''} p_{v'v''}$ is the fraction of decay that is bound-bound. $P(\varepsilon'')$ can now be simply calculated as

$$P(\varepsilon'') = 1 - \sum_{v''} p_{v'v''}. \tag{3.37}$$

We are interested in what fraction of the decay that is bound-bound from the higher laying vibrational levels of the $1^1\Sigma_u^+$ state, since these vibrational levels are candidates for photoassociation. Of interest is also the decay rates $A_{v'v''}$. We also calculate the total bound-bound decay rates, $A_{v'} = \sum_{v''} A_{v'v''}$ for the uppermost vibrational levels $|v'\rangle$ in $1^1\Sigma_u^+$, along with the bound-bound fractions $p_{v'} = \sum_{v''} p_{v'v''}$ for these levels. The results are found in table 3.5.

As expected the bound-free decay from the highest excited vibrational levels (of $1^1\Sigma_u^+$) is dominant. However, about ten percent of the decay is bound-bound also from the highest excited vibrational levels we have been able to study. This is certainly much better than what is found for many other alkalis [36], still the bound-free decay is large and causes extensive loss of molecules.

Figure 3.7 shows the total bound-bound spontaneous emission decayrates $A_{v'} = \sum_{v''} A_{v'v''}$, from all excited levels v', while figure 3.8 shows the fraction of spontaneous decay that is bound-bound, $p_{v'} = \sum_{v''} p_{v'v''}$, as a function of vibrational levels v'.

Figure 3.7 shows a decrease in the total bound-bound spontaneous emission rate $A_{v'}$ for the higher laying vibrational levels of the excited state. This is to be expected, the bound-free

v'	$\sum_{v''} A_{v'v''}$ (s^{-1})	$\sum_{v''} p_{v'v''}$	v'	$\sum_{v''} A_{v'v''}$ (s^{-1})	$\sum_{v''} p_{v'v''}$	v'	$\sum_{v''} A_{v'v''}$ (s^{-1})	$\sum_{v''} p_{v'v''}$
45	5.65[+6]	0.069	57	1.06[+7]	0.12	69	1.24[+7]	0.14
46	5.40[+6]	0.074	58	1.08[+7]	0.13	70	1.25[+7]	0.14
47	5.91[+6]	0.085	59	1.09[+7]	0.13	71	1.22[+7]	0.14
48	6.92[+6]	0.096	60	1.12[+7]	0.13	72	1.19[+7]	0.14
49	7.73[+6]	0.099	61	1.16[+7]	0.13	73	1.18[+7]	0.13
50	8.07[+6]	0.10	62	1.20[+7]	0.13	74	1.21[+7]	0.13
51	8.53[+6]	0.11	63	1.22[+7]	0.14	75	1.23[+7]	0.13
52	8.75[+6]	0.10	64	1.22[+7]	0.14	76	1.25[+7]	0.13
53	8.99[+6]	0.10	65	1.19[+7]	0.14	77	1.24[+7]	0.13
54	9.30[+6]	0.12	66	1.18[+7]	0.14	78	1.24[+7]	0.13
55	9.71[+6]	0.12	67	1.19[+7]	0.14	79	1.22[+7]	0.13
56	1.02[+7]	0.12	68	1.22[+7]	0.14	80	1.23[+7]	0.13

Table 3.5. *Spontaneous emission coefficients and Franck-Condon factors for the transition* $A^1\Sigma_u^+(v') \rightarrow X^1\Sigma_g^+(v'')$. *Numbers in [] indicates powers of ten.*

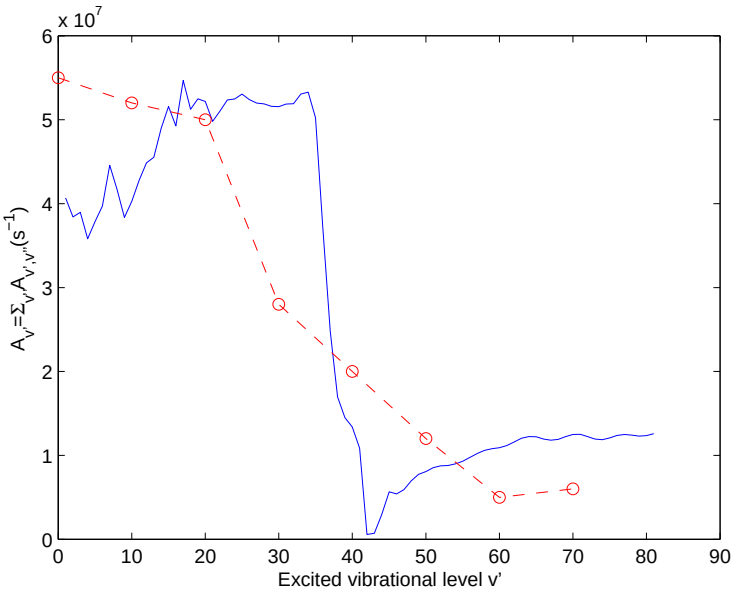

Figure 3.7. *Total bound-bound spontaneous emission decayrates* $A_{v'}$ *from excited levels* v' *into ground state* v'' *levels. The red circles are data taken from Côté and Dalgarno [43] for the same transition, included for comparison. See also the remark comment at the end of this section.*

decay generally increases with vibrational number v'. There may be some strange behavior around $v' = 45$, where the bound-bound emission seems to decrease and reach a minima. The reason for this, is unclear, but the behavior is also seen in figure 3.8. We also see that $A_{v'}$ oscillates between $4 \cdot 10^7 - 5.5 \cdot 10^7 \mathrm{s}^{-1}$ for low v', before reaching a small plateau. There is a very steep decrease in bound-bound decay between $v' = 40 - 45$. For the last vibrational levels, the decay rate $A_{v'}$ again reaches a plateau of about $10^7 \mathrm{s}^{-1}$. We would expect $A_{v'}$ to approach zero for the highest laying vibrational levels. There may therefore be even more vibrational levels in the $1^1\Sigma_u^+$ electronic state that would emerge if the potential was extended even further, beyond $R = 30\mathrm{a}_0$.

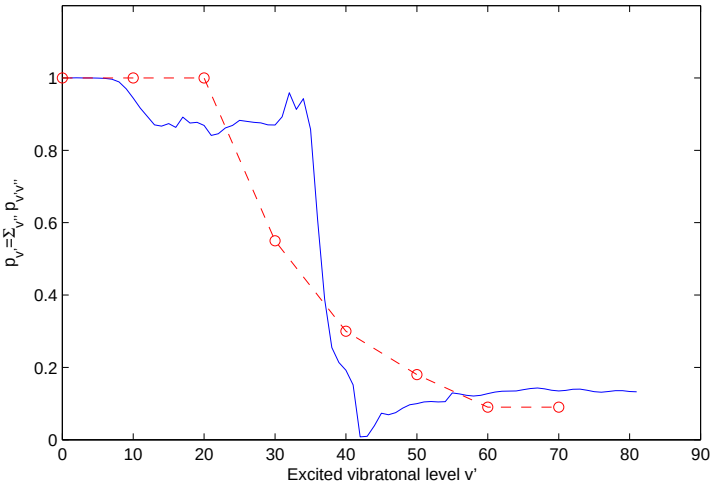

Figure 3.8. *Fraction of transitions ending up in bound vibrational levels of the ground state $p_{v'}$, as a function of excited vibrational levels v'. The red circles are data obtained by Côté and Dalgarno [43], included here for comparison.*

Figure 3.8 shows the fraction of decay that is bound-bound. This figure shows much of the same behavior as figure 3.7. From the lower vibrational levels v', almost all decay is bound-bound. However, at around $v' = 40$, there is a steep decrease in the bound-bound decay to around 10%.

Both figures 3.7 and 3.8 indicates an efficient cold molecule production, even the highest excited vibrational levels have a decay probability of $10^7 \mathrm{s}^{-1}$, this is encouraging. To see how the bound-bound decay spreads out on the ground state vibrational levels v'', we have calculated the $A_{v'v''}$ decayrates for all possible combinations of v' and v''. The results are shown in figure 3.9.

The calculations indicates that most bound-bound decay to the electronic ground state ends up with approximately the same vibrational quantum number as in the excited state ($v'' = v'$). This is seen from the diagonal form of the surface in figure 3.9. The higher excited vibrational levels v' decays dominantly to the highest vibrational levels v'' of the ground state. This is unfortunate if we were seeking to produce molecules with low vibrational quantum numbers. It is however hard to see the details in figure 3.9, so we zoom in on the highest excited vibrational levels v' and investigate their decay properties more closely, see figure 3.10.

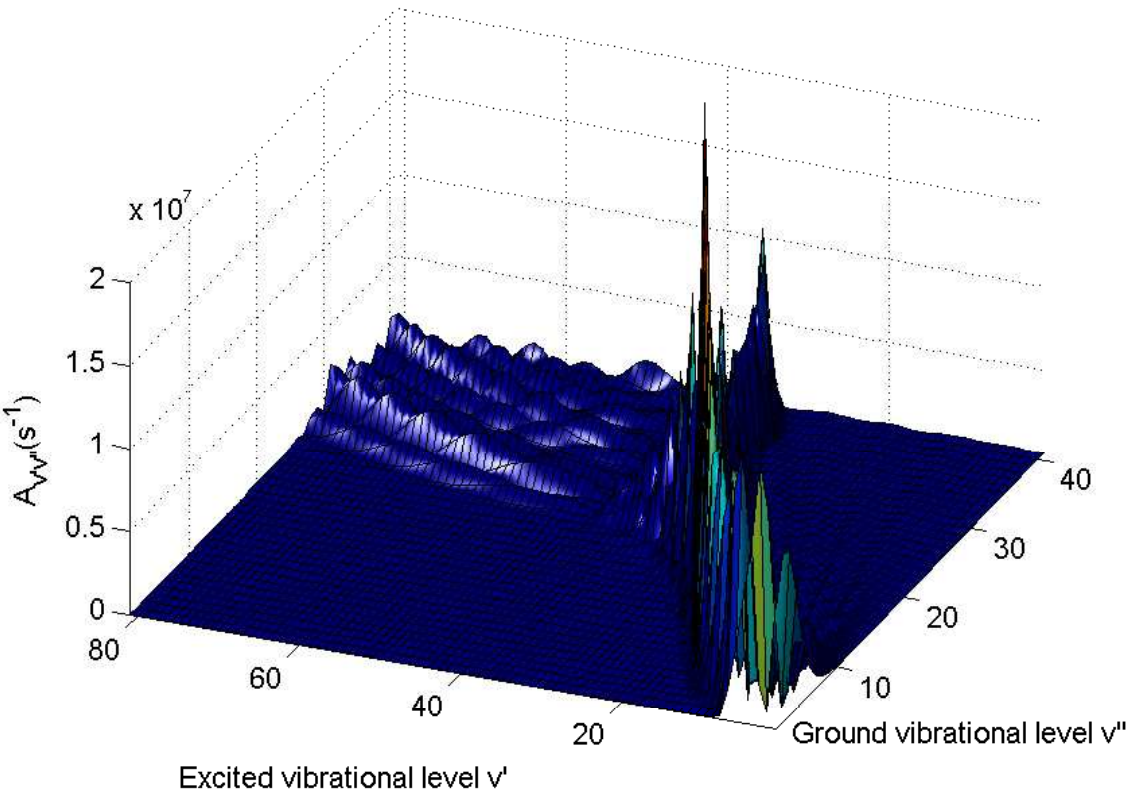

Figure 3.9. *Bound-bound decay rates for transition* $1^1\Sigma_u^+(v') \rightarrow {}^1\Sigma_g^+(v'')$*. The maximum values are found along the diagonal.*

Figure 3.10 shows several interesting features. There is a significant bound-bound emission rate from $v' \in [61, 81]$, and down to the uppermost vibrational level of the ground state. It seems, however, that all ground state vibrational levels v'' below 20 will be very sparsely populated.

We may also look for vibrational levels v' that decays dominantly to *one* vibrational level in the ground state. From figure 3.10 there seems to be few candidates with this behavior. We have however indicated one possibility with an arrow in figure 3.10. The arrow points to $A_{v'=77,v''=31} = 2.64 \cdot 10^6 \mathrm{s}^{-1}$, which implies that about 22% of all bound-bound transitions from $v' = 77$ ends up in the $v'' = 31$ vibrational level of the ground state. Excited vibrational levels that decay dominantly to one ground state vibrational level v'' can be used in a somewhat different cold molecule production scheme, namely a two-color scheme. This works by using the first laser to photoassociate two atoms to an excited state vibrational level v'. After populating a v'' vibrational level through spontaneous decay, the population is re-pumped to an excited vibrational level v' with a second laser. The excited vibrational level v' must be carefully selected. This should be a vibrational level with favorable decay rate to a preferred ground state vibrational level.

The $v' = 77$ level can be a candidate to use in such a two-color scheme. However, since

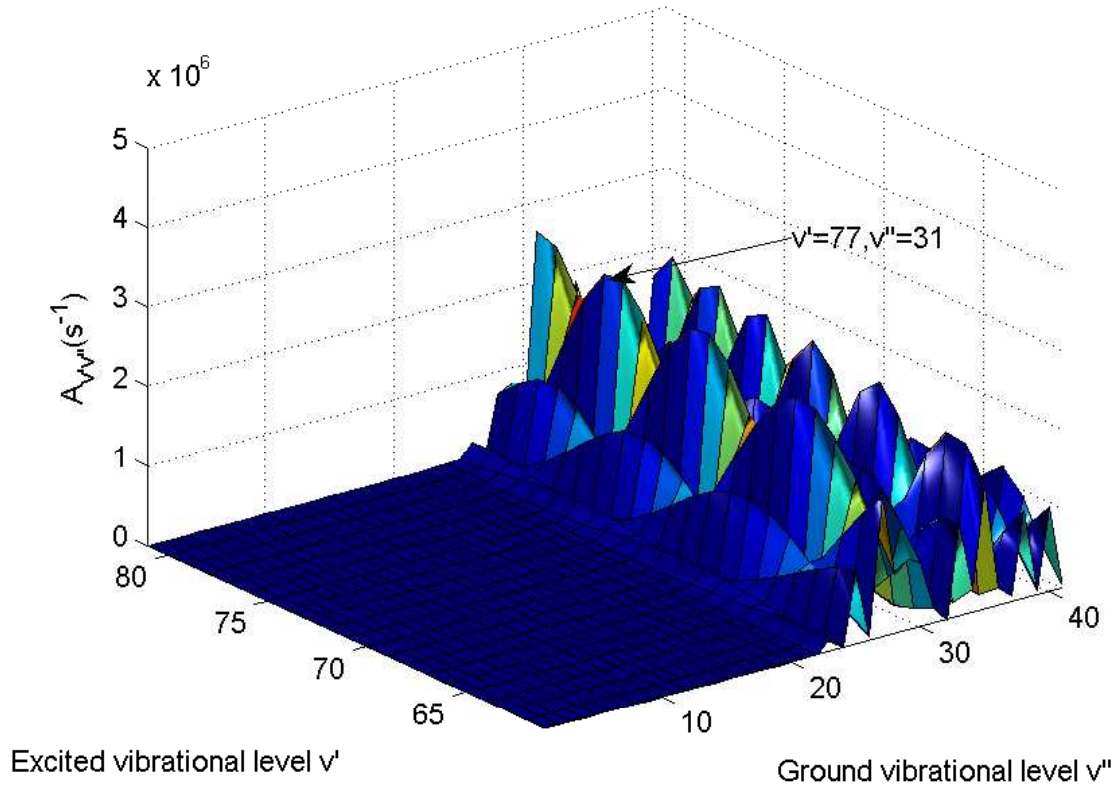

Figure 3.10. *Bound-bound decay rates for transition $v' \rightarrow v''$ with $v' \in [61, 81]$. This is an enlargement of part of figure 3.9.*

only 22% of the population decays to the lower vibrational level, the efficiency is low.

In figure 3.10 we can see that this is a general property for the $1^1\Sigma_u^+ \rightarrow X^1\Sigma_g^+$ transitions. The excited vibrational levels all decays to a series of ground state vibrational levels, and all ground state vibrational levels $v'' > 20$ seems to be relatively evenly populated.

Which rotational levels that will be populated can be found by simple considerations, the dipole selection rule for J is $\Delta J = 0, \pm 1$. The transition we are studying here is of the type $^1\Sigma \rightarrow ^1\Sigma$, and then $\Delta J = 0$ is not allowed. The initially cold atoms will have $J = 0$ (because they are cold, any other J value is very unlikely), thus the rotational level in the excited state will have to be $J = 1$. Upon decay both rotational levels $J = 0$ and $J = 2$ can be populated.

It is important to compare the data obtained with similar calculations done elsewhere. This is important in light of the uncertainties that can be expected in these kind of theoretical/numerical analysis. We have found only one paper by Côté and Dalgarno, [33], with results that allow for direct comparison. Côté and Dalgarno have performed essentially the same analysis for the same transition in $^6Li_2$. Their results are very similar to ours. There are some discrepancies. These are foremost the number of vibrational levels included in the excited electronic state $^1\Sigma_u^+$. Côté and Dalgarno have found 90 vibrational levels, while we have obtained 81 in this work. As I understand the uppermost vibrational levels they have

found are probably not of interest in cold molecule production, since they have negligible bound-bound rates. The decay spread are very similar in their work and in this work. Red circles were included in figures 3.7 and 3.8 for easier comparison between the two works. The functions plotted in these figures have the same overall behavior and the calculated values are of the same order and similar. The details are however different, typically Côté and Dalgarno predicts a more slowly decrease in the bound-bound rates and bound-bound fraction for the singlet transition.

3.2.6 Cold triplet $1^3\Sigma_u^+$ state molecules with $1^3\Sigma_g^+ \rightarrow 1^3\Sigma_u^+$ transitions

We now investigate a somewhat different transition occurring between triplet states, schematically shown in figure 3.11.

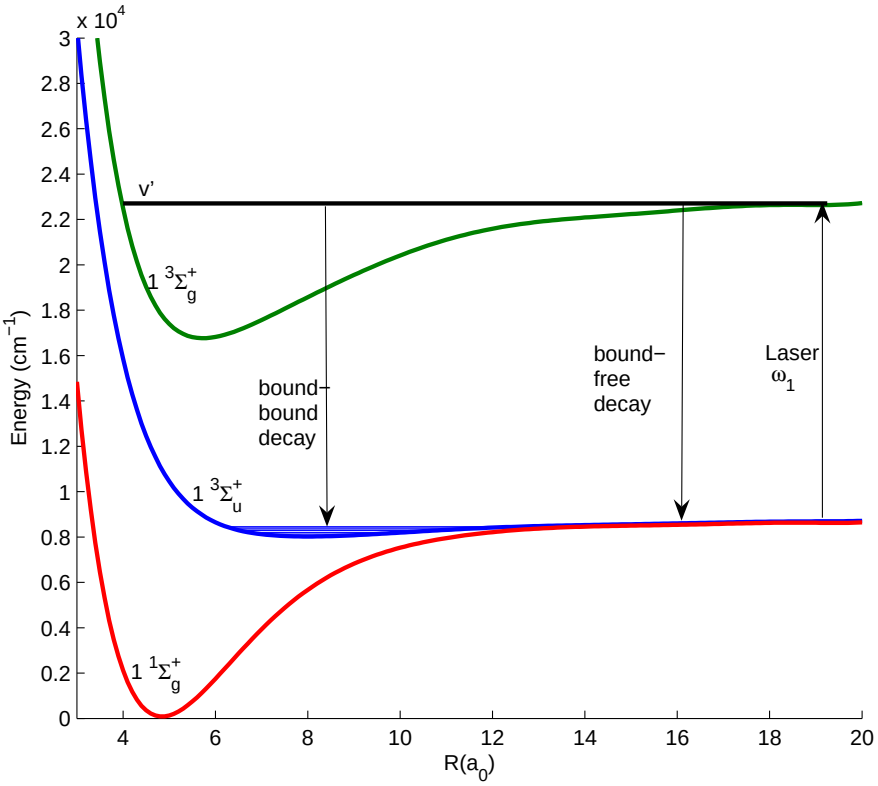

Figure 3.11. *Photoassociation scheme to produce cold triplet $1^3\Sigma_u^+$ state molecules. Molecules in the excited vibrational level v' decays to v'' in $1^3\Sigma_u^+$.*

From photoassociation of two free atoms we form molecules in one of the vibrational levels of the $1^3\Sigma_g^+$ state. By spontaneous decay we hope to produce cold triplet molecules

$$^6\mathrm{Li} + ^6\mathrm{Li} + \hbar\omega_1 \rightarrow 1^3\Sigma_g^+(v'), \tag{3.38}$$

$$1^3\Sigma_g^+(v') \rightarrow 1^3\Sigma_u^+(v'') + \hbar\omega_s. \tag{3.39}$$

v'	$\sum_{v''} A_{v'v''}$ (s^{-1})	$\sum_{v''} p_{v'v''}$	v'	$\sum_{v''} A_{v'v''}$ (s^{-1})	$\sum_{v''} p_{v'v''}$	v'	$\sum_{v''} A_{v'v''}$ (s^{-1})	$\sum_{v''} p_{v'v''}$
45	6.43[+6]	0.068	52	7.81[+6]	0.077	59	8.11[+6]	0.079
46	6.65[+6]	0.070	53	7.87[+6]	0.077	60	8.36[+6]	0.081
47	6.90[+6]	0.078	54	7.90[+6]	0.077	61	8.55[+6]	0.080
48	7.15[+6]	0.075	55	7.91[+6]	0.076	62	8.55[+6]	0.079
49	7.37[+6]	0.076	56	7.89[+6]	0.076	63	8.43[+6]	0.078
50	7.57[+6]	0.077	57	7.90[+6]	0.076	65	8.31[+6]	0.076
51	7.71[+6]	0.078	58	7.96[+6]	0.077	65	8.25[+6]	0.075

Table 3.6. *Total bound-bound spontaneous decayrates $A_{v'}$ and bound-bound fractions $p_{v'}$ for the transition $1^3\Sigma_g^+ \rightarrow 1^3\Sigma_u^+$. Numbers in [] indicates powers of ten.*

Notice that we also have the decay possibility

$$1^3\Sigma_g^+(v') \rightarrow 1^3\Pi_u(v'') + \hbar\omega_s', \tag{3.40}$$

allowed from the dipole selection rules. ω_s and ω_s' are frequencies of the photon sent out in the spontaneous decay processes, while ω_1 is the laser frequency. We argue that since $A_{v'v''}$ depends on the emitted energy in third power, transition (3.40) will be suppressed by the favorable transition (3.39). This has also been verified by explicitly calculating the decay rates for transition (3.40).

We have again calculated the total bound-bound spontaneous decay rates $A_{v'} = \sum_{v''} A_{v'v''}$ from the highest laying excited vibrational levels of $1^3\Sigma_g^+$ for transition (3.39), along with the fraction of decay that is bound-bound, $p_{v'} = \sum_{v''} p_{v'v''}$. In table 3.6 we list these results for the 21 highest laying vibrational levels, and we plot the results for *all* vibrational levels in figure 3.12.

From table 3.6 it is evident that the bound-bound decay is less than for the singlet transition. This probably has to do with the fact that the electronic states $1^3\Sigma_u^+$ and $1^3\Sigma_g^+$ have their vibrational levels horizontally shifted relative to each other. This causes less overlap between the wavefunctions and thereby decreases the bound-bound decay. Our calculations (table 3.6) indicates that it is only about 7% of the total decay that is bound-bound. Thus, the singlet transition represents a more effective mechanism for cold molecule production.

In figure 3.12 we have plotted the total decayrates $A_{v'}$ and the bound-bound fraction $p_{v'v''}$ as a function of excited vibrational levels v'. This figure only confirms what table 3.6 indicated. It is however interesting that the spontaneous decay rate has a maximum for some of the highest vibrational levels v' found, around $A_{v'=60} \simeq 8 \cdot 10^6 \mathrm{s}^{-1}$. We note that this may indicate vibrational levels well suited for cold molecule production. As with the $1^1\Sigma_u^+$ state we remark that there probably exists more vibrational levels in the $1^3\Sigma_g^+$ electronic state than what is found in this work. Côté and Dalgarno [43] seems to operate with around 90, although the last twenty are of no interest, since all decay is to the continuum from these levels.

We are by now anxious to see how the decay spread on the eight vibrational levels of the triplet $^3\Sigma_u^+$ state. Figure 3.13 provides the answers.

Figure 3.13 shows something interesting and promising. The high laying excited vibrational levels of the excited state seems to populate the lower vibrational levels of the lower

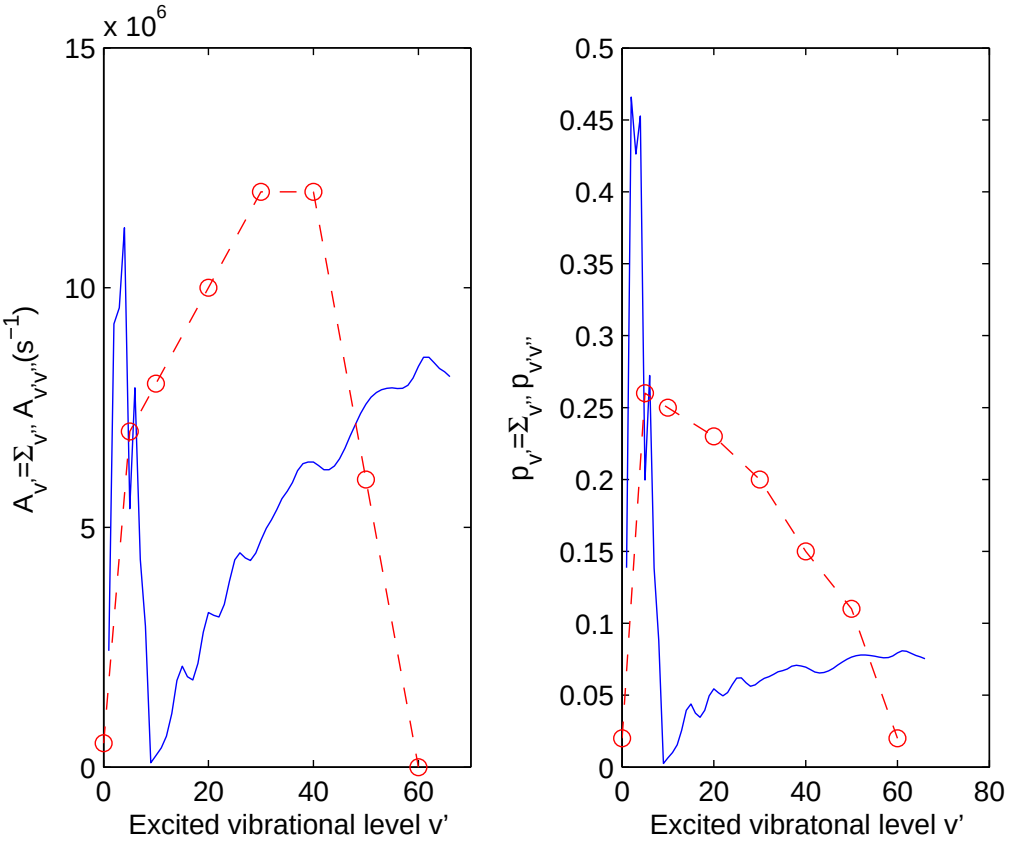

Figure 3.12. *To the left: total bound-bound decay rates $A_{v'}$ for vibrational levels v' in the $1^3\Sigma_g^+$ state that decays to $1^3\Sigma_u^+$ vibrational levels v''. To the right is the fraction of decay that is bound-bound, $p_{v'}$. Red circles are data from [43] for comparison.*

state, while the lower vibrational levels of the excited state populates the higher vibrational levels of the lower state. Moreover, the figure strongly indicates that populating excited vibrational levels around $v' = 50 - 60$ will cause decay to the lower vibrational levels in the lower triplet state.

In figure 3.13 the position of $A_{v'=51,v''=0}$ has been marked. This is done to point out our interest in the decay $v' = 51 \rightarrow v'' = 0$. The spontaneous decay rate is calculated to be $3.05 \cdot 10^6 \mathrm{s}^{-1}$, this implies that 40% of all bound decay from $v' = 51$ is to the $v'' = 0$ level of the lower state. This is encouraging, and certainly indicates that vibrationally cold molecules can be created. Combined with a bound-bound fraction of 7.8% for $v' = 51$, this way of producing cold molecules have an efficiency of about 3%, according to our calculations.

Comparing again the results with [43] we see some discrepancies in both the total bound-bound decay rates $A_{v'}$ and the bound-bound fraction, $p_{v'}$. While we find a minima in both $A_{v'}$ and $p_{v'}$ for $v' \simeq 10$, Côté and Dalgarno have no such minima, instead they have a maxima occurring for vibrational levels v' around 10-20. On this point, the results obtained are in conflict with the results in [43].

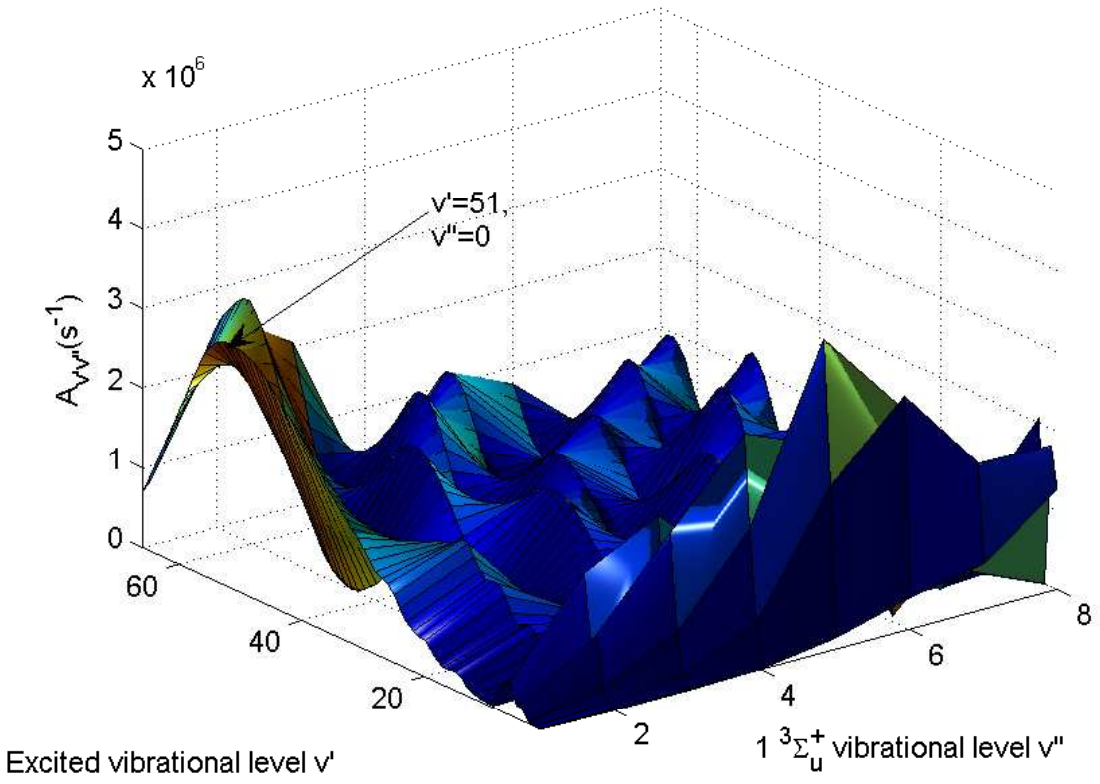

Figure 3.13. *Bound-bound decayrates $A_{v'v''}$ for all v' in the $1^3\Sigma_g^+$ state and all v'' in the $1^3\Sigma_u^+$ state.*

Chapter 4

Tunneling through the $1^1\Pi_u$ potential barrier

4.1 The problem

In the last chapter we concluded that the $1^1\Pi_u \rightarrow 1^1\Sigma_g^+$ transition, although not dipole forbidden, was unable to produce ground state molecules because of inaccessibility to the vibrational levels of the $1^1\Pi_u$ electronic state. This happens since the internuclear potential has a maximum, as seen in figure 4.1.

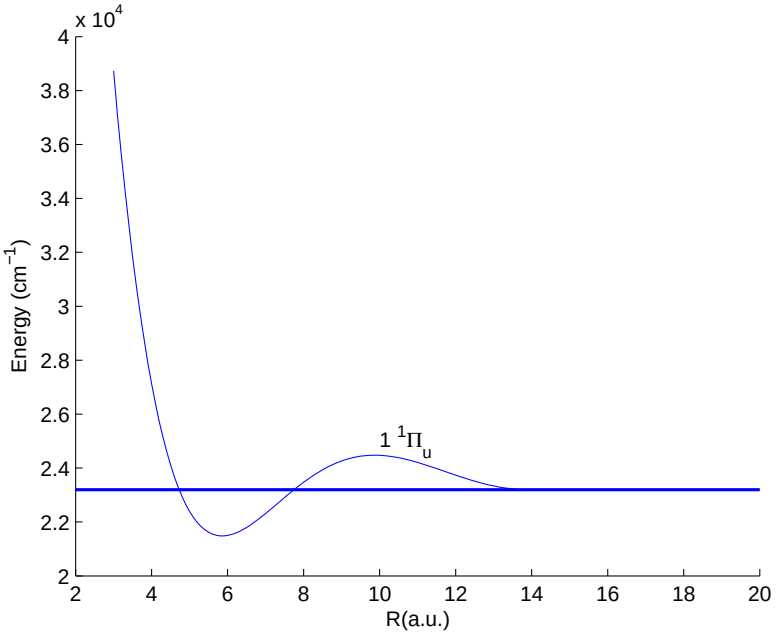

Figure 4.1. *The $1^1\Pi_u$ interatomic potential curve has a potential barrier between $R \approx 8a_0$ and $R \approx 14a_0$. The constant solid line is the asymptotic $^2S + {}^2P$ limit.*

In this chapter we consider the possibility of tunneling through the potential barrier,

gaining access to the bound vibrational levels. We expect this to be possible, with a small but finite transition probability T. The big questions are : 1) what order of magnitude will we find for T, and 2) if a molecule manages to tunnel the barrier, what is the probability for decay to the ground state versus the probability for tunneling back out to the continuum states? This is of course highly dependent upon the transmission probability. To calculate the transmission probability we need to review some theory.

4.2 Tunneling theory

In this section we review the theory for quantum mechanical tunneling. Tunneling is a purely quantum mechanical effect, making it possible for a particle to go *through* a wall, if it can not pass over. This happens when the particle has an energy less than the hight of the potential barrier.

Tunneling is a well known phenomena in physics, and most quantum mechanical textbooks presents tunneling exemplified for a particle that encounters a box potential. For such a potential it is possible to calculate the transmission probability analytically.

At all there have been five Nobel prizes related to the discoveries of different tunneling phenomena. In a patriotic mood we should mention the 1973 Nobel prize awarded Ivar Giaever[1]. He was awarded the prize for his experimental discovery of tunneling in semiconductors and superconducters.

Here we aim a little lower and present theory for calculating the transmission probability through a potential of arbitrary shape. This section assumes knowledge of the standard calculations of the tunneling probability for a box-potential[2]. We use essentially the same theory to calculate the transmission coefficient for a potential of arbitrary shape.

The calculation method that we present here, divides the potential (of arbitrary shape) into box potentials of width d, see figure 4.2. We define $x = L$ to be the position where the particle encounter the barrier. The height of each box V_j with $j \in \{0, 1, \ldots, n\}$ is taken as the average between the actual potential at $V(L + dj)$ and $V(L + (j - 1)d)$,

$$V_j \equiv \frac{V(L + dj) + V(L + (j - 1)d)}{2}. \tag{4.1}$$

We will also need

$$k \equiv \sqrt{\frac{2mE}{\hbar^2}}, \tag{4.2}$$

$$\alpha_j \equiv \sqrt{\frac{2m(V_j - E)}{\hbar^2}}. \tag{4.3}$$

In analogy with the usual treatment of the box-potential we define three regions, I, II and III. The potentials in both region I and region III are assumed to be 0. We assume I to be the region before the particle encounters the barrier, II to be the region within the potential barrier and III to be the region after the particle has passed the barrier. We will need to solve the Schrödinger equation in all three regions. If we assume the particle to have an energy E,

[1] Together with Leo Esaki and Brian D Josephson.

[2] See for instance P. C. Hemmer, *Kvantemekanikk* pages 58-62.

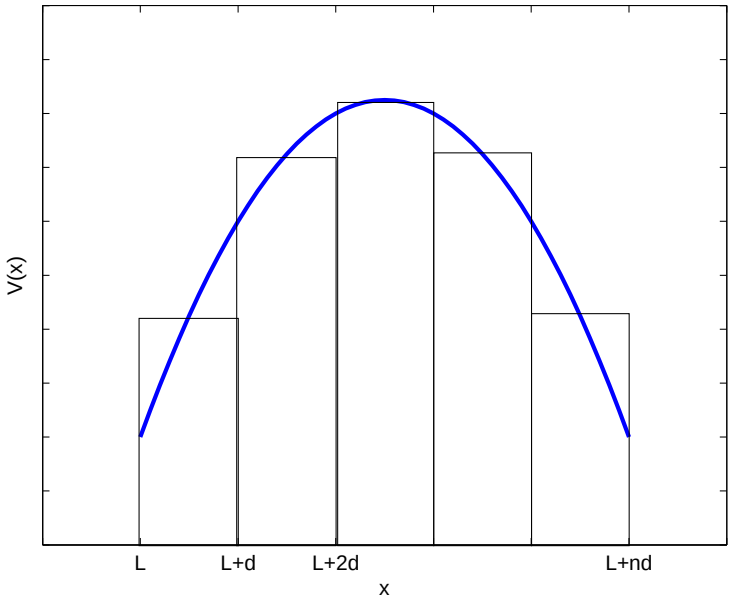

Figure 4.2. *A potential of arbitrary shape (blue curve) is approximated with boxes of width d.*

the Schrödinger equation has solutions

$$\psi_I(x) = Ae^{ikx} + Be^{-ikx}, \tag{4.4}$$
$$\psi_j(x) = C_j e^{\alpha_j x} + D_j e^{-\alpha_j x}, \tag{4.5}$$
$$\psi_{III}(x) = Fe^{ikx} + Ge^{-ikx}. \tag{4.6}$$

ψ_I is the solution in region I and ψ_{III} is the solution in region III. In region II we write the solution as ψ_j, here the II index has been suppressed for easier notation. Instead we label the wavefunctions (ψ_j) in this area with a j to know which box segment they belong to ($j = 0, 1, \ldots, n$).

Notice from the definition (4.3) that α_j may be complex if $E > V_j$. This could easily happen for a general potential in some regions, and we do not assume α_j to be real.

We require the wavefunction and its first derivative to be continuous functions. At $x = L$ we must therefore demand

$$Ae^{ikL} + Be^{-ikL} = C_1 e^{\alpha_1 L} + D_1 e^{-\alpha_1 L}, \tag{4.7}$$
$$Aike^{ikL} - ikBe^{-ikL} = C_1\alpha_1 e^{\alpha_1 L} - \alpha_1 D_1 e^{-\alpha_1 L}. \tag{4.8}$$

Now introduce the 2×2 matrix K

$$K(\alpha_j, x) \equiv \begin{pmatrix} e^{\alpha_j x} & e^{-\alpha_j x} \\ \alpha_j e^{\alpha_j x} & -\alpha_j e^{-\alpha_j x} \end{pmatrix}. \tag{4.9}$$

With this matrix we can rewrite equations (4.7) and (4.8) in matrix form

$$K(L, ik)\begin{pmatrix} A \\ B \end{pmatrix} = K(L, \alpha_1)\begin{pmatrix} C_1 \\ D_1 \end{pmatrix}. \tag{4.10}$$

A similar continuity condition must be met at all the other boundaries (between segments)

$$K(L+jd,\alpha_j)\begin{pmatrix}C_j\\D_j\end{pmatrix}=K(L+jd,\alpha_{j+1})\begin{pmatrix}C_{j+1}\\D_{j+1}\end{pmatrix}, \tag{4.11}$$

with $j=1,2,\ldots,n-1$. At the last boundary however, we need to be a bit careful

$$K(L+nd,\alpha_n)\begin{pmatrix}C_n\\D_n\end{pmatrix}=K(L+nd,ik)\begin{pmatrix}F\\G\end{pmatrix}. \tag{4.12}$$

We want to express A and B in terms of F and G. Using the three equations (4.10)-(4.12) we can do this

$$\begin{pmatrix}A\\B\end{pmatrix}=K^{-1}(L,ik)K(L,\alpha_1)K^{-1}(L+d,\alpha_1)K(L+d,\alpha_2)\cdots K^{-1}(L+nd,\alpha_n)K(L+nd,ik)\begin{pmatrix}F\\G\end{pmatrix}. \tag{4.13}$$

Let us now consider multiplication of two of the matrices in equation (4.13), and define $M\equiv K(L+jd,\alpha_j)K^{-1}(L+(j+1)d,\alpha_j)$

$$M(\alpha_j)=\frac{1}{2\alpha}\begin{pmatrix}e^{\alpha_j(L+jd)} & e^{-\alpha_j(L+jd)}\\ \alpha_j e^{\alpha_j(L+jd)} & -\alpha_j e^{-\alpha_j(L+jd)}\end{pmatrix}\begin{pmatrix}\alpha_j e^{-\alpha_j(L+(j+1)d)} & e^{-\alpha_j(L+(j+1)d)}\\ \alpha_j e^{\alpha_j(L+(j+1)d)} & -e^{\alpha_j(L+(j+1)d)}\end{pmatrix}. \tag{4.14}$$

For the M matrix in equation (4.14) we find

$$M(\alpha_j)\equiv\begin{pmatrix}\cosh(\alpha_j d) & -\frac{1}{\alpha_j}\sinh(\alpha_j d)\\ -\alpha_j\sinh(\alpha_j d) & \cosh(\alpha_j d)\end{pmatrix}. \tag{4.15}$$

We must also consider what happens if α is complex in one or more of the segments. If α is complex it will be purely imaginary, $\alpha=i\beta$. In this case we find

$$M(i\beta)=\begin{pmatrix}\cos(\beta d) & -\frac{1}{\beta}\sin(\beta d)\\ \beta\sin(\beta d) & \cos(\beta d)\end{pmatrix}, \tag{4.16}$$

since we have the relations $\cosh(ix)=\cos(x)$ and $\sinh(ix)=i\sin(x)$. Now, use equation (4.15) in equation (4.13) to obtain

$$\begin{pmatrix}A\\B\end{pmatrix}=K^{-1}(L,ik)M(\alpha_1)M(\alpha_2)\cdots M(\alpha_n)K(L+nd,ik)\begin{pmatrix}F\\G\end{pmatrix} \tag{4.17}$$

To simplify the notation further we may use a product matrix P to represent the product of the $M(\alpha_j)$ matrices. P is a 2×2 matrix defined by

$$P\equiv\Pi_{j=1}^{n}M_j(\alpha_j)=\begin{pmatrix}\alpha & \beta\\ \gamma & \delta\end{pmatrix}. \tag{4.18}$$

In terms of α,β,γ and δ we find

$$\begin{pmatrix}A\\B\end{pmatrix}=\frac{1}{2ik}\begin{pmatrix}e^{iknd}(ik\alpha+\gamma-k^2\beta+ik\delta) & e^{-ik(2L+nd)}(ik\alpha+\gamma+k^2\beta-ik\delta)\\ e^{ik(2L+nd)}(ik\alpha-\gamma-k^2\beta-ik\delta) & e^{-iknd}(ik\alpha-\gamma+k^2\beta+ik\delta)\end{pmatrix}\begin{pmatrix}F\\G\end{pmatrix}. \tag{4.19}$$

The transmission coefficient (probability for tunneling) can be expressed

$$T \equiv \frac{j_t}{j_i}, \tag{4.20}$$

with j_t as the transmitted current and j_i as the incoming current. The current is defined as

$$j \equiv \frac{\hbar}{2mi}(\Psi^* \nabla \Psi - \Psi \nabla \Psi^*). \tag{4.21}$$

For plane waves this yields for the transmission coefficient

$$T = \left|\frac{F}{A}\right|^2 = \frac{4}{(\alpha+\delta)^2 + (\beta k - \gamma/k)^2}, \tag{4.22}$$

if we assume the incoming and outgoing waves to have the same wave coefficient k. In equation (4.22) we have used $G = 0$, since there are no reflected waves in region III.

4.3 Numerical implementation

In order to calculate the transmission coefficient T for an arbitrary shaped potential, the procedure outlined above should be ideal for making a computer code. A small computer program based on this theory has therefore been written.

As input the program takes the potential shape, the particle mass, energy of the incoming particle, and the number of boxes to divide the barrier into. The program interpolates the potential, divides it into boxes with the desired width, calculates the K and M matrices needed, multiplies them and computes the transmission probability. The whole program is listed in appendix B.

The programming language used is MATLAB, this is chosen because it saves a lot of time, not needing to write routines to interpolate and multiply matrices. The program is not expected to be exceptional when it comes to running time and accuracy[3]. The repeated evaluations of trigonometric functions will lengthen the computing time and may cause problems with the accuracy in extreme cases. The convergence may also be slow and it should be expected that we need a high number of boxes to get a high level of accuracy.

4.4 Results with the model

From here on, regions I, II and III are defined according to figure 4.3, and with potential we mean the $1^1\Pi_u$ potential barrier we are attempting to tunnel.

Our previous calculations indicated a vibrational level (the blue level in table 3.4) with nearly the same energy as the asymptotic $^2S + {}^2P$ continuum. By tunneling through the potential, this is the vibrational level we would expect to populate. From our calculations we find the vibrational level in question to be situated approximately $0.4\mathrm{cm}^{-1}$ above the continuum limit. To access this vibrational level, a kinetic energy corresponding to a temperature $0.57\mathrm{K}$ would be needed, estimated from $k_B T \sim E$. It may be to our disadvantage

[3]This is not due to the quality of MATLAB, in fact tests have shown that MATLAB in its newest version is just as fast as C++.

that this vibrational level is so close in energy to the continuum limit, since this will reduce the energy with witch we can approach the barrier. The next vibrational level is too high in energy to be reached at low temperatures.

We now try to calculate the transmission probability with a model including the potential to the left in figure 4.3.

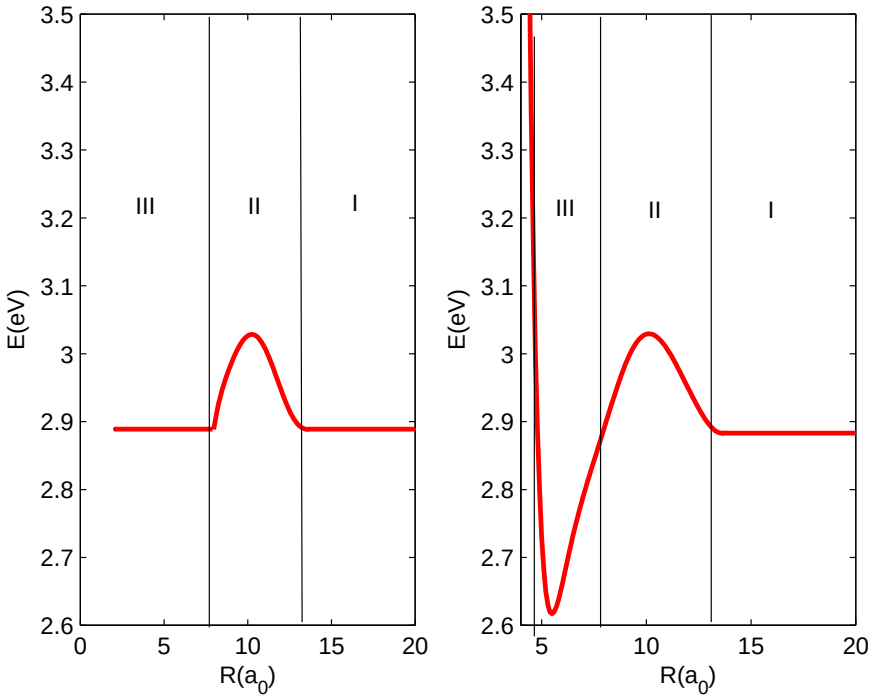

Figure 4.3. *Our first model includes only the potential to the left. We have extended this first model by including the correct potential in region III, this corresponds to the potential curve shown to the right.*

The Schrödinger equations in the three regions are (with $V(R)$ as the appropriate potential)

$$\left\{-\frac{\hbar^2}{2\mu}\frac{\mathrm{d}^2}{\mathrm{d}R^2}+V(R)+\frac{\hbar^2 J(J+1)}{2\mu R^2}\right\}\psi(R)=E\psi(R). \tag{4.23}$$

The approximated Schrödinger equations we solve with our program (in the different regions) are

$$\left\{-\frac{\hbar^2}{2\mu}\frac{d^2}{dR^2}+V_i(R)\right\}\psi_i(R)=E\psi_i(R), \tag{4.24}$$

with $i\in\{I,II,III\}$ and $V_I=V_{III}=$ constant while $V_{II}=V_{II}(R)\simeq V(R)$ for R in region II.

$V_I=$ constant is a good approximation. However, $V_{III}=$ constant is not a good approximation at all, since $V(R)$ really has a quite complex dependency upon R in this region.

These shortcomings will be returned to later, but we calculate the tunneling probability also within this first model. This should give us a hint of the overall tunneling probability. Since the kinetic energy is determined mainly by temperature $k_B T \simeq E$, the tunneling probability will depend on temperature. Figure 4.4 shows transmission coefficient as a function of relevant temperatures, along with the transmission coefficient in the high temperature limit, corresponding to $0.1 - 0.5\mathrm{eV}$.

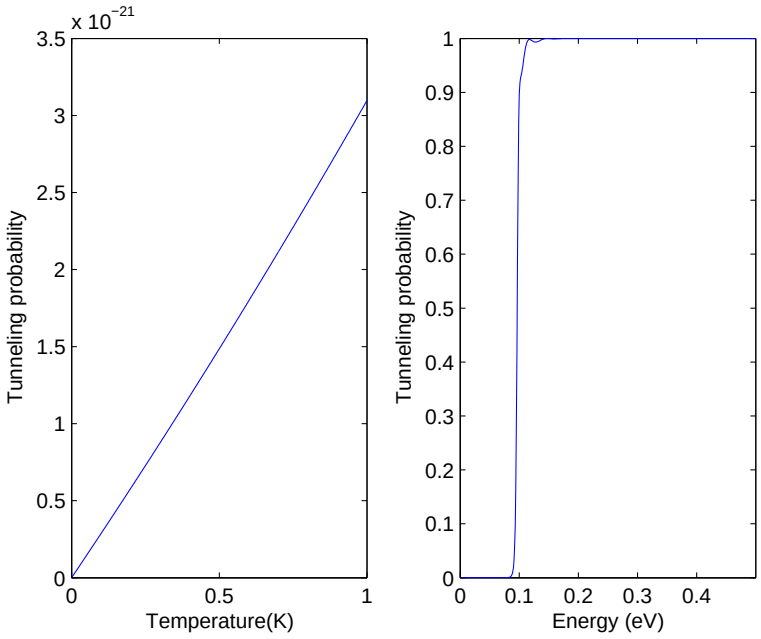

Figure 4.4. *To the left we see the tunneling coefficient for* $m\mathrm{K}$ *temperatures, and to the right the high temperature limit has been included, corresponding to temperatures well above* $1\mathrm{K}$*. The potential barrier is approximately* $0.13\mathrm{eV}$ *high.*

Our calculations indicate a transmission coefficient of about 10^{-20} for temperatures in the range of 0.1 K. To lower the temperature further, and thereby the energy, will significantly decrease the probability for tunneling. What we have found signals that tunneling is a very unlikely phenomena, which seriously limits the possibility of producing cold molecules with this mechanism. The probability is far too low to lead to a significant concentration of molecules.

Struck down by the low probability, we have tried to extend the model further. One could hope that effects not taken into consideration, perhaps the correct $V(R)$ in region III, and maybe rotation, could improve the probability. This is probably unrealistic, since it is first and foremost the length and height of the barrier that seriously limits our chance of tunneling.

We have however extended the model to include the realistic potential in region III, and we have also included the angular momentum term in equation (4.23). These effects were included by the same philosophy as before, by dividing the potential into pieces in each region, and using the theory outlined previously to calculate the tunneling probability. The angular momentum term was included by adding this as a barrier "on top" of the potential

$V(R)$.

We report our final tunneling probabilities in table 4.1 and in figure 4.5. Figure 4.5 shows the tunneling probability as a function of energy for different J quantum numbers. We have also included all the vibrational levels of the $1^1\Pi_u$ state that are situated above the continuum limit.

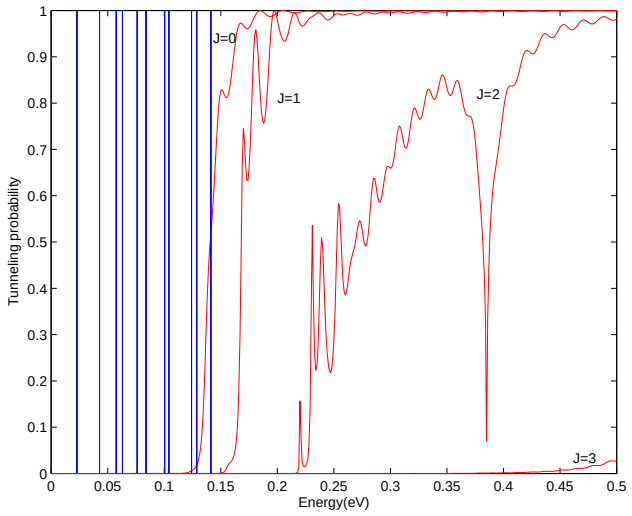

Figure 4.5. *Tunneling probability versus energy for $J = 0, 1, 2, 3$. The vertical blue lines indicates vibrational levels. The energies are measured above the continuum limit. The somewhat odd spacing for the vibrational levels is not a bug, this is the vibrational energy levels as found when solving the Schrödinger equation with Numerovs method. The lowest (most interesting) vibrational level can not be seen in this figure, since it overlaps with the y-axis.*

The higher vibrational levels, although shown in figure 4.5, are not relevant to cold molecule production, since they require too high temperatures to be populated (room temperatures). Therefore we have included only one vibrational level in table 4.1, namely the vibrational level corresponding very closely to the continuum limit. The tunneling probability for this level is calculated for different J values, and the results are tabulated in table 4.1.

	Prob. with $n = 545$	Prob. with $n = 4904$	Prob. with $n = 27244$	Prob. with $n = 49038$
$J = 0$	$6.69 \cdot 10^{-21}$	$5.1683 \cdot 10^{-21}$	$4.709 \cdot 10^{-21}$	$4.6591 \cdot 10^{-21}$
$J = 1$	$2.565 \cdot 10^{-32}$	$2.570 \cdot 10^{-32}$	$2.574 \cdot 10^{-32}$	$2.575 \cdot 10^{-32}$
$J = 2$	$1.922 \cdot 10^{-60}$	$2.051 \cdot 10^{-60}$	$2.075 \cdot 10^{-60}$	$2.078 \cdot 10^{-60}$
$J = 3$	$5.852 \cdot 10^{-111}$	$6.469 \cdot 10^{-111}$	$6.481 \cdot 10^{-119}$	$7.080 \cdot 10^{-119}$

Table 4.1. *Tunneling probabilities from the vibrational level with energy $4.59 \cdot 10^{-5}$eV above the continuum limit. We include values for different number of partitions n, to check convergence.*

From both table 4.1 and figure 4.5 one might be surprised of the large differences between $J = 3$, $J = 2$, $J = 1$, and $J = 0$, but in fact this might be reasonable since at low energies

(temperatures) such an angular momentum term represent a barrier to the "on top" of the potential barrier $V(R)$.

More as a curiosity we have investigate which vibrational levels in the ground state that we could expect to populate with molecules that has tunneled through the potential barrier. Figure 4.6 shows the spontaneous decay rates $A_{v'v''}$ with v' as the relevant vibrational level of the $1^1\Pi_u$ state.

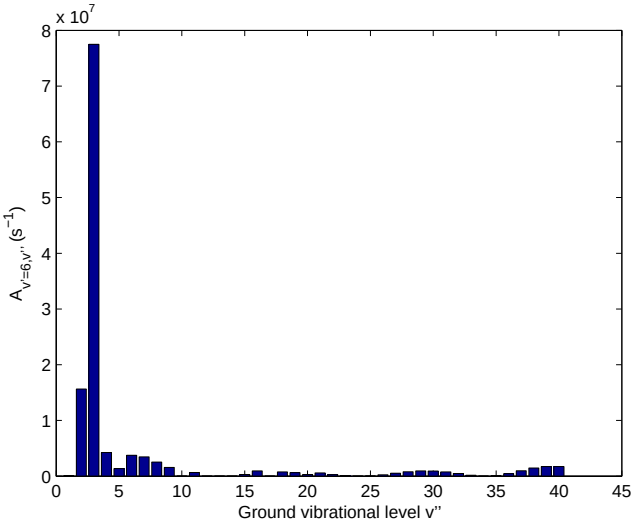

Figure 4.6. *Decay rates $A_{v'v''}$ for $1^1\Pi_u(v'=6) \rightarrow 1^1\Sigma_g^+(v'')$*

It is exciting to see that the ground state vibrational level $v''=3$ seems to be heavily populated. This is probably because the $1^1\Pi_u$ state and the ground state has much the same equilibrium distances. In fact, 61% of all bound-bound decay from the excited vibrational level we have considered is to the $v''=3$ level of the ground state. Comparing with the other transitions investigated in previous chapters, this actually proves to be the one most suited for populating the lower vibrational ground state levels.

4.5 Conclusions

This tunneling idea turned out *not* to be a good way to produce cold molecules in Li_2. We are seriously limited by the extremely low tunneling probability, making it practically impossible to populate relevant $1^1\Pi_u$ vibrational levels. This will probably not be possible in other molecules either, since most molecules are heavier than the Li_2 molecule, making tunneling even more unlikely.

However, we shall not forget that the $1^1\Pi_u \rightarrow X^1\Sigma_g$ transition is very interesting. Although access to the vibrational levels can not be accomplished with tunneling, it may be possible to use a two-color scheme to access them. Such a scheme would probably need to involve excitations to electronic states corresponding to the 2^S+3^S or the 2^P+2^P asymptotic limits. Based on the potential curves calculated by Konowalow and Fish [40], the electronic state $3^1\Sigma_g^+$ may seem like an ideal candidate. To determine this we would need to do cal-

culations with this state and look at the decay to $1^1\Pi_u$. Since we have not studied the $3^1\Sigma_g^+$ electronic state, such considerations are beyond the scope of this thesis.

Chapter 5

Cold atomic collisions

THis chapter is concerned with cold and (mostly-) elastic collisions, a large and rather complicated field (at least in my mind) that by no means can be tamed in this limited treatment. The main focus will be on calculating the phase shift, a very central quantity in scattering theory. This is because both the scattering length and the cross section can be calculated from the phase shift, as we will see.

The first part of this chapter is a quite detailed treatment of the partial waves method. This method was in fact originally developed by the Norwegian physicist Johan Peter Holtsmark together with Hilding Faxén in 1927 (Faxén was a Swedish physicist). The second part is concerned with the use of this theory, attempting to calculate scattering lengths for two colliding Li atoms, guided by the interatomic potential $V(R)$ obtained in chapter 3.

This chapter is meant as an introduction, it is simply an amateurs first attempt to do scattering theory and the results obtained must be seen on this background. My calculated scattering lengths can not be taken as highly accurate final answers.

5.1 Basic definitions

Before being able to discuss scattering and collisions, a couple of definitions are needed. One distinguishes between *elastic* and *inelastic* scattering. An *elastic* scattering process is one where the particles involved do *not* change their internal quantum state. In an *inelastic* scattering process, one or more of the particles involved change their internal quantum state. The photoassociation process described in chapter 3 is an example of an inelastic process since one of the atoms is excited from a s to a p state

Channels are used in scattering theory. A channel is a possible mode of fragmentation of the composite system during the collision. This implies that in elastic scattering the initial (before scattering) channel and final (after scattering) channel are the same. Channels are further divided into *open channels* and *closed channels*. A *closed channel* is forbidden by conservation laws, while *open channels* are allowed by conservation laws.

5.2 Cross sections

Definition of cross section:
The cross section for a certain type of event in a given collision is the ratio of the number of

events of the right type per unit time and per unit scatterer, to the flux of incident particles with respect to the target.

We might exemplify this definition by thinking of two particles A and B colliding and forming particle C. The cross section will, according to the definition be given as

$$\sigma = \frac{n_C}{N_A n_B}, \tag{5.1}$$

with n_C as the number of C particles produced, N_A as the flux of incoming A particles and n_B as the number of B particles acting as targets for the incoming A particles.

Definition of differential cross section:
We define the differential cross sections $\frac{\mathrm{d}\sigma}{\mathrm{d}\Omega}$ as the ratio of the outgoing flux of particles passing through the area $R^2\mathrm{d}\Omega$ per unit solid angle, to the incident flux.

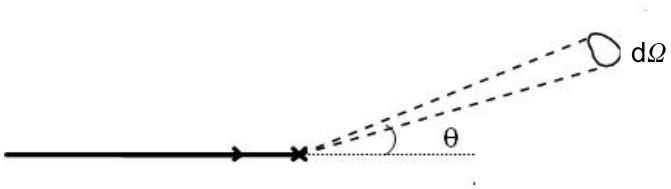

Figure 5.1. *Simple drawing illustrating the differential cross section. The cross represents the scatterer and incident particles are from the left, in the direction of the arrow.*

5.3 Scattering between two spinless particles

Scattering between two spinless particles are among the simplest cases to study. A good starting point is the time-dependent Schrödinger equation

$$i\hbar\frac{\partial}{\partial t}\Psi(\mathbf{R},t) = \left\{-\frac{\hbar^2}{2\mu}\nabla^2 + V(\mathbf{R})\right\}\Psi(\mathbf{R},t), \tag{5.2}$$

with μ as the reduced mass and $V(\mathbf{R})$ describing the interaction between the two particles. Since $V(\mathbf{R})$ is time-independent, we seek solutions of the time-independent Schrödinger equation

$$\left\{-\frac{\hbar^2}{2\mu}\nabla^2 + V(\mathbf{R})\right\}\psi(\mathbf{R}) = E\psi(\mathbf{R}). \tag{5.3}$$

For large distances, $R \to \infty$, we assume $V = 0$. The corresponding Scrödinger equation is easy to solve, and we find

$$\psi_{\text{in}}(\mathbf{R}) = Ae^{ikz}, \tag{5.4}$$

if we assume the particles to travel parallel to the z-axis. A is a normalization constant. This solution is certainly the right one for the incoming particles, but the scattered particles have more complicated wavefunctions. It is standard to argue that far from the scatterer, after the scattering has taken place, the scattered wave is outgoing spherical of the form

$$\psi_{\text{out}}(\mathbf{R}) = Af(k,\theta,\phi)\frac{e^{ikR}}{R}. \tag{5.5}$$

$f(k,\theta,\phi)$ is called the *scattering amplitude*. When $R \to \infty$ we find $\nabla^2\psi_{\text{out}}$ to be

$$\nabla^2\psi_{\text{out}}(\mathbf{R}) = -k^2\psi_{\text{out}}(\mathbf{R}), \tag{5.6}$$

thus $\psi_{\text{out}}(\mathbf{R})$ satisfies the Schrödinger equation when $R \to \infty$. This enables us to write down the general asymptotic solution to equation (5.3) as

$$\psi(\mathbf{R}) = \psi_{\text{in}}(\mathbf{R}) + \psi_{\text{out}}(\mathbf{R}), \tag{5.7}$$

$$= A\left[e^{ikz} + f(\theta,\phi)\frac{e^{ikR}}{R}\right], \qquad R \to \infty. \tag{5.8}$$

To find the differential cross section we use the probability current (defined in chapter 4) to find the (outgoing) radial current

$$\mathbf{j}\cdot\mathbf{R} = \frac{\hbar}{2mi}\left(\psi^*_{\text{out}}\frac{\partial\psi_{\text{out}}}{\partial R} - \frac{\partial\psi^*_{\text{out}}}{\partial R}\psi_{\text{out}}\right) = |Af(k,\theta,\phi)|^2\frac{\hbar}{2mi}\frac{2Rik}{R^3} = |Af(k,\theta,\phi)|^2\frac{v}{R^2}, \tag{5.9}$$

where $v = \frac{\hbar k}{m}$ has been introduced as the particle speed. The differential cross section is given by multiplying the outgoing particle flux with $R^2\mathrm{d}\Omega$ and divide with the incoming flux $|A|^2v$ according to the definition. This gives

$$\frac{\mathrm{d}\sigma}{\mathrm{d}\Omega} = |f(k,\theta,\phi)|^2. \tag{5.10}$$

5.4 The partial waves method

In the preceding section we found the differential cross section given by the scattering amplitude $|f(k,\theta,\phi)|^2$. The partial waves method will help us find $f(k,\theta,\phi)$. This method is very well suited at low energies, with only a small number of partial waves that contribute.

Assume a Hamiltonian of the form

$$\hat{H} = -\frac{\hbar^2}{2\mu}\nabla^2 + V(R), \tag{5.11}$$

describing a particle with mass μ in a spherical symmetric potential $V(R)$ (two particles colliding in the center of mass system). For such a Hamiltonian we always have $[\hat{H},\hat{\mathbf{L}}^2] = [\hat{H},\hat{L}_z] = [\hat{\mathbf{L}}^2,\hat{L}_z] = 0$. Since $\mathbf{k}$ is along the incident direction that coincides with the z-axis, the solutions can not depend on ϕ. This enables us to expand $\psi_{\mathbf{k}}$ in a series of the Legendre polynomials $\mathcal{L}_l$[1]. In fact any function $f(\theta)$ obeying the Dirichlet [2] conditions can

[1] Defined by

$$\mathcal{L}_l(x) = \frac{1}{2^l l!}\frac{\mathrm{d}^l}{\mathrm{d}x^l}(x^2-1)^l$$

.

[2] See chapter 12 in [57].

be represented as an infinite sum of Legendre polynomials

$$f(\theta) = \sum_{l=0}^{\infty} f_l \mathcal{L}_l(\cos\theta). \tag{5.12}$$

For $\psi_{\mathbf{k}}(R,\theta)$ we write

$$\psi_{\mathbf{k}}(R,\theta) = \sum_{l=0}^{\infty} P_l(k,R)\mathcal{L}_l(\cos\theta), \tag{5.13}$$

with $RP_l(k,R) = u_l(k,R)$ satisfying

$$\left\{ \frac{\mathrm{d}^2}{\mathrm{d}R^2} - \frac{l(l+1)}{R^2} - \frac{2\mu V(R)}{\hbar^2} + k^2 \right\} u_l(k,R) = 0. \tag{5.14}$$

We investigate the behavior of $u_l(k,R)$ for large and small R. To investigate small R behavior we expand $u_l(k,R)$ in a Fröbenius series, and find the roots of the indicial equation.

$$u_l(k,R) = \sum_{n=0}^{\infty} a_n R^{n+s}, \quad u_l'(k,R) = \sum_{n=0}^{\infty} a_n(n+s)R^{n+s-1}, \quad u_l''(k,R) = \sum_{n=0}^{\infty} a_n(n+s)(n+s-1)R^{n+s-2}. \tag{5.15}$$

Assuming $V(R)$ is less singluar than R^{-2} one finds the indicial equation with solutions

$$s(s-1) - l(l+1) = 0, \qquad \Rightarrow \qquad s \in \{l+1, -l\}. \tag{5.16}$$

Since the $s = -l$ solution will diverge at $R = 0$, this solution must be discarded. We are left with $u_l(k,R) \sim R^{l+1}$ at the origin.

For $R > a$ we will assume $V(R) = 0$, the potential is zero for a finite R value a. In this case equation (5.14) simplifies to

$$\left\{ \frac{\mathrm{d}^2}{\mathrm{d}\rho^2} + \frac{2}{\rho}\frac{\mathrm{d}}{\mathrm{d}\rho} - \frac{l(l+1)}{\rho^2} - 1 \right\} P_l(\rho) = 0, \qquad R > a \qquad , \tag{5.17}$$

with $\rho = kR$. The general solution to this equation is a linear combination of the spherical Bessel function $j_l(\rho)$ and the spherical Neumann function $n_l(\rho)$. The solution can therefore be written

$$P_l(k,R) = B_l(k) j_l(kR) + C_l(k) n_l(kR), \qquad R > a. \tag{5.18}$$

The spherical Bessel ($j_l(kR)$)- and Neumann ($n_l(kR)$) functions are defined as

$$j_l(x) = \sqrt{\frac{\pi}{2x}} J_{l+\frac{1}{2}}(x), \qquad n_l(x) = (-1)^{l+1}\sqrt{\frac{\pi}{2x}} J_{-l-\frac{1}{2}}(x), \tag{5.19}$$

with $J_v(x)$ being a Bessel function of order v. See [57], chapter 16 for a further discussion of Bessel functions.

When $R \to \infty$ it may be shown that $j_l(x) \to \frac{1}{x}\sin(x - \frac{l\pi}{2})$ and $n_l(x) \to -\frac{1}{x}\cos(x - \frac{l\pi}{2})$. Therefore we may write

$$P_l(k,R) = B_l(k)\frac{\sin(kR - l\pi/2)}{kR} - C_l(k)\frac{\cos(kR - l\pi/2)}{kR}, \qquad R \to \infty. \tag{5.20}$$

If we define

$$B_l(k) \equiv A_l(k)\cos(\delta_l(k)), \tag{5.21}$$
$$-C_l(k) \equiv A_l(k)\sin(\delta_l(k)), \tag{5.22}$$

we can rewrite equation (5.20) as

$$P_l(k,R) = \frac{A_l(k)}{kR}\sin(kR - l\pi/2 + \delta_l(k)), \qquad R \to \infty, \tag{5.23}$$

with

$$\tan\delta_l(k) \equiv -\frac{C_l(k)}{B_l(k)}. \tag{5.24}$$

This definition may be used to rewrite equation (5.18) as

$$P_l(k,R) = B_l(k)(j_l(kR) - \tan(\delta_l(k))n_l(kR)), \qquad R > a. \tag{5.25}$$

The *phase-shift* $\delta_l(k)$ introduced in equation (5.24) turns out to be very important. At long range $R > a$ the effect of a potential $V(R)$ will be to introduce a phase shift relative to a solution obtained with $V = 0$. We may say that the phase shift gives information about the scattering potential, but we must be aware that there is not a one to one correspondence, several potentials may give the same phase shift.

The above statements implies that $V = 0 \Rightarrow \delta_l(k) = 0$. This follows from the definitions of $B_l(k)$ and $C_l(k)$ in equations (5.21) and (5.22) since if $V = 0$, equation (5.18) gives the general solution for all R. From our investigation of $P_l(k,R)$ for small R, we expect j_l or n_l to be irregular at $R = 0$. This turns out to be $n_l(kR)$ (seen from a series expansion of $j_l(kR)$ and $n_l(kR)$), thus we must require $C_l(k) = 0$ which indicates $\delta_l(k) = 0$. For a free particle we then find

$$P_l(k,R) = \frac{A_l(k)}{kR}\sin(kR - l\pi/2), \qquad R \to \infty. \tag{5.26}$$

Using equations (5.4) and (5.13) together with equation (5.26) we can find the free particle wavefunction ψ_{in} represented in terms of Legendre polynomials in the $R \to \infty$ limit

$$\begin{aligned}\psi_{\text{in}} = Ae^{ikz} &= \sum_{l=0}^{\infty} P_l(k,R)\mathcal{L}_l(\cos\theta), \\ &= \sum_{l=0}^{\infty} \frac{A_l(k)}{kR}\sin(kR - l\pi/2)\mathcal{L}_l(\cos\theta), \qquad R \to \infty.\end{aligned} \tag{5.27}$$

Remark: It may be appropriate with a remark on what will be done, it is rather easy to lose the way in the algebra that follows. Our approach is to use equation (5.27) to express the first term in equation (5.8) as a series of Legendre polynomials. We want to identify $A_l(k)$ and $f(\theta)$ by comparing with equation (5.23) used in equation (5.13). The resulting expression is also valid in the $R \to \infty$ limit, making it possible to identify $A_l(k)$ and $f(\theta)$.

We start by finding $A_l(k)$ in equation (5.27)[3]

$$A_l(k) = \frac{AkR}{\sin(kR - l\pi/2)} \int_{-1}^{1} e^{ikR\cos\theta} \mathcal{L}_l(\cos\theta) \mathrm{d}\theta, \tag{5.29}$$

$$\simeq A(2l+1)i^l. \tag{5.30}$$

Thus we find

$$\psi_{\text{in}} = A \sum_{l=0}^{\infty} (2l+1) i^l \frac{\sin(kR - l\pi/2)}{kR} \mathcal{L}_l(\cos\theta), \qquad R \to \infty. \tag{5.31}$$

Using this result we write equation (5.8) as

$$\psi_{\mathbf{k}}(R) = A \left(\sum_{l=0}^{\infty} (2l+1) i^l \sin(kR - l\pi/2)(kR)^{-1} \mathcal{L}_l(\cos\theta) + f(k,R,\theta) \frac{e^{ikR}}{R} \right), \quad R \to \infty. \tag{5.32}$$

Now look only at even l values ($l = 0, 2, 4, 6...$)

$$\psi_{\mathbf{k}}(R) = A \left(\sum_{\text{even l}} (2l+1)(-1)^l \left(\frac{e^{ikR} - e^{-ikR}}{2i} \right) (kR)^{-1} \mathcal{L}_l(\cos\theta) + f(k,R,\theta) \frac{e^{ikR}}{R} \right), \tag{5.33}$$

$$= A \left(\frac{e^{ikR}}{R} \left[- \sum_{\text{even l}} \frac{i}{2k} (2l+1) \mathcal{L}_l(\cos\theta) + f(k,R,\theta) \right] + \frac{e^{-ikR}}{R} \left[\sum_{\text{even l}} \frac{i}{2k} (-1)^l (2l+1) \mathcal{L}_l(\cos\theta) \right] \right). \tag{5.34}$$

Also consider odd values of l ($l = 1, 3, 5, 7...$)

$$\psi_{\mathbf{k}}(R) = A \left(- \sum_{\text{odd l}} (2l+1)(-1)^l i \left(\frac{e^{ikR} + e^{-ikR}}{2} \right) (kR)^{-1} \mathcal{L}_l(\cos\theta) + f(k,R,\theta) \frac{e^{ikR}}{R} \right), \tag{5.35}$$

$$= A \left(\frac{e^{ikR}}{R} \left[- \sum_{\text{odd l}} \frac{i}{2k} (2l+1) \mathcal{L}_l(\cos\theta) + f(k,R,\theta) \right] + \frac{e^{-ikR}}{R} \left[\sum_{\text{odd l}} \frac{i}{2k} (-1)^l (2l+1) \mathcal{L}_l(\cos\theta) \right] \right). \tag{5.36}$$

Since we have been able to write the results for both odd and even l so that the expressions coincides, we may write for all l

$$\psi_{\mathbf{k}}(R) = A \left(\frac{e^{ikR}}{R} \left[- \sum_{l=0}^{\infty} \frac{i}{2k} (2l+1) \mathcal{L}_l(\cos\theta) + f(k,R,\theta) \right] + \frac{e^{-ikR}}{R} \left[\sum_{l=0}^{\infty} \frac{i}{2k} (-1)^l (2l+1) \mathcal{L}_l(\cos\theta) \right] \right), \quad R \to \infty. \tag{5.37}$$

[3]Here we use the properties

$$\int_{-1}^{1} \mathcal{L}_l(x) \mathcal{L}_{l'}(x) \mathrm{d}x = \frac{2}{2l+1} \delta_{ll'} \tag{5.28}$$

and $\mathcal{L}_l(1) = 1$ while $\mathcal{L}_l(-1) = (-1)^l$. This calculation is also done in the $R \to \infty$ limit, and a very similar calculation can be found in [55], page 277.

On the other hand we can find $\psi_{\mathbf{k}}(R)$ by using equations (5.13) and (5.23)

$$\psi_{\mathbf{k}}(R) = \sum_{l=0}^{\infty} A_l(k) \frac{e^{ikR - l\pi/2 + \delta_l(k)} - e^{-ikR + l\pi/2 - \delta_l(k)}}{2ikR} \mathcal{L}_l(\cos\theta), \qquad R \to \infty. \tag{5.38}$$

Equations (5.37) and (5.38) must be equal. This implies

$$A_l(k) = A(2l+1) i^l e^{i\delta_l(k)}, \tag{5.39}$$

$$f(k,\theta) = \frac{1}{2ik} \sum_{l=0}^{\infty} (2l+1)(e^{2i\delta_l(k)} - 1)\mathcal{L}_l(\cos\theta), \tag{5.40}$$

$$= \frac{1}{2ik} \sum_{l=0}^{\infty} (2l+1)(S_l(k) - 1)\mathcal{L}_l(\cos\theta), \tag{5.41}$$

$$= \frac{1}{k} \sum_{l=0}^{\infty} (2l+1) e^{i\delta_l(k)} \sin\delta_l(k) \mathcal{L}_l(\cos\theta), \tag{5.42}$$

where the *scattering matrix element* $S_l(k) \equiv e^{2i\delta_l(k)}$ has been defined. We take this opportunity to also define the *partial wave amplitude* $\mathcal{A}_l(k)$

$$\mathcal{A}_l(k) \equiv \frac{1}{2ik}\left(e^{2i\delta_l(k)} - 1\right) = \frac{1}{k} e^{i\delta_l(k)} \sin\delta_l(k), \tag{5.43}$$

enabling us to write equation (5.42) as

$$f_l(k,\theta) = \sum_{l=0}^{\infty} (2l+1)\mathcal{A}_l(k)\mathcal{L}_l(\cos\theta). \tag{5.44}$$

From equation (5.10) we also calculate the differential cross section

$$\frac{\mathrm{d}\sigma}{\mathrm{d}\Omega} = \frac{1}{k^2} \sum_{l=0}^{\infty} \sum_{l'=0}^{\infty} (2l+1)(2l'+1) e^{i\delta_l(k)} e^{-i\delta_{l'}(k)} \sin\delta_l(k) \sin\delta_{l'}(k) \mathcal{L}_l(\cos\theta)\mathcal{L}_{l'}(\cos\theta). \tag{5.45}$$

We can find the total cross section by integration

$$\sigma = \frac{2\pi}{k^2} \sum_{l=0}^{\infty} \sum_{l'=0}^{\infty} (2l+1)(2l'+1) e^{i\delta_l(k)} e^{-i\delta_{l'}(k)} \sin\delta_l(k) \sin\delta_{l'}(k) \int_0^{\pi} \mathcal{L}_l(\cos\theta)\mathcal{L}_{l'}(\cos\theta) \sin\theta \mathrm{d}\theta. \tag{5.46}$$

A change of variable, $u = \cos\theta$, and once again using the orthogonality relation for the Legendre polynomials results in

$$\sigma = \frac{4\pi}{k^2} \sum_{l=0}^{\infty} (2l+1) \sin^2\delta_l(k). \tag{5.47}$$

5.5 Further analysis of the phase shift

From the preceding sections it is apparent that the phase shift is a very important concept in scattering theory. But how to obtain $\delta_l(k)$ is still unclear. This section seeks to answer this. We start by considering two different solutions $u_l(k,R)$ and $w_l(k,R)$ of the Schrödinger equation, corresponding to two different potentials $V(R)$ and $\tilde{V}(R)$ respectively. The asymptotic expressions for u and w as $R > a$ are given by equation (5.18)

$$u_l(k,R) = R\left(j_l(kR) + \tan\delta_l(k) n_l(kR)\right), \tag{5.48}$$

$$w_l(k,R) = R\left(j_l(kR) + \tan\tilde{\delta}_l(k) n_l(kR)\right), \tag{5.49}$$

with the normalization $B_l(k) = 1$. This implies the following relations

$$\tan\delta_l(k) - \tan\tilde{\delta}_l(k) = u_l w_l' - u_l' w_l, \tag{5.50}$$

$$\frac{\mathrm{d}}{\mathrm{d}R}(\tan\delta_l(k) - \tan\tilde{\delta}_l(k)) = u_l w_l'' - u_l'' w_l. \tag{5.51}$$

From the Scrödinger equations satisfied by u_l and w_l (for all R) it is readily found

$$u_l'' = \left\{\frac{l(l+1)}{R^2} - k^2 + \frac{V(R)2\mu}{\hbar^2}\right\} u_l, \tag{5.52}$$

$$w_l'' = \left\{\frac{l(l+1)}{R^2} - k^2 + \frac{\tilde{V}(R)2\mu}{\hbar^2}\right\} w_l. \tag{5.53}$$

Inserting equations (5.52) and (5.53) into equation (5.51) and integrating yields

$$\tan\delta_l(k) - \tan\tilde{\delta}_l(k) = \frac{2\mu k}{\hbar^2}\int_0^\infty w_l(k,R)(\tilde{V}(R) - V(R))u_l(k,R)\mathrm{d}R. \tag{5.54}$$

Let $\tilde{V}(R) = 0$, which implies $\tilde{\delta}_l(k) = 0$

$$\tan\delta_l(k) = -\frac{2\mu k}{\hbar^2}\int_0^\infty j_l(kR)V(R)u_l(k,R)R\mathrm{d}R, \tag{5.55}$$

or if we use the radial function $P_l(k,R)$

$$\tan\delta_l(k) = -\frac{2\mu k}{\hbar^2}\int_0^\infty j_l(kR)V(R)P_l(k,R)R^2\mathrm{d}R. \tag{5.56}$$

Using this integral we can in principe determine $\delta_l(k)$. Notice however that we have to solve the *exact* Schrödinger equation (or rather find an approximation to the solution) to be able to perform the integration above, since $P_l(k,R)$ must be known also for $R \leq a$.

The boundary conditions used to obtain the radial function $P_l(k,R)$ for $R \leq a$ are

1. $P_l(k,0)$ =finite. If $V(0) \to \infty$ we require $P_l(k,0) = 0$. Either way $n_l(R)$ must be excluded.

2. $P_l(k,R)$ used for $R \leq a$ corresponds smoothly to the 'normalized' function $P_l(k,R) = j_l(kR) - \tan\delta_l n_l(k)$ used for $R \geq a$. Thus we require

$$P_l(k,a)^{R\leq a} = P_l(k,a)^{R\geq a}, \tag{5.57}$$

$$\left.\frac{\mathrm{d}P_l(k,R)^{R\leq a}}{\mathrm{d}R}\right|_{R=a} = \left.\frac{\mathrm{d}P_l(k,R)^{R\geq a}}{\mathrm{d}R}\right|_{R=a}. \tag{5.58}$$

The continuity requirements for $P_l(k,R)$ and $\frac{\mathrm{d}P_l(k,R)}{\mathrm{d}R}$ can be fulfilled by requiring the logarithmic derivative to be continuous at $R=a$.[4]

To continue further we define the logarithmic derivative of the interior ($R \leq a$) solution to be

$$\gamma_l(k) \equiv \frac{1}{P_l(k,a)} \frac{\mathrm{d}P_l(k,R)}{\mathrm{d}R}\bigg|_{R=a}. \tag{5.60}$$

Matching the exterior ($R \geq a$) and interior solutions requires the two logarithmic derivatives to be equal. The logarithmic derivative of the exterior solution (5.25) is easily found from equation (5.59). We also use $\frac{\mathrm{d}j_l(kR)}{\mathrm{d}R} = k\frac{\mathrm{d}j_l(kR)}{\mathrm{d}(kR)}$ to find

$$\gamma_l(k) = \frac{\frac{\mathrm{d}j_l(kR)}{\mathrm{d}(kR)}\Big|_{kR=ka} - \tan\delta_l(k)\frac{\mathrm{d}n_l(kR)}{\mathrm{d}(kR)}\Big|_{kR=ka}}{j_l(ka) - \tan\delta_l(k) n_l(ka)} = \frac{k[j'(ka) + \tan\delta_l(k) n_l'(ka)]}{j_l(ka) - \tan\delta_l(k) n_l(ka)}, \tag{5.61}$$

with $j_l'(kR)$ and $n_l'(kR)$ indicating derivatives with respect to kR. Solving this equation for $\tan\delta_l(k)$ yields

$$\tan\delta_l(k) = \frac{kj_l'(ka) - \gamma_l(k) j_l(ka)}{kn_l'(ka) - \gamma_l(k) n_l(ka)}. \tag{5.62}$$

5.5.1 Behaviour of the phase shift at low energies. Scattering length.

Since we are concerned with cold collisions in this chapter, the low energy limit is important. In the low energy limit we have $k \to 0$ and therefore also $kR \to 0$. We investigate the phase shift in this limit, using a series expansion[5] of the spherical Bessel and Neumann functions $j_l(x)$ and $n_l(x)$ respectively

$$j_l(x) = \frac{x^l}{(2l+1)!!}\left(1 - \frac{\frac{1}{2}x^2}{2l+3} + \cdots\right), \tag{5.63}$$

$$n_l(x) = -\frac{(2l-1)!!}{x^{l+1}}\left(1 - \frac{\frac{1}{2}x^2}{(1-2l)} + \cdots\right), \tag{5.64}$$

with $(2l+1)!! \equiv 1\cdot 3\cdot 5\cdots(2l+1)$. Keeping only the first term in both expansions (5.63) and (5.64) and inserting these in equation (5.62) yields

$$\tan\delta_l(k) \simeq \frac{k\frac{l(ka)^{l-1}}{(2l+1)!!} - \gamma_l\frac{(ka)^l}{(2l+1)!!}}{k\frac{(l+1)(2l-1)!!}{(ka)^{l+2}} + \gamma_l(k)\frac{(2l+1)!!}{(ka)^{l+1}}}, \tag{5.65}$$

$$= \frac{(ka)^{2l+1}}{(2l+1)!!(2l-1)!!}\frac{l - a\gamma_l(k)}{l+1+a\gamma_l(k).} \tag{5.66}$$

[4] The logarithmic derivative is

$$D[\ln f(x)] = \frac{f'(x)}{f(x)}. \tag{5.59}$$

Both $f(x)$ and $f'(x)$ are required to be continues at $x=a$, this is seen (from equation (5.59)) to be fulfilled when the logarithmic derivatives of $f(x)$ on both sides of a, at $x=a$ are equal.

[5] Details of these expansions can be found in [54].

This implies (in the $k \to 0$ limit)

$$\delta_l(k) = (ka)^{2l+1} \frac{1}{(2l+1)!!(2l-1)!!} \frac{l - a\hat{\gamma}_l}{l+1+a\hat{\gamma}_l}. \tag{5.67}$$

The transition from equation (5.66) to equation (5.67) can be done using $\arctan x = x$ when $x \to 0$. We have also defined

$$\hat{\gamma}_l \equiv \lim_{k\to 0} \gamma_l(k). \tag{5.68}$$

Equation (5.67) allows us to write $\delta_l(k) = c_l k^{2l+1}$ with c_l as a l dependent, k independent constant. Consider now the partial wave amplitude $\mathcal{A}_l(k)$ (defined in equation (5.43)), still in the $k \to 0$ limit

$$\mathcal{A}_l(k) \to \frac{1}{2ik}\left(1 + 2ic_l k^{2l+1} - 1\right) = c_l k^{2l}. \tag{5.69}$$

From this expression we can see that for $l > 0$, all partial cross sections vanishes as $k \to 0$. At very low energies the scattering is therefore isotropic. Now we define the very important scattering length α

$$\boxed{\lim_{k\to 0} k \cot \delta_0(k) \equiv -\frac{1}{\alpha},} \tag{5.70}$$

and investigate $\mathcal{A}_0(k)$ in the $k \to 0$ limit. From equation (5.43) it follows

$$\mathcal{A}_0(k) = \frac{1}{k} \sin \delta_0(k) e^{i\delta_0(k)}, \tag{5.71}$$

and in the limit

$$\lim_{k\to 0} \mathcal{A}_0(k) = \frac{\sin \delta_0(k)}{k} \cdot 1 = -\alpha. \tag{5.72}$$

To sum up, we have found the scattering length, differential cross section and cross section to be

$$\lim_{k\to 0} \mathcal{A}_0(k) = -\alpha, \qquad \lim_{k\to 0} \frac{\mathrm{d}\sigma}{\mathrm{d}\Omega} = \alpha^2, \qquad \lim_{k\to o} \sigma_{\text{tot}} = 4\pi\alpha^2. \tag{5.73}$$

At temperatures of a few Kelvin, the energy is of the order of $1\mathrm{cm}^{-1}$ and very few partial waves contribute to the cross section, while the $l = 0$ partial wave is expected to dominate. If we consider temperature $T \leq 1\mu\mathrm{K}$ only the s-wave ($l = 0$) will contribute and the cross section will be given accurately by

$$\sigma_{\text{tot}} = 4\pi\alpha^2. \tag{5.74}$$

Notice from the previous equations that the scattering length and cross section can be determined once the phase shift is known. The scattering length α is very sensitive to small changes in the potential. This we know from experience after calculating scattering lengths in section 5.6, and it has also been reported by others [48]. Hence, to obtain reliable cross sections accurate potentials will be required. The potentials are calculated from the usual

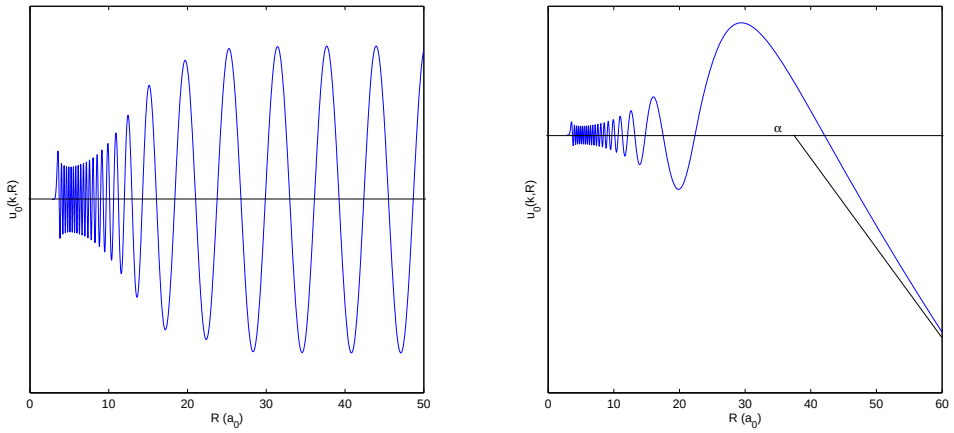

Figure 5.2. *Wavefunctions for unbound states used to describe collisions between two atoms. Figures to the left and right are the wavefunctions corresponding to the same potential (ground state* Li*), but at different energies. The wavefunctions are found solving equation (5.14) with arbitrary initial conditions for the purpose of this illustration. The figure to the right corresponds to very low-energy scattering, the black line represents an asymptote the wavefunction approaches for large R values. The scattering length is the R value where this asymptote crosses the R-axis.*

Born-Oppenheimer approximation (which is expected to be adequate for such a cold and slow collision), but often relativistic effects are included in order to get the accuracy needed in the calculation of α. In section 5.7 we present a calculation of the scattering length based on our calculated interatomic potential.

When calculating the scattering length from the phase shift we may use equation (5.70). This equation is however only valid in the limit $k \to 0$, so a series expansion is sometimes used to improve accuracy for small non-zero k values

$$k \cot \delta_0(k) = -\frac{1}{\alpha} + \frac{1}{2} R_e k^2, \tag{5.75}$$

$$R_e = 2 \int_0^\infty (w_0^2(k,R) - u_0(k,R)^2) \mathrm{d}R, \tag{5.76}$$

$$w_0(k,R) = \frac{\sin(kR + \delta_0)}{\sin \delta_0}. \tag{5.77}$$

$u_0(k,R)$ is a solution of the radial equation behaving as $w_0(k,R)$ for large R values. This expansion is due J. M. Blatt and J. D. Jackson [58].

5.6 Numerical methods for calculating scattering lengths

Based on the partial waves theory outlined in previous sections, and our interatomic potential curves presented in chapter 3, we have the basis for a numerical calculation of the phase shift and scattering length. It could be questioned whether or not our potential curves possesses the accuracy needed for such delicate calculations. In this section we present three different calculation schemes, whereas two have been implemented numerically.

5.6.1 Method I (not implemented)

This is perhaps the most professional approach used by the pro's when they seek to calculate high precision scattering lengths. The aim is to solve the differential equation

$$\left\{\frac{1}{R^2}\frac{\mathrm{d}}{\mathrm{d}R}\left(R^2\frac{\mathrm{d}}{\mathrm{d}R}\right)+k^2-\frac{2\mu V(R)}{\hbar^2}-\frac{l(l+1)}{R^2}\right\}P_l(k,R)=0, \tag{5.78}$$

with boundary conditions $P_l(k,0)=0$ and $P_l(k,R)=\frac{\sin(kR-\frac{l}{2}\pi+\delta_l)}{kR}$ for $R>a$. a is some cut-off radius where the potential is zero (or small enough to be neglected). To solve equation (5.78) is not as easy as just solving a differential equation numerically[6], the boundary conditions involve δ_l which we set out to calculate. This is handled by using two initial conditions $u(k,0)=0$ and $u'(k,0)=b$. To start the process one chooses/guesses on a b-value and find the corresponding wavefunction $u_l(k,R)$ by solving equation (5.78). One then calculates $\tan\delta_l$ by the use of equation (5.55)

$$\tan\delta_l=-\frac{2\mu k}{\hbar^2}\int_0^\infty j_l(kR)V(R)P_l(k,R)R^2\mathrm{d}R. \tag{5.79}$$

To check if the asymptotic behavior is correct one may use the logarithmic derivative and require that the following equality must hold

$$\left[\frac{1}{P_l(k,R)}\frac{\mathrm{d}P_l(k,R)}{\mathrm{d}R}\right]_{R=a}=\frac{k[j_l'(ka)-\tan\delta_l(k)n_l'(ka)]}{j_l(ka)-\tan\delta_l(k)n_l(ka)}. \tag{5.80}$$

Probably this equality will not hold an one will have to return to the differential equation (5.78) and solve it several times with new initial conditions $u'(k,0)=b$ each time. The trick is to vary $u'(k,0)$ in a systematic way until a solution with the correct asymptotic behavior is obtained.

5.6.2 Method II

This method is probably somewhat less accurate and may require a longer running time than method I. It has however been the method chosen to implement for several reasons: 1) the method is easy to program and very suitable for MATLAB, 2) because we do not have chance on a many digit precision accuracy anyway, the difference between this method and method I should have no significance. We also believe that by running with a large N (explained below) this method will give the accuracy needed. 3) This method has been given a beautiful and detailed explanation in [51], but also described less detailed in [54]. The more uninteresting details have been referred to appendix C together with the actual computer code.

We work with the reduced potential $U(R)\equiv\frac{2\mu V(R)}{\hbar^2}$, and divide it into N constant pieces with a width b. The height of the potential in each segment is taken to be the linearly mean value between $U(jb)$ and $U((j-1)b)$,

$$U_j\equiv 0.5(U((j-1)b)+U(jb)), \qquad j=1,2,3,...,N. \tag{5.81}$$

[6]Equation (5.78) can of course not be solved analytically even in the $l=0$ case without serious approximations regarding $V(R)$.

Further we define α_j which we allow to take complex values

$$\alpha_j \equiv \sqrt{k^2 - U_j}. \tag{5.82}$$

Now equation (5.78) for one of the N segments reads (the l index on the radial function P is neglected for an easier notation, we use j to designate different segments)

$$\left\{ \frac{1}{R^2} \frac{\mathrm{d}}{\mathrm{d}R} \left(R^2 \frac{\mathrm{d}}{\mathrm{d}R} \right) + \alpha_j^2 - \frac{l(l+1)}{R^2} \right\} P_j(k, R) = 0, \tag{5.83}$$

with the *exact* solution

$$P_j(k, R) = A_j j_l(kR) + B_j n_l(kR). \tag{5.84}$$

The A_j and B_j coefficients are also l dependent, but this dependence is suppressed in the notation. Of special interest is $l = 0$, but this method can be used to find $\delta_l(k)$ also for higher l values. Further there are two things to consider; the spherical Neumann function $n_l(kR)$ is irregular at $R = 0$ so we have to set $B_0 = 0$ (the subscript 0 indicates segment 0, not partial wave $l = 0$). Secondly we always have to require the wavefunction and the first derivative of the wavefunction to be continuous between each segment. These requirements can be expressed in terms of matrices, and be written

$$M(R_j, \alpha_j) \begin{pmatrix} A_j \\ B_j \end{pmatrix} = M(R_{j+1}, \alpha_{j+1}) \begin{pmatrix} A_{j+1} \\ B_{j+1} \end{pmatrix}, \quad \text{with} \quad M(\alpha, R) \equiv \begin{pmatrix} j_l(\alpha R) & n_l(\alpha R) \\ \alpha j_l'(\alpha R) & \alpha n_l'(\alpha R) \end{pmatrix}. \tag{5.85}$$

Clearly this enables us to write

$$\begin{pmatrix} A_{\text{out}} \\ B_{\text{out}} \end{pmatrix} = W \begin{pmatrix} A_0 \\ 0 \end{pmatrix}, \tag{5.86}$$

with W as a 2×2 matrix that is a product of M matrices and M^{-1} matrices. The complete W matrix is a product of $2N$ matrices. For the exact form of the W matrix, see appendix C. Notice that $B_0 = 0$ in equation (5.86). To determine the phase shift we consider $P_l(k, R)$ as $R \to \infty$. $P_l(k, R)$ in this limit is given by (see also equation (5.20))

$$P_l(k, R) = B_{\text{out}} \sin(kR - l\pi/2) - C_{\text{out}} \cos(kR - l\pi/2), \tag{5.87}$$

$$= A_{\text{out}} \sin(kR - l\pi/2 + \delta_l), \qquad R \to \infty, \tag{5.88}$$

with

$$\tan \delta_l(k) \equiv -\frac{C_{\text{out}}}{B_{\text{out}}}, \qquad A_{\text{out}} = \sqrt{B_{\text{out}}^2 + C_{\text{out}}^2}. \tag{5.89}$$

C_{out} and B_{out} are the coefficients of solution (5.87) found outside the potential for $R > a$.

From equation (5.86) we can find A_{out} and B_{out} in terms of A_0, and the different entries of matrix W. This gives

$$\tan \delta_l(k) = -\frac{W_{21}}{W_{11}}. \tag{5.90}$$

The theory presented above gives a short outline of the method. For large N values this method should be rather good, but not very efficient. For a more detailed treatment of the components of both the W matrix and the M matrix, see appendix C.

5.6.3 Method III

For the sake of comparison, a third method has been implemented. The basis for calculating scattering lengths with this method is a set of equations obtained by Gribakin and Flambaum [52]. Using a semiclassical approach they found the scattering length to be given by the following expressions in the case of a long range potential $V(R) \propto \frac{1}{R^6} +$ higher order R^{-n}

$$\alpha = \bar{\alpha}\left[1 - \tan\left(\Phi - \frac{\pi}{8}\right)\right], \tag{5.91}$$

$$\bar{\alpha} = \frac{\sqrt{2}}{2}\sqrt{\left(\frac{\sqrt{2\mu C_6}}{4\hbar}\right)}\left(\frac{\Gamma(3/4)}{\Gamma(5/4)}\right), \tag{5.92}$$

$$\Phi = \frac{\sqrt{2\mu}}{\hbar}\int_{R_0}^{\infty}\sqrt{-V(R)}\mathrm{d}R. \tag{5.93}$$

$V(R)$ is always negative on the interval of integration since the potential is scaled in such a way that $V(\infty) = 0$. The potential is measured relative to the dissociation energy. R_0 is the R value where the potential crosses from positive to negative values when the above convention of scaling is used (the integral will converge).

This method, although simple, has previously been used in [48] and [49] with success, and seems to be accurate.

Expressions (5.91) - (5.93) has been used to calculate the scattering lengths using our own potential (see chapter 3) extended to long range (see next section).

5.7 Results

The scattering lengths were calculated using both methods II and III for two different potentials. The two potentials used were of course our own ^{6}Li potential calculated in chapter 3, and in addition the potential adopted by Côté, Dalgarno and Jamieson (hereafter CDJ potential) in [48] (^{7}Li potential). The reason for calculating the scattering length also for this potential was to check that our methods of calculation were reliable. The potential used in [48] consists of data from several sources, we were able to get hold of most of these, but one value at $3.00a_0$ proved impossible to retrieve (invalid citation).

Both potentials were at long range assumed to be

$$V(R) = -\frac{C_6}{R^6} - \frac{C_8}{R^8} - \frac{C_{10}}{R^{10}}, \tag{5.94}$$

with C_6, C_8 and C_{10} taken from [48] for ^{7}Li and from [50] for ^{6}Li. Note that these coefficients C_n are given in terms of $energy \times length^n$ with $energy$ measured in atomic units of energy and length in terms of a_0. Côté *et. al.* [48] uses an additional term in $V(R)$ at long range, namely

$$V(R) = 0.001288R^{4.558}e^{-1.259R}. \tag{5.95}$$

This extra term has been included when calculating scattering lengths for ^{7}Li but no such term has been used in the calculations done for ^{6}Li. The reduced masses used in the calculations are $2821.99\mathrm{MeV/c^2}$ and $3267.68\mathrm{MeV/c^2}$ for ^{6}Li and ^{7}Li respectively.

Our results for both potentials are in table 5.1.

	Method II	Method III	Believed to be
^{6}Li	$73.5a_0$	$66.2a_0$	$(47 \pm 3)a_0$
^{7}Li	$26.3a_0$	$30.1a_0$	$(34 \pm 5)a_0$

Table 5.1. *Calculated scattering lengths for ^{6}Li and ^{7}Li. Blue color indicates results obtained with our own potential, while red signals results obtained with the CDJ potential. The "believed to be" column is taken from [53].*

The results for method II in table 5.1 are obtained by setting $V(R) = 0$ for $R = 500a_0$. We have used $N = 200000$ and there seems to be nothing to gain by increasing N further. The criteria for setting $V(R) = 0$ for some $R = a$ is that $k^2 \gg U(a)$. This requirement is fully met at $a = 500$. This very large a value is chosen since k is small at such low energies.

The k values used corresponds to energies of the order 10^{-8}eV and below, where the scattering length and thereby the cross section are constant [48]. As one increases the energy several partial waves will start to contribute, while at sufficiently low energies only the s-wave contributes and the scattering length approaches a constant according to equation (5.70). (See [48] and the work done there on higher partial waves at different energies).

For both potentials we have used splines to interpolate values in the potential curve. In addition the ^{6}Li data between $7a_0 - 8a_0$ have been smoothed by fitting a polynomial to best match these and join the rest of the potential curve. This was done since some of the calculated values in this interval had small oscillations. A probable reason for this is a forced change in the configuration when running the MultiMOD program on this interval (intruders). Without doing this, the results in table 5.1 would be somewhat different.

5.7.1 Discussion of the results

The calculated scattering lengths are quite good, although they are not within the interval listed in the "Believed to be column" in 5.1. There are several reasons for this.

For our own potential the small discrepancies between our calculated values and the more accurate "believed to be" column can have several sources. First of all our potential is calculated *ab initio* and one must be aware that the scattering lengths we are comparing to are obtained from empirical potentials. On this background the results in table 5.1 may be seen as a compliment to our potential.

Regarding the CDJ potential (^{7}Li potential) the results obtained should be compared to the value $36.9a_0$ found by Côté *et al.* [48]. Our results are somewhat lower, this is confirmed by both method II and method III. Why this is one can only speculate. However, we do not use the *exact* same potential since the value at $3.00a_0$ is different. Further, we have no information on what kind of interpolation method that has been used in [48].

Although the results are good, one can not neglect that the scattering length is extremely sensitive to relatively small changes in the potential. Our potential may not posses the accuracy required to reliable calculate this sensitive parameter. In fact even Côté *et al.* [48] with their high reliability both in data and calculating methods, reports accuracy to be inadequate to predict scattering lengths with certainty.

Having found the scattering length we can of course calculate the cross section. In the

low energy limit we have (see also equation (5.73))

$$\sigma \propto \alpha^2 \approx 10^{-17}\mathrm{m}^2. \tag{5.96}$$

We use proportional to and not equal to, this because we really should account for the fact that ^{6}Li are bosons. This changes the constant 4π in equation (5.73). However, here we are only interested in the magnitude of the cross section and do not care about the constant in front.

The scattering length and cross section are the important quantities of a cold collision. In fact we can for most cases model an ultracold gas of atoms as a gas of hard spheres with radius α, thus the scattering length completely determines the interactions in a gas. Therefore the scattering length is important to all phenomena where atoms collide at ultracold temperatures. This may be in BEC experiments or in different trapping arrangements. For a BEC, the scattering length is important since its magnitude determines the evaporative cooling rate, while the sign determines the stability of the condensate. A stable condensate will never be achieved with atoms that have negative scattering lengths.

In the next chapter on Feshbach resonances the scattering length will be further investigated, and its importance will become apparent. We will consider the effect of varying the scattering length, and see just how central this quantity is to the interatomic interactions in a gas.

Chapter 6

Feshbach resonances

In this chapter the rich field of physics related to the Feshbach resonances will be investigated. There are two questions that we seek to answer; 1) What is a Feshbach resonance? 2) What are the implications of such a resonance? Both questions are important since the Feshbach resonance opens numerous of new opportunities. Among these are several applications to Bose-Einstein condensation (BEC), making BEC possible for atomic species with unfavorable scattering lengths and also for molecules. Feshbach resonances can also be utilized to produce cold molecules. This again makes Feshbach resonances interesting also in quantum computations with the cold molecules acting as q-bits.

Perhaps the most spectacular application so far is the possibility of making a Fermi gas go through a phase transition from BEC to a superfluid Bardeen-Cooper-Schrieffer (BCS) state by tuning the interaction strength in the Fermi gas, or equivalent, tuning the s-wave scattering length α.

Unfortunately the physics surrounding these phenomena are quantitatively hard to study. Often we will have to settle for a somewhat simplified version of the theories. The full indept mathematical treatments are too complicated to be included here. However, much of the relevant physics and key ideas will be highly transparent, and make no mistake, there are beautiful physics in this chapter.

6.1 What is a Feshbach resonance?

A *Feshbach resonance* introduces a superposition of two states into the wavefunction of two colliding atoms. One of these states is a continuum state and the other one a bound state

$$|\Psi(B,E,R)\rangle = f(B,E)|\psi_{\text{bound}}\rangle + g(B,E)|\psi_{\text{cont}}\rangle. \tag{6.1}$$

The coefficients in this superposition $f(B,E)$ and $g(B,E)$ is determined by an external B-field and the energy of the incoming channel (the colliding atoms). A Feshbach resonance occurs when one bound state coincides in energy with the collision energy in an open and different scattering channel.

We consider two ground state atoms approaching along the molecular ground state potential. The two ground state atoms represents the open channel. The closed channel is a bound molecular level belonging to a different electronic state (different interatomic poten-

tial). In Li_2 we may write for this process

$$\underbrace{\mathrm{Li}(^2\mathrm{S}) + \mathrm{Li}(^2\mathrm{S})}_{\text{open inital channel}} \rightarrow \underbrace{\mathrm{Li}_2(^3\Sigma_u^+(M_F))}_{\text{closed final channel}} . \tag{6.2}$$

There may exist many open and closed channels with different combinations of hyperfine- and hyperfine Zeeman levels. The initial channel is always a s-channel ($l = 0$), while the closed channel in principle can take on any l value. It is however a requirement that all channels must have the same projection of the total angular momentum, $M_F = M_{F_1} + M_{F_2}$ along the magnetic field axis, with M_{F_1} and M_{F_2} as the hyperfine Zeeman levels of atom 1 and atom 2 respectively. Since the open and closed channels have different magnetic moments they will in general interact with a magnetic field in different ways. This enables a tuning of the bound molecular level so that it matches the energy of the $^2\mathrm{S} + {}^2\mathrm{S}$ asymptotic limit. The coupling between the open channel and the s-wave part of the closed channel arises through the central part of the molecular potential. In figure 6.1 we illustrate this process schematically using interatomic potentials from Li_2. This figure shows a coupling between the closed channel with $S = 1$ and the open channel with $S = 0$.

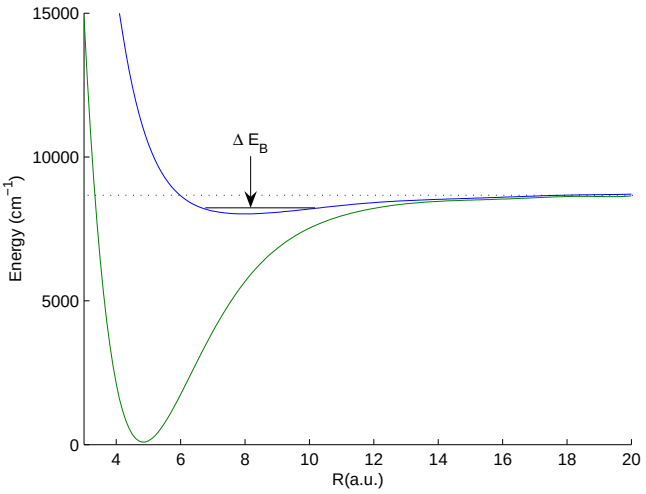

Figure 6.1. *The singlet (in green) and triplet (in blue) ground state in* Li_2*. The dotted line indicates the energy of two colliding atoms while the solid (black) line is a bound level in the shallow triplet state. By using a magnetic field it is possible to shift the energy of the bound level (by* E_B*), bringing it into resonance with the continuum.*

We noticed in the preceding chapter how the scattering length is dependent upon the position of the last bound state in a potential. It is therefore to be expected that tuning the position of such a state influences the scattering length. This proves to be the case, a Feshbach resonance changes the s-wave scattering length α (defined in chapter 5, equation (5.70)) according to the equation

$$\alpha(B) = \alpha\left(1 - \frac{\Delta B}{B - B_0}\right), \tag{6.3}$$

with B_0 defined as the magnetic field where the bound state is shifted equal to the collision energy of the open channel. ΔB is the width of the resonance and α is the scattering length far from the resonance. ΔB as the width of the resonance is determined by the strength of the interaction between the open and closed channels. This ability to change the scattering length can also be understood from the relationship between scattering lengths and wavefunctions discussed in the previous chapter. Introducing a superposition as in equation (6.1) will change the wavefunction and thereby the scattering length. More details on equation (6.3) can be found in [62].

This ability to change the scattering length is the main reason for the many different research areas utilizing Feshbach resonances. It makes effective tuning of the interactions in a gas possible as we will see.

6.2 Toy model of a Feshbach resonance

To find a real Feshbach resonance would mean calculating couplings between different hyperfine- and Zeeman levels, this is in general a very complicated task, we comment on this in section 1.3. In fact going the other way may also be troublesome, even if one has observed a Feshbach resonance it may be hard to determine which hyperfine and Zeeman levels that are involved in the resonance.

Here we investigate a Feshbach resonance occurring in a toy model. This toy model, being completely useless, serves only one purpose, it may give insight into the underlying mechanisms.

A particle with a two level inner structure is studied (equivalent to spin up and spin down). This particle is being scattered by a square well potential. We add an external field (in this toy model it can be magnetic or something else) and let the two different states respond differently to this field. In addition, particles in different internal states feel a different potential both inside and outside of the square well. The 'interparticle' potential is shown in figure 6.2.

The system is governed by the Hamiltonian

$$\hat{H} = \begin{cases} (-\nabla^2 - V_0)|1\rangle\langle 1| + \Delta|1\rangle\langle 2| + \Delta|2\rangle\langle 1| + (-\nabla^2 - V_0 + V_{\text{in}} + x)|2\rangle\langle 2| & R < a \\ -\nabla^2|1\rangle\langle 1| + (-\nabla^2 + V_{\text{out}})|2\rangle\langle 2| & R > a \end{cases}, \tag{6.4}$$

with Δ as a coupling constant. $|1\rangle$ and $|2\rangle$ are states 1 and 2 respectively. V_{in} is the potential difference between the two internal states inside the potential well, while V_{out} is the potential difference between the two internal states outside the potential well. x is the external field, interacting only with $|2\rangle$. In equation (6.4) and throughout we use $\frac{\hbar^2}{m} = 1$. The Schrödinger equation for this system reads

$$\hat{H}\Psi(R) = \mathbf{E}\Psi(R), \tag{6.5}$$

with

$$\Psi(R) = \begin{pmatrix} \psi_1(R) \\ \psi_2(R) \end{pmatrix}, \tag{6.6}$$

and

$$\mathbf{E} = E \begin{pmatrix} 1 \\ 1 \end{pmatrix}. \tag{6.7}$$

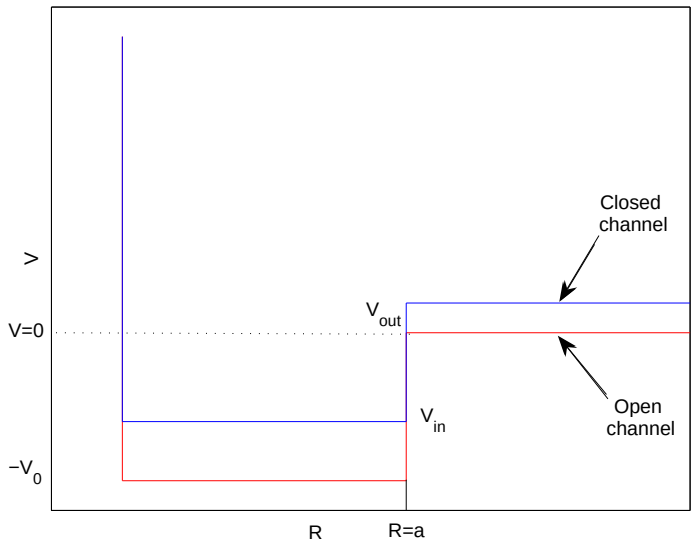

Figure 6.2. *Interparticle potential for the two different particle states introduced in the text (in red and blue). The difference between the potentials are V_{in} for $R < a$ and V_{out} for $R > a$.*

The Schrödinger equation can be written as two coupled second order differential equations

$$-\frac{\mathrm{d}^2\psi_1}{\mathrm{d}R^2} - V_0\psi_1 + \Delta\psi_2 = E\psi_1, \tag{6.8}$$

$$-\frac{\mathrm{d}^2\psi_2}{\mathrm{d}R^2} - V_0\psi_2 + V_{\mathrm{in}}\psi_2 + x\psi_2 + \Delta\psi_1 = E\psi_2. \tag{6.9}$$

The two coupled second order differential equations (for $R < a$) can be written as a set of four first order equations. This is a purely mathematical operation and we define

$$\frac{\mathrm{d}\psi_1}{\mathrm{d}R} \equiv \Phi_1, \tag{6.10}$$

$$\frac{\mathrm{d}\psi_2}{\mathrm{d}R} \equiv \Phi_2. \tag{6.11}$$

We can now rewrite equations (6.8) and (6.9)

$$\frac{\mathrm{d}\Phi_1}{\mathrm{d}R} = -(V_0 + E)\psi_1 + \Delta\psi_2, \tag{6.12}$$

$$\frac{\mathrm{d}\Phi_2}{\mathrm{d}R} = -(V_0 + E)\psi_2 + (V_{\mathrm{in}} + x)\psi_2 + \Delta\psi_1. \tag{6.13}$$

Or in compact matrix notation

$$\frac{\mathrm{d}\tilde{\Psi}}{\mathrm{d}R} = A\tilde{\Psi}, \tag{6.14}$$

with

$$A = \begin{pmatrix} 0 & 0 & 1 & 0 \\ 0 & 0 & 0 & 1 \\ -V_0 - E & \Delta & 0 & 0 \\ \Delta & V_{\text{in}} - V_0 - E + x & 0 & 0 \end{pmatrix}, \qquad \tilde{\Psi}(R) = \begin{pmatrix} \psi_1(R) \\ \psi_2(R) \\ \Phi_1(R) \\ \Phi_2(R) \end{pmatrix}. \tag{6.15}$$

Given the four eigenvalues $\lambda_1, \lambda_2, \lambda_3$ of matrix A and λ_4 along with the corresponding eigenvectors $\mathbf{v}_1, \mathbf{v}_2, \mathbf{v}_3$ and $\mathbf{v}_4$, of matrix A, the solution to equation(6.14) is[1]

$$\tilde{\Psi}(R) = c_1 e^{\lambda_1 R}\mathbf{v}_1 + c_2 e^{\lambda_2 R}\mathbf{v}_2 + c_3 e^{\lambda_3 R}\mathbf{v}_3 + c_4 e^{\lambda_4 R}\mathbf{v}_4. \tag{6.16}$$

with c_1, c_2, c_3 and c_4 as undetermined constants. If one of the eigenvalues λ is complex, the complex conjugate $\bar{\lambda}$ is also among the eigenvalues. For our chosen values of V_0 and V_{in}, matrix A has purely imaginary eigenvalues and eigenvectors. We define $\lambda_1 = i\tau_1$ with eigenvector $\mathbf{v}_1 = i\mathbf{w}_1$ and $\lambda_3 = i\tau_3$ with eigenvector $\mathbf{v}_3 = i\mathbf{w}_3$. This allows us to write the solution as

$$\tilde{\Psi}(R) = c_1 \sin(\tau_1 R)\mathbf{w}_1 + c_2 \cos(\tau_1 R)\mathbf{w}_1 + c_3 \sin(\tau_2 R)\mathbf{w}_2 + c_4 \cos(\tau_2 R)\mathbf{w}_2, \quad R < a. \tag{6.17}$$

We require $\psi_1(0) = \psi_2(0) = 0$ since $V(0) \to \infty$. This determines $c_2 = c_4 = 0$. We must also demand ψ_1 and ψ_2 and their derivatives ψ_1' and ψ_2' to be smooth at $R = a$. To do this we need the solutions for $R > a$. These are easily found from equation (6.4) to be

$$\psi_1(R) = \beta_1 \sin(kR + \delta_0), \qquad k = \sqrt{E}, \tag{6.18}$$

$$\psi_2(R) = \beta_2 e^{-k'R}, \qquad k' = \sqrt{V_{\text{out}} - E}, \tag{6.19}$$

with β_1 and β_2 as undetermined constants. Following the conventions of the previous chapter on scattering theory we put $c_1 = 1$, and find the other constants β_1, β_2, c_3 and δ_0 from the continuity requirements

$$\sin(\tau_1 R)w_{1,1} + c_3 \sin(\tau_2 R)w_{2,1} = \beta_1 \sin(kR + \delta_0), \tag{6.20}$$

$$\tau_1 \cos(\tau_1 R)w_{1,1} + c_3\tau_2 \cos(\tau_2 R)w_{2,1} = \beta_1 k \cos(kR + \delta_0), \tag{6.21}$$

$$\sin(\tau_1 R)w_{1,2} + c_3 \sin(\tau_2 R)w_{2,2} = \beta_2 e^{-k'R}, \tag{6.22}$$

$$\tau_1 \cos(\tau_1 R)w_{1,2} + \tau_2 c_3 \cos(\tau_2 R)w_{2,2} = -\beta_2 k' e^{-k'R}. \tag{6.23}$$

From these equations we have calculate δ_0 and thereby also the scattering length α for different field values (x-values). The result is shown in figure 6.3. We see the signature of a Feshbach resonance as the scattering length approaches $\pm\infty$ for a specific external field value.

6.3 Finding real Feshbach resonances

It would certainly be nice to be able to map out the Feshbach resonances occurring in a real molecule just like we did for the toy model. If possible we could find the B-fields

[1] Here it is assumed that the eigenvectors and eigenvalues are all distinct, this needs not to be the case. See [74] for more details.

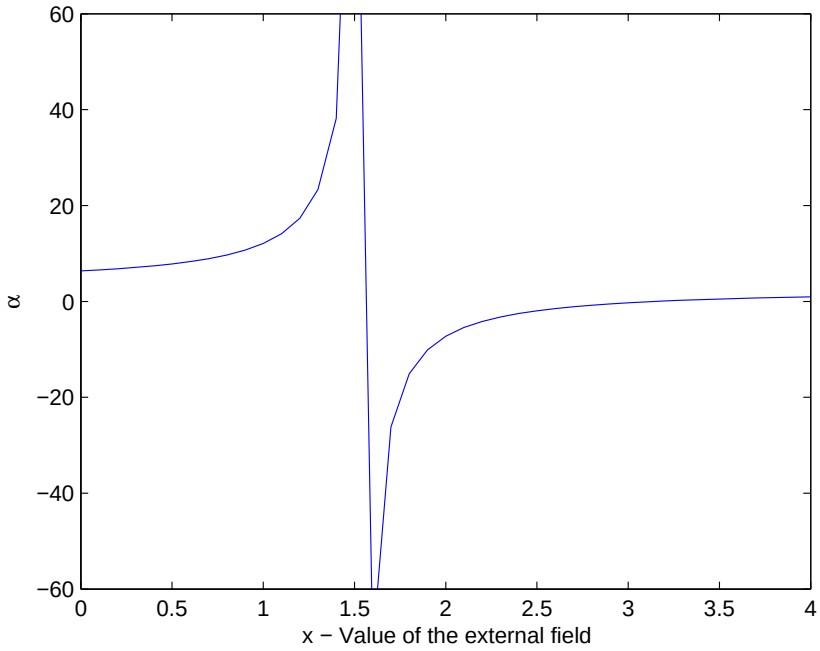

Figure 6.3. *Feshbach resonance in the toy model. The scattering length diverges when a bound state occurs near zero energy. The plot is made using* $V_0 = 125, a = 2, V_{in} = 8, V_{out} = 10, \Delta = 10, E = 0.005$. *Notice that* $\alpha \sim 2$ *away from the resonance. This is a general result, the length of a single square well dictates the scattering length,* $\alpha = a$.

needed to couple different hyperfine levels in for example the $^1\Sigma_g$ and the $^3\Sigma_u$ states in Lithium, we could calculate the probabilities for transferring molecules into the bound level and determine the strength of the interaction. Unfortunately all this is not possible.

Consider the Hamiltonian for a diatomic molecule

$$\hat{H} = \frac{\hbar^2}{2\mu}\nabla^2 + V(R) + \hat{H}_{\text{hf}} + \hat{H}_{\text{z}} + \hat{H}_{\text{other}} \tag{6.24}$$

with hyperfine and Zeeman interactions included. We will not be concerned with the explicit form of $\hat{H}_{\text{hf}}$ and $\hat{H}_{\text{z}}$ here. $\hat{H}_{\text{other}}$ includes other relativistic effects, such as spin-spin and spin-orbit coupling. We make the observation that in going from the continuum of the $^1\Sigma_g^+$ state to a bound molecular state in $^3\Sigma_u$, we have $\Delta S = 1$ and $g \to u$. Thus, the probability for such a process is dictated by the hyperfine Hamiltonian and the matrix element

$$\langle {}^1\Sigma_g^+ | \hat{H}_{\text{hf}} | {}^3\Sigma_u^+ \rangle \equiv F(B, E), \tag{6.25}$$

since all other matrix elements are identically zero. $F(B, E)$ is introduced as a matrix with its elements being the couplings between different hyperfine levels of the two states in question. The couplings are dependent upon energy and the magnetic field strength B. For the $^1\Sigma_g^+$ state there are no hyperfine levels, only vibrational and rotational levels. The matrix element in equation (6.25) is hard to calculate *ab initio* to the order needed since a first order

approach will not suffice. Thus, a theoretical determination of the Feshbach resonances and their properties can not be obtained in this way.

This does not mean that we have no information about Feshbach resonances, but most of this information is found experimentally. Often the experimentalists are guided by more or less accurate calculations on where Feshbach resonances should occur. Experimentally one may then find both the width (strength of the interaction) and the position of the resonance. Experimentalists are then faced with the opposite problem, given a Feshbach resonance for a magnetic field strength B is it possible to find the hyperfine levels involved? This is in general much easier and we have precise information on resonances for several homonuclear molecules such as Li_2 and K_2. These two molecules are perhaps the most investigated because of the relatively low magnetic fields required to reach a resonance.

6.4 Feshbach resonances and Bose-Einstein condensates

We now consider an important occurrence of Feshbach resonances in atomic BEC. Feshbach resonances also has a role in producing molecular BEC, this will be considered further in section 1.5.

An atomic BEC can be described by the Gross-Pitaevskii equation [1] in the $T \to 0$ limit,

$$\left[-\frac{\hbar^2}{2m}\nabla^2 + V(\mathbf{R}) + g|\psi|^2\right]\psi(\mathbf{R}) = E\psi(\mathbf{R}), \tag{6.26}$$

with the coupling constant

$$g \equiv \frac{4\pi\hbar^2 N\alpha}{m}. \tag{6.27}$$

E is the energy of an atom in presence of all the others (this is equal to the chemical potential μ), while $\psi(\mathbf{R})$ can be thought of as the wavefunction of the BEC atoms. The interaction between atoms in this mean field theory is accounted for by the term $g|\psi|^2$. N is the number of atoms, and α is the scattering length. Notice especially how the atomic interactions in the condensate is dependent upon α.

In some alkali atoms the scattering length α may be negative. This causes the atoms in the condensate to be attracted to each other ($g < 0$) and makes it impossible to have many atoms in the condensate. Typical values of N for such a condensate may be around 100. We can analyze why this happens if we introduce a 3D harmonic potential $V(\mathbf{R})$ trapping the atoms

$$V(\mathbf{R}) = \frac{1}{2}m\omega^2 R^2. \tag{6.28}$$

Now we use a variational method to estimate the energy. A gaussian trial wavefunction is introduced (because of the harmonic potential)

$$\psi(R) = Ae^{-R^2/2b^2}, \tag{6.29}$$

b is a variation constant to minimize the energy. Inserted in equation (6.26) this wavefunction predicts an energy [2]

$$E = \frac{3}{4}\hbar\omega\left(\frac{a^2}{b^2} + \frac{b^2}{a^2}\right) + \frac{g}{(2\pi)^{3/2}}\frac{1}{b^3}, \tag{6.30}$$

with $a \equiv \sqrt{\frac{\hbar}{m\omega}}$. By defining $x \equiv a/b$ we can rewrite equation (6.30) as

$$\tilde{E}(x) = \frac{4}{3}\frac{E}{\hbar\omega} = x^{-2} + x^2 + Gx^{-3}, \tag{6.31}$$

with $G \equiv \frac{1.06N\alpha}{a}$. A BEC can only exist as long as equation (6.31) has a minima. Because we have assumed a negative scattering length, $G < 0$. Figure 6.4 shows $\tilde{E}(x)$ for several different G values corresponding to different negative scattering lengths.

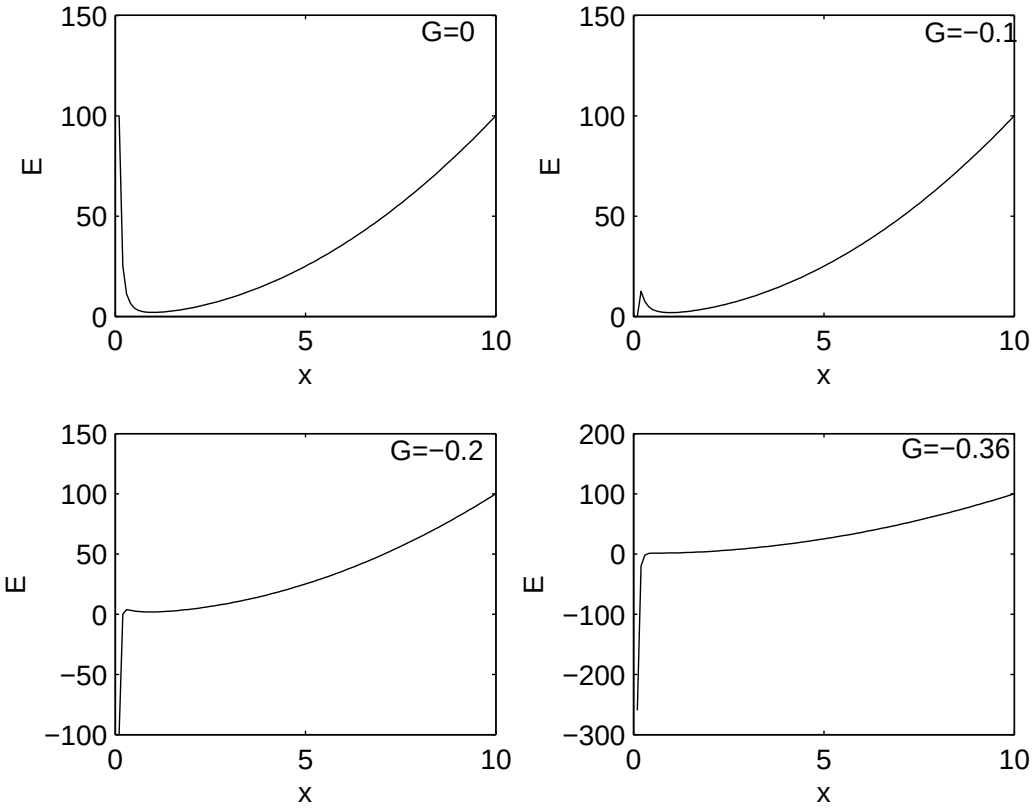

Figure 6.4. *$\tilde{E}$ as a function of x for different values of G. For $G = -0.36$ there is no longer a minima in $\tilde{E}(x)$ and the condensate will implode.*

Figure 6.4 indicates an energy minima that disappears when $G \approx -0.3396$, thus we have

$$N\alpha = -0.3396a. \tag{6.32}$$

For a trap with $a = 2\mu\mathrm{m}$ figure 6.5 shows the maximum number of atoms N in a condensate as a function of α. From figure 6.5 it is seen that equation (6.32) limits the maximum number of atoms in a condensate to a couple of hundred for atoms with large negative scattering lengths. This is too few to make a condensate.

This limitation prevents BEC of atomic species with large negative scattering lengths. Among these are for example $^{85}\mathrm{Rb}$ with a scattering length $\alpha \sim -400a_0$. However, by

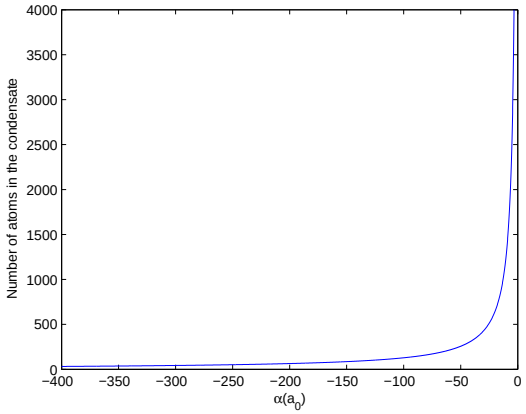

Figure 6.5. *Maximal number of atoms in a condensate with negative scattering length.*

using a magnetic-field induced Feshbach resonance one may tune the scattering length α to a positive value. In this way a condensate can be created also for species with large negative scattering lengths. An example of this can be found in [61].

This level of control offered by the Feshbach resonance means that the scattering length is no longer fixed by the choice of atoms, but can be varied throughout an experiment. This has also led to the investigation of condensates with extremely large positive scattering lengths. With the very strong interactions in such a system, the mean-field Gross-Pitaevskii equation is not expected to hold, and the condensate must be described by other equations.

Several articles [74], [75] also describes condensates where a Feshbach resonance is used to change the scattering length from a positive to a negative value. This causes the condensate to implode. This process along with the effect on the condensate when the scattering length changes sign is studied. This is also the topic for section 1.6

6.5 Production of cold molecules

A Feshbach resonance can also be used to produce cold molecules. This is not merely a theoretical possibility, it has, among others, been reported by Cindy A. Regal *et al.* [63] and by J. Cubizolles *et al.* [64] and is at present time a reality.

This way of producing cold molecules, as with photoassociation, requires pre-cooled atoms from a trap as a starting point. The atomic cooling methods are among those described in chapter 1 and it is typical to use more than one method. However, evaporative cooling is always among these since this is a necessity to reach the low temperatures needed. Previously we noticed how a Feshbach resonance coupled a bound molecular state to the free wavefunction of two colliding atoms. This happens when the bound Zeeman level is tuned into resonance with the continuum state. If we think in terms of the wavefunction introduced in equation (6.1) we enhance the coefficient $f(B, E)$ by putting atom pairs into a stronger superposition of the bound molecular state. In this way we can populate the bound Zeeman level in question. If the magnetic field is further changed (now reversed), lowering the bound level relative to the continuum state, molecules can be trapped in the bound

molecular state. See figure 6.6.

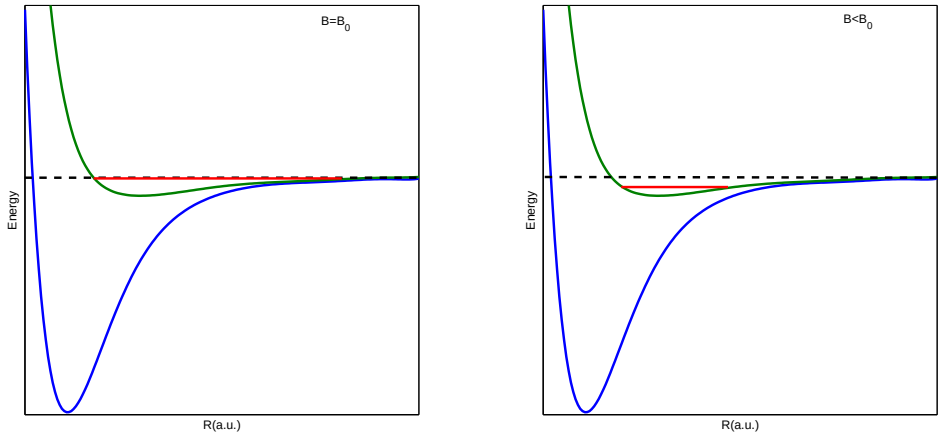

Figure 6.6. *Red line shows position of bound molecular state. To the left at the Feshbach resonance with $B = B_0$. To the right at $B < B_0$ where molecules have been formed as the bound state is lowered. The energy difference shifted by the B-field is exaggerated.*

There is an additional complication arising when producing molecules from fermions. Fermions need to be in different spin states to interact in a way that can be described by the usual low-temperature s-wave theory (the theory outlined in the previous chapter). Because of this, experiments with fermions are carried out using a mixture of atoms in two different spin-states M_F (a so called incoherent mixture). These M_F spin-states are the Zeeman-levels of a hyperfine level F. Fermions have the advantage of forming bosonic molecules with an expected lifetime much longer than for a molecule composed of two bosons. This is a consequence of the Pauli principle and we might say that the Pauli principle makes it harder for two fermions to dissociate into atoms once a molecule is formed. A more detailed explanation will not be given here, the interested reader is referred to [64]. Typical lifetimes for diatomic molecules formed by Feshbach resonance and composed of fermions are from milli seconds to several seconds. The lifetimes are reduced because of atom-molecule and molecule-molecule inelastic collision. Molecules composed of bosons are expected to have very short lifetimes. The problem of short lifetimes is closely related to another limitation we can not overcome when producing molecules this way, namely the population of only highly excited vibrational levels. Very few vibrational levels will be populated and only the highest, there are no chance of reaching the lower vibrational levels. Compared to photoassociation this is a disadvantage.

The effectiveness of the cold molecule production is dependent upon the speed of the magnetic field change (ramp speed). This is often measured in Gauss per second, and typical values may be between 10 and 20 Gauss per second. The production rate as a function of ramp speed approaches a near constant value when the ramp speed is sufficiently slow. Too high ramp speeds yields very few molecules. With optimal ramp speed and other favorable conditions as many as 80% of the atoms [64] may be converted to molecules in one magnetic sweep.

One can also reverse the whole process (going from molecules → atoms) by reversing the ramp speed. When this happens the molecules dissociates and provided there is no trap loss, the number of atoms are again the same as before any molecules were formed.

Compared with other ways of producing cold molecules the Feshbach resonance has perhaps two advantages: 1) The number of molecules produced can be high. 2) The phase-space density can be significantly higher than for other methods (among these, photoassociation). This may also be the reason for Feshbach resonances so often being used to make the molecules in a molecular BEC. To the best of my knowledge the first molecular BEC was made in 2003 by several groups at about the same time. See [69], [70] and [71] and references therein. It is worth noting that Feshbach resonances played a crucial role in the formation of all these condensates.

To make a molecular BEC one needs to start with a collection of fermions cooled to temperatures below the Fermi temperature[2] T_F , in for example [70] it is reported a temperature $T/T_F = 0.17$ for the initial atomic gas. By letting the atoms form molecules (by the use of a Feshbach resonance) adiabatically, conserving entropy, a fraction of the newly formed bosonic molecules should form a condensate. To see this we may consider the ratio between the two temperatures T_C and T_F in an ideal gas, with T_C as the critical temperature for the BEC transition. This is only an estimate, since the degenerate fermion gas is not an ideal gas when it is trapped. Nevertheless, the ratio between the two temperatures in the ideal case is (see appendix D for a derivation of T_C)

$$\frac{T_C}{T_F} = \frac{\frac{1}{k_B} \times 0.527 \times \frac{h^2}{2\pi M} \left(\frac{N}{V}\right)^{2/3}}{\frac{1}{k_B}\frac{h^2}{8m} \left(\frac{3N}{\pi V}\right)^{2/3}} \approx 0.35 \tag{6.33}$$

with $M = 2m$ taken as the mass of the bosons and m as the atomic mass. This indicates $T_C < T_F$, making cooling beyond T_F a necessity for the production of molecular BEC.

6.6 BEC-BCS crossover

In this section a simplified version of the theory for the BCS-BEC crossover is presented. BCS and BEC represents two different phases that can occur in a Fermi gas. With BEC we still mean a Bose-Einstein condensate and in this section BEC indicates a molecular BEC. The BCS phase represents a superfluid phase (flow of a fluid without resistance) that can occur for low temperatures. The transition between these two phases are first described from a qualitative point of view, thereafter a short quantitative presentation is given. The quantitative theory presented is not a state-of-the-art approach, but rather an introduction to the estimation of important parameters. I find the theory of the BCS-BEC crossover physics to be rather unaccessible and a comprehensive derivation of all results have not been possible, instead a number of papers have been referred to. Some knowledge of the BCS theory may be useful.

6.6.1 Qualitative description

The BCS theory describes a superconducting state formed by pair of fermions with opposite wavevectors $\mathbf{k}$ and $-\mathbf{k}$. Such a pair is called a Cooper pair if the two fermions are in different spin states. In superconductors these fermions are electrons, in a Fermi gas they are atoms.

[2]Related to the Fermi energy E_F by $T_F k_B = E_F$. As always k_B is the Boltzmann constant.

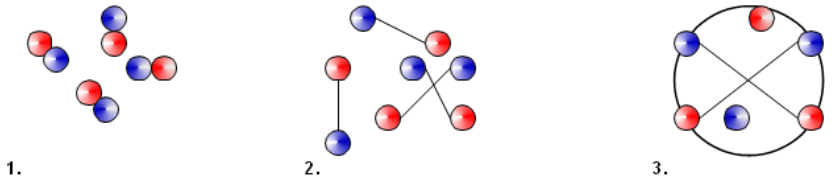

Figure 6.7. *Sketch showing transition from BEC to BCS. 1) Pairs of fermions are strongly interacting and has formed diatomic molecules, α takes moderate positive values. As α is increased towards larger positive values, the molecular binding energy approaches zero. 2) This is an intermediate step where the fermions are strongly interacting. $|\alpha|$ takes large values. 3) Cooper pairs on the Fermi surface (circle) in momentum space. Atoms inside the circle represents fermions in the Fermi sea in equilibrium with the Cooper pairs. α is negative. For 1), 2) and 3) the blue and red are used to indicate fermions in different spin states.*

We consider a dilute homogenous Fermi gas that has been cooled and a diatomic molecular BEC has been formed. Depending on the strength of the interaction between the fermions (in the diatomic molecule) it is possible to go from the BEC to the BCS regime. If the interactions between the fermions are strong the fermions can pair and produce an integer spin particle. This integer spin particle (diatomic molecule) can be seen as a composite boson, making it possible to achieve BEC. One must remember that although this is referred to as the strong interaction regime, the interactions between the bosons themselves are weak. As the interactions between the fermions are increased the diatomic molecules becomes more loosely bound before the molecule dissociates into a strongly interacting pair, before becoming Cooper pairs. During this sequence the scattering length has gone from positive to plus infinity to minus infinity and ends up at a moderate negative value. See also figure 6.7.

The Cooper pairing mechanism needs to be considered further. Cooper himself imagined two fermions outside the Fermi sea with equal and opposite momentum. It may be shown that forming a Cooper pair is energetically favorable for such a pair, in other words, the energy of the two fermions is *less* than $2E_F$ with E_F as the Fermi energy. This can at least partly be explained by the Pauli exclusion principle which makes it impossible for the fermion pair to occupy momentum states with $|\mathbf{k}| \leq |\mathbf{k}_F|$. $\mathbf{k}_F$ is the Fermi wavevector related to the Fermi energy by $E_F = \frac{\hbar^2 k_F^2}{2m}$.

The above discussion is of course inadequate since more than one pair of fermions will form Cooper pairs. In fact one expect Cooper pairing to continue until an equilibrium point is reached. This occurs when it is no longer favorable to form Cooper pairs, because the Fermi sea is disturbed so that momentum states $|\mathbf{k}| < |\mathbf{k}_F|$ is accessible. The solution to this many body problem is the so called BCS state.

6.6.2 Quantitative description ($T = 0$)

Unfortunately we will have to limit ourselves in the presentation of the BCS-theory as given below. The analysis is only valid at $T = 0$, it has proven hard to obtain accurate theories for finite temperatures and this is a work that continues. The theory presented below is the so called NSR theory, based on a work by Nozires and Schmitt-Rink [66]. The key equations are presented together with an investigation of the two limits, BEC and BCS.

We have the very central gap equation as in BCS, introducing the gap parameter Δ_k as the energy needed to brake up a Cooper pair with wavevectors $\mathbf{k}$ and $-\mathbf{k}$

$$\Delta_k = -\sum_{\mathbf{k}'} U_{kk'} \frac{\Delta_{k'}}{2E'_k}. \tag{6.34}$$

Here we have $E_k = \sqrt{\xi^2 + \Delta_k}$, $\xi = \epsilon_k - \mu$ and $\epsilon_k = \frac{\hbar^2 k^2}{2m}$. $U_{kk'}$ is the attractive potential for scattering of fermions with $\mathbf{k}'$ and $-\mathbf{k}'$ to $\mathbf{k}$ and $-\mathbf{k}$. μ is the chemical potential.

The total number of fermions in both states (red an blue in figure 6.7) are given by

$$\langle N_{\text{tot}} \rangle = \sum_{\mathbf{k}} \left(1 - \frac{\xi_k}{E_k}\right). \tag{6.35}$$

To solve equation 6.34 for Δ_k it is standard to argue that $U_{kk'}$ is constant (independent of k and k'). Then it follows that Δ_k is also a constant, $\Delta_k = \Delta$ and equation (6.34) takes the form

$$-\frac{1}{U} = \sum_{\mathbf{k}} \frac{1}{2E_k}. \tag{6.36}$$

This equation is problematic when dealing with atomic systems since it turns out to diverge! When using BCS theory on superconductors this divergence is avoided because the Debye energy sets an upper limit to the energy. The Debye energy comes into play in superconductors because it is the phonons that interacts with the electrons and make them form Cooper pairs. Since there are no equivalent restriction on the energy for an atomic system this divergence is a serious problem that requires some kind of a normalization procedure. See for example [67]. The result is however the modified gap equation

$$-\frac{m}{4\pi\hbar^2\alpha} = \frac{1}{V}\sum_{\mathbf{k}} \left(\frac{1}{2E_k} - \frac{1}{2\epsilon_k}\right), \tag{6.37}$$

with m as the fermion mass, V as the volume and α still as the s-wave scattering length. For the cross-over regime (between BEC and BCS) we have to solve equations (6.37) and (6.35) simultaneously to obtain Δ and μ. These really are the central parameters, μ as the chemical potential and Δ has the interpretation of excitation gap, the smallest possible energy that can create a hole in the superfluid in the BCS limit. Here we only look at the BCS and BEC limits and do not treat the crossover, however it should be noted that the crossover behavior is smooth. It is possible to find μ and Δ analytically also in the crossover regime by the use of elliptic integrals [68]. In the BEC limit one can find [68]

$$\mu = -\left(\frac{1}{k_F\alpha}\right)^2 E_F, \qquad \Delta = E_F\sqrt{\frac{16}{3\pi}\frac{1}{k_F\alpha}}. \tag{6.38}$$

And in the BCS limit [68]

$$\mu = E_F, \qquad \Delta = e^{\frac{-\pi}{k_F|\alpha|}} E_F. \tag{6.39}$$

The BCS limit where $\mu = E_F$ can be used if the interaction energy is small compared to the Fermi energy, since the equilibrium between Cooper pairs and fermions then occurs for

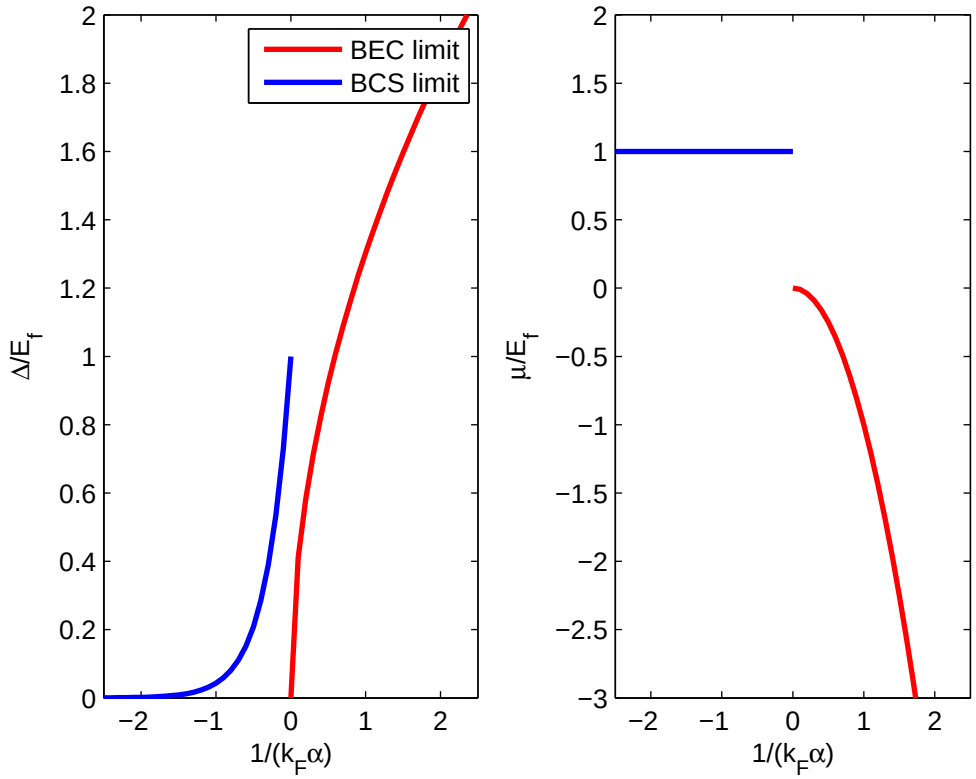

Figure 6.8. *μ and Δ in the BEC and BCS limit for a Fermi gas at $T = 0$. BEC regime to the left of each figure and BCS regime to the right. By tuning the scattering length α a smooth transition between the two regimes occurs. We see the chemical potential μ changes from fermionic ($\mu > 0$) to bosonic ($\mu < 0$).*

approximately $\mu = E_F$. From figure 6.8 we also find $\mu = 0$ as for an ideal Bose gas if α approaches infinity and the fermions are strongly interacting.

The gap parameter Δ is a very central parameter in the BCS theory, as it represents the minimum energy needed to break a Cooper pair. Δ is expected to be 0 at the superfluid phase transition temperature T_C. This is because it is at this temperature it starts to be energetically favorable to form Cooper pairs. The gap parameter increases toward the value it takes at $T = 0$, $\Delta(T = 0)$ depends on the phase transition temperature as [68]

$$\Delta(T = 0) = \frac{3.528}{2} k T_C. \tag{6.40}$$

From figure 6.8 we find $T_C = 0$ when $\alpha \to 0$, this seems reasonable since there are no attraction between the fermions in this limit, thus making the formation of Cooper pairs not favorable.

Generally we see that T_C increases with the interaction, still BCS transition temperatures can be extremely small and are therefore often not experimentally attainable.

If we think of a transition from BCS to BEC this happens when interactions between the

fermions forming Cooper pairs increases, along with Δ to the point where $\Delta = E_F$. We are then back in the cross over regime.

At present the transition between the two regimes are simulated using a Monte Carlo approach [76] [77]. This represents the best theoretical simulations possible in 2006. The pitfall of the NSR theory presented above is mainly due to the oversimplified description of the system which includes only two-particle correlations.

6.7 Hyperfine structure

Knowledge of the hyperfine and hyperfine Zeeman levels in a diatomic molecules plays a crucial role to Feshbach resonances. Couplings between the continuum and magnetically tuned Zeeman levels gives broad Feshbach resonances. In this section we have calculated the hyperfine structure of the shallow $^3\Sigma_u^+$ state in the $^6Li_2$ molecule. We only investigate the $N = 0$ rotational level[3] of the highest excited vibrational level of the $^3\Sigma_u^+$ state. Other rotational levels will not contribute at the ultracold temperatures we are interested in. This might be seen since the energy of the different rotational levels are given by

$$E_N = B_{\text{rot}} N(N+1) \tag{6.41}$$

with rotational constant

$$B_{\text{rot}} = \frac{\hbar^2}{2I}. \tag{6.42}$$

I is the moment of inertia for the molecule. To see just how improbable an excitation to a higher rotational level is we may calculate the ratio between the two probabilities $P(N=1)$ and $P(N=0)$ for populating the $N = 0$ and $N = 1$ respectively

$$\frac{P(N=1)}{P(N=0)} = e^{-\frac{2B_{\text{rot}}}{kT}} \simeq e^{-10^5}. \tag{6.43}$$

The temperature used is $T = 10^{-6}$K, while the rotational constant is found to be $B_{\text{rot}} = 0.204\text{cm}^{-1}$. This value is calculated from the expectation value

$$\langle B_{\text{rot}} \rangle = \frac{\hbar^2}{2\mu} \left\langle \psi_v \left| \frac{1}{R^2} \right| \psi_v \right\rangle, \tag{6.44}$$

with the constant $\frac{\hbar^2}{2\mu}$ found to be 19.9357cm^{-1} for $^6Li_2$. ψ_v is the vibrational wavefunction of the highest vibrational level in the $^3\Sigma_u^+$ state. The highest vibrational level is the only one with relevance to Feshbach resonances. It is only the Zeeman levels of this vibrational level that can be tuned into resonance with the continuum. Lower laying vibrational levels do not have enough energy to make such a resonance possible.

Generally the hyperfine Hamiltonian for a diatomic molecule with one nuclear spin or for a homonuclear molecule may be written [78]

$$\hat{H}_{\text{hf}} = 2g_I\mu_0\mu_N \hat{\mathbf{I}} \cdot \sum_i \frac{\hat{\mathbf{r}}_i \times \hat{\mathbf{p}}_i}{r_i^3} + 2g_I\mu_0\mu_N \sum_i \left[\frac{3(\hat{\mathbf{I}} \cdot \hat{\mathbf{r}}_i)(\hat{\mathbf{s}}_i \cdot \hat{\mathbf{r}}_i)}{r_i^5} - \frac{\hat{\mathbf{I}} \cdot \hat{\mathbf{s}}_i}{r_i^3} \right] + 2g_I\mu_0\mu_N \sum_i \frac{8\pi}{3} \hat{\mathbf{s}}_i \cdot \hat{\mathbf{I}} \delta(\hat{\mathbf{r}}_i) \tag{6.45}$$

[3] We denote by **N** the total angular momentum of the molecule, composed of the orbital angular momentum **L** of the electrons and the angular momentum of the rotation of the nuclei

with g_I as the nuclear g factor and μ_N as the nuclear magneton. The summation is taken over the electrons. In the ${}^3\Sigma_u^+$ state both atoms have orbital angular momentum equal to zero, thus the hyperfine Hamiltonian can be written

$$\hat{H}_{\text{hf}} = b_F \hat{\mathbf{S}} \cdot \hat{\mathbf{I}} \tag{6.46}$$

with $I \in \{0, 1, 2\}$ and $S \in \{0, 1\}$. $S = 0$ corresponds to the singlet ground state that has no hyperfine structure and is thus without interest in this context. The possible values thay I can attain are found from adding the nuclear spins of the two Lithium atoms with $\mathbf{i}_1 = \mathbf{i}_2 = 1/2$. The constant b_F is the Fermi contact parameter

$$b_F = \frac{16\pi}{3} g_I \mu_0 \mu_N \frac{1}{\Sigma} \left\langle q\Lambda\Sigma \middle| \sum_i \delta(\mathbf{r}_i) s_{iz} \middle| q\Lambda\Sigma \right\rangle. \tag{6.47}$$

Most of the symbols used are obvious or defined before, perhaps with exception of q that is used as a label to separate different electronic states with the same Λ and Σ quantum numbers. The less obvious is perhaps how to calculate b_F, it can of course not be done analytically but must be done numerically. Luckily the MultiMod program that finds the electronic state wavefunctions for us, shortly described in an earlier chapter, also calculates four hyperfine parameters [78], among them, b_F.

From the Hamiltonian H_{hf} in equation (6.46) we can find the the different hyperfine levels in terms of b_f. To see this we write

$$\hat{\mathbf{F}} = \hat{\mathbf{J}} + \hat{\mathbf{I}} = \hat{\mathbf{S}} + \hat{\mathbf{I}}, \tag{6.48}$$

with $\mathbf{J} = \mathbf{N} + \mathbf{S}$, assuming $N = 0$. Here we have used $\mathbf{l}_1 = \mathbf{l}_2 = 0$. Thus we may write

$$\hat{H}_{\text{hf}} = \frac{b_f}{2}(\hat{\mathbf{F}}^2 - \hat{\mathbf{S}}^2 - \hat{\mathbf{I}}^2) \tag{6.49}$$

Working in a basis with F, I and S as good quantum numbers we find

$$H_{\text{hf}} = \frac{b_f}{2}(F(F+1) - S(S+1) - I(I+1)). \tag{6.50}$$

The hyperfine structure without any applied B-field is shown in figure 6.9. When calculating the hyperfine structure in figure 6.9 we have used a b_f value obtained from averaging over the relevant vibrational wavefunction

$$b_f = \int_0^\infty \psi_v(R) b_f(R) \psi_v(R) \mathrm{d}R \tag{6.51}$$

with $b_f(R)$ as a function obtained when running MultiMOD for a series of different R values in the range $3 \leq R \leq 20$. The integration is performed with Simpsons method and gives $b_f = 44.63\text{MHz}$[4].

When an external magnetic field is applied the degeneracy in the M_F quantum number is lifted and the Zeeman effect appears. This effect is described by the Hamilton operator

$$\hat{H}_{\text{z}} = \hat{\mu} \cdot \mathbf{B} \tag{6.52}$$

[4]Energy is sometimes measured in Hz, this makes sense since $f = \frac{E}{h}$ with E as energy, h is the Planck constant. More specific we have $1\text{eV} = 2.41797 \cdot 10^8 \text{MHz}$.

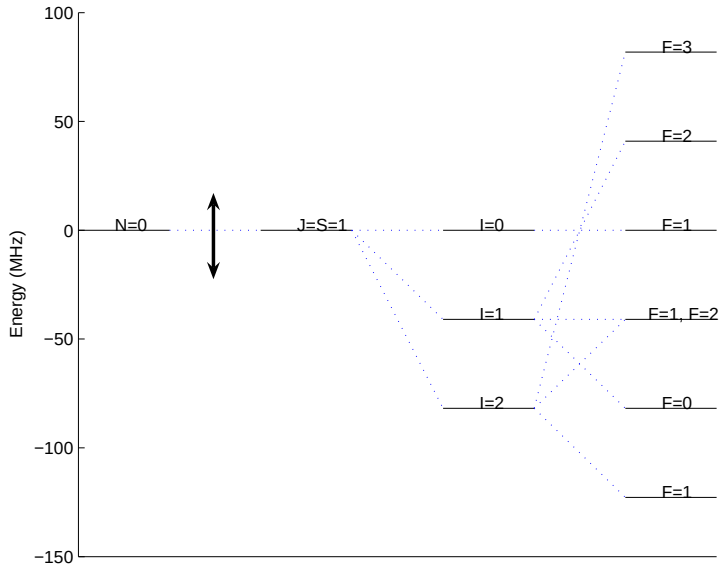

Figure 6.9. *Hyperfine structure in the ${}^3\Sigma_u^+$ electronic state with $N = 0$ and $J = S = 1$. The up-down-arrow is inserted because we can not determine the exact position of the hyperfine structure relative to the rotational level. Unfortunately there is one higher-order spin-orbit type of parameter that is unknown. This unknown parameter causes a constant shift in energy. The width of the hyperfine structure is however correct.*

with

$$\hat{\mu} = -g_J \mu_B \hat{\mathbf{J}} + g_I \mu_N \hat{\mathbf{I}}. \tag{6.53}$$

When an external magnetic field is applied the F quantum number is no longer a good quantum number. Finding the energy levels of the different Zeeman levels is therefore not an easy task, and as often before a numerical calculation is necessary. The writing of the code to do this has already been done some twenty years ago by my supervisor Leif Veseth. His program has been used to find the positions for the different Zeeman levels with different magnetic field strengths.

6.7.1 Zeeman levels at different magnetic fields

In this section we present diagrams for the Zeeman structure as it is found for different magnetic field strengths. To separate the different Zeeman levels from each other we use different colors for different M_F quantum numbers. We have not been able to calculate the exact energy of each Zeeman level because we can not precisely determine the position of the $J = 1$ level. However, this shifts the whole Zeeman structure either up or down as a whole, and do not influence the position of the levels relative to each other. This is indicated with an up-down-arrow in the diagrams (figures 6.11-6.15).

The figures show several interesting features. From figure 6.11, at the low field of only 1 Gauss[5], one sees that with this field strength it still makes good sense to group the Zeeman levels according to their F-quantum number. Although F is not a good quantum number in an external magnetic field, the perturbation is still small at $B = 1\text{G}$. This situation changes rapidly as the magnetic field is increased and already by $B = 10\text{G}$ Zeeman levels from different F quantum numbers start to overlap. When increasing the magnetic field further we see from figure 6.12 that the Zeeman levels start to cling together in three different groups, each group sharing the same M_J quantum number. This behavior is even clearer in figure 6.13, where the 27 Zeeman levels form three bands (of about 150MHz). From the last figure 6.14 where $B = 10000\text{G}$ we see that the Zeeman levels are no longer grouped together and we have quite an unpredictable behavior. This is typical for an atomic or molecular system at very high magnetic fields. In figure 6.10 this behavior is summarized

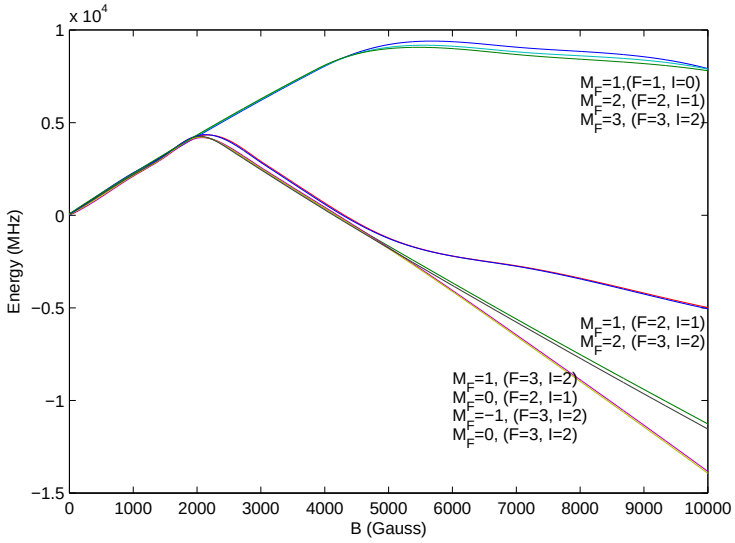

Figure 6.10. *The 9 Zeeman levels with $M_J = 1$ as a function of magnetic field strength. We observe a linear behavior below $\simeq 2000\text{G}$. For $B > 2000\text{G}$ the behavior is hard to predict and the linear relationship between energy and magnetic field is completely lost. This is due to interactions among several rotational levels.*

Most closely related to the Feshbach resonances is perhaps figure 6.14 showing the Zeeman levels at $B = 1000\text{G}$. It is known that there exists a broad Feshbach resonance in $^6\text{Li}_2$ at a magnetic field of $B = 810\text{G}$ [79]. This must mean that the $M_J = 1$ band seen in figure 6.14 at a magnetic field of $B = 810\text{G}$ is lifted into resonance with the open channel. To be more specific we remember that the interaction coupling the open channel to the closed channel must conserve the total M_F quantum number. In other words, the Zeeman levels that can interact with two atoms in M_F states M_{F_1} and M_{F_2} are those with quantum number $M_F = M_{F_1} + M_{F_2}$. The known ^6Li resonance at 810G occurs between atoms in $|F_1, M_{F_1}\rangle = |1/2, 1/2\rangle$ and $|F_2, M_{F_2}\rangle = |1/2, -1/2\rangle$ hyperfine states. Thus, only $M_F = 0$ in the $M_J = 1$ band will have the possibility to couple to the open channel. There exists two

[5] $1\text{T} = 10000\text{G}$(auss).

almost degenerate $M_F = 0$ values (a difference of a couple of MHz) in the $M_J = 1$ band. These two levels appears as one in figure 6.14.

Although we might predict the structure and relative positions of the Zeeman hyperfine levels with certainty, we have problems predicting at what magnetic fields Feshbach resonances occur. There are two reasons for this uncertainty: 1) We have an undetermined constant in our calculations that may shift the Zeeman structure up or down. 2) The position of the last bound vibrational level is uncertain. Problem 1) involves a second order spin-orbit type of parameter that is unknown, this parameter can not be calculated *ab initio* and is not experimentally known. Problem 2) however has been given attention, and our calculated position is expected to be reliable. If we assume the Zeeman splitting to be dominant at the Feshbach resonance of $B = 810\mathrm{G}$ we may neglect our undetermined constant and say that we are tuning the $M_F = 0$ levels approximately $1800\mathrm{MHz}$ since this is the $M_F = 0$ position at $810\mathrm{G}$. This would indicate the last bound vibrational level to be shifted approximately $0.0600\mathrm{cm}^{-1}$ from the continuum limit. After extending our calculated values for the $^3\Sigma_u^+$ electronic state with the usual long range van der Waals potential (we use the same C_6, C_8, C_{10} as in the previous chapter) and polishing the potential curve, we found the topmost vibrational level to be positioned at $560.91\mathrm{cm}^{-1}$ above the minima at the equilibrium distance of the electronic state. This vibrational level is then situated approximately $0.6228\mathrm{cm}^{-1}$ *below* the dissociation limit. This is a factor 10 from our rough estimate made above. It may be that our undetermined constant is of this size, or it could be that there exists yet another vibrational level in the $^3\Sigma_u^+$ electronic state. Also, with the *ab initio* methods used to calculate the interatomic potential curve and thereafter the vibrational levels, we can probably not predict vibrational levels with the accuracy needed here. My claim is therefore that the results are in agreement with the experimental findings, but too inaccurate to predict the exact magnetic field needed to observe a Feshbach resonance.

We thus have to conclude that it is hard to predict the magnetic field needed to find a Feshbach resonance from theoretically *ab initio* calculations. Our calculations do however show that it is very plausible that there exists a Feshbach resonance around $800\mathrm{G}$ in $^6\mathrm{Li}_2$. Together theoretical considerations and observed resonances may yield information about the molecule. Examples of this may be the position of the last bound vibrational level or the unknown spin-orbit parameter.

For all Zeeman levels calculated we have used $g_I\mu_N = 0$ (see equation (6.53). Since $g_I\mu_N$ is approximately 10^{-4} less than $g_S\mu_B$ it does not really matter whether it is included or not. This has been verified also for the stronger fields of $B = 1000\mathrm{G}$ and $B = 10000\mathrm{G}$ where this effect changes the energy levels with approximately $1\mathrm{MHz}$ and $10\mathrm{MHz}$ respectively.

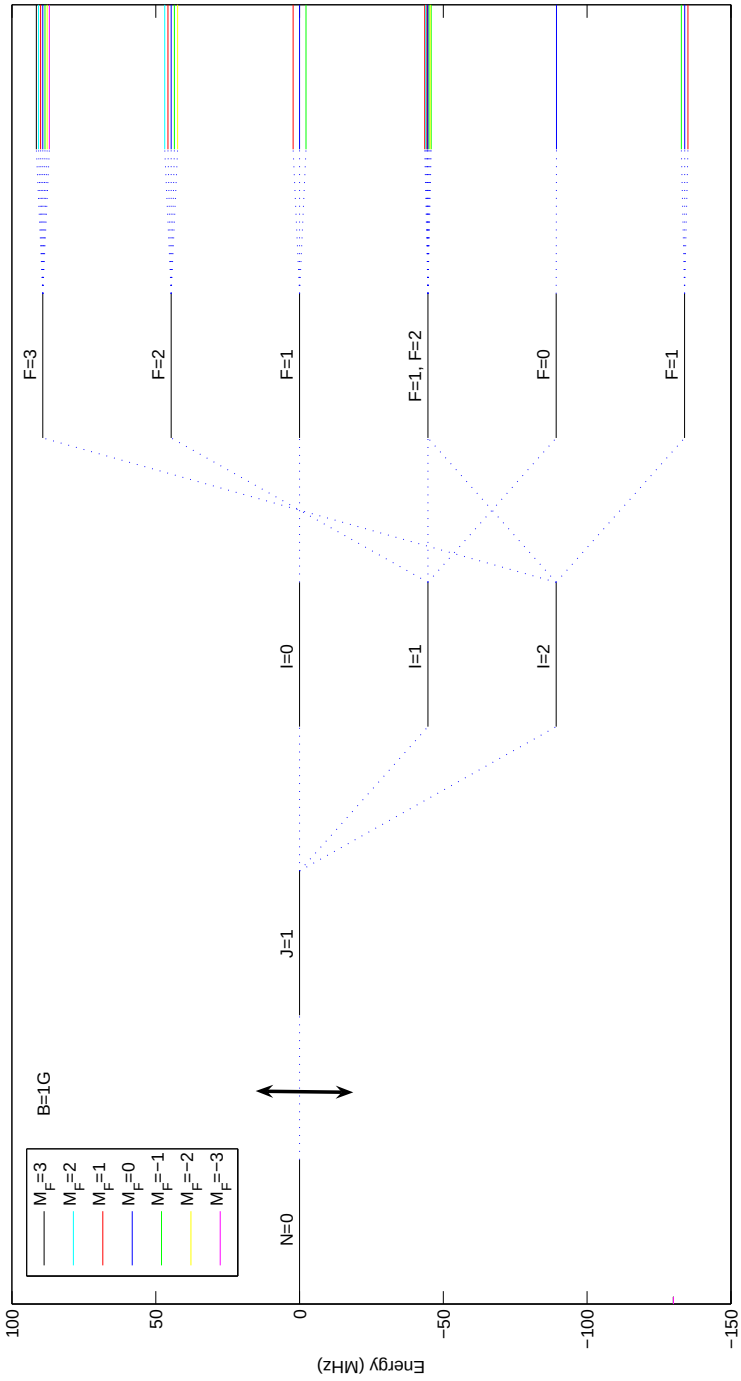

Figure 6.11. *Zeeman levels with $B = 1\mathrm{G}$. See the text for further discussions and explanations.*

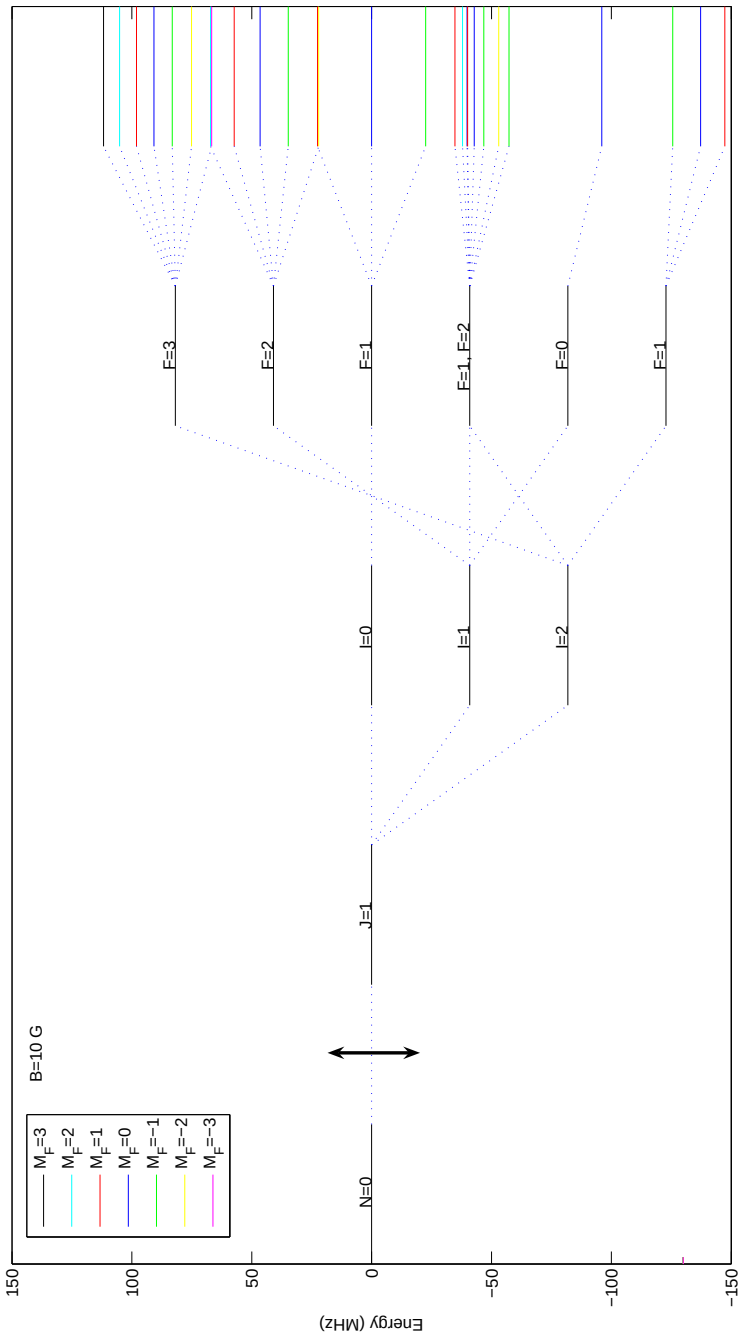

Figure 6.12. *Zeeman levels with $B = 10\mathrm{G}$. See the text for further discussions and explanations.*

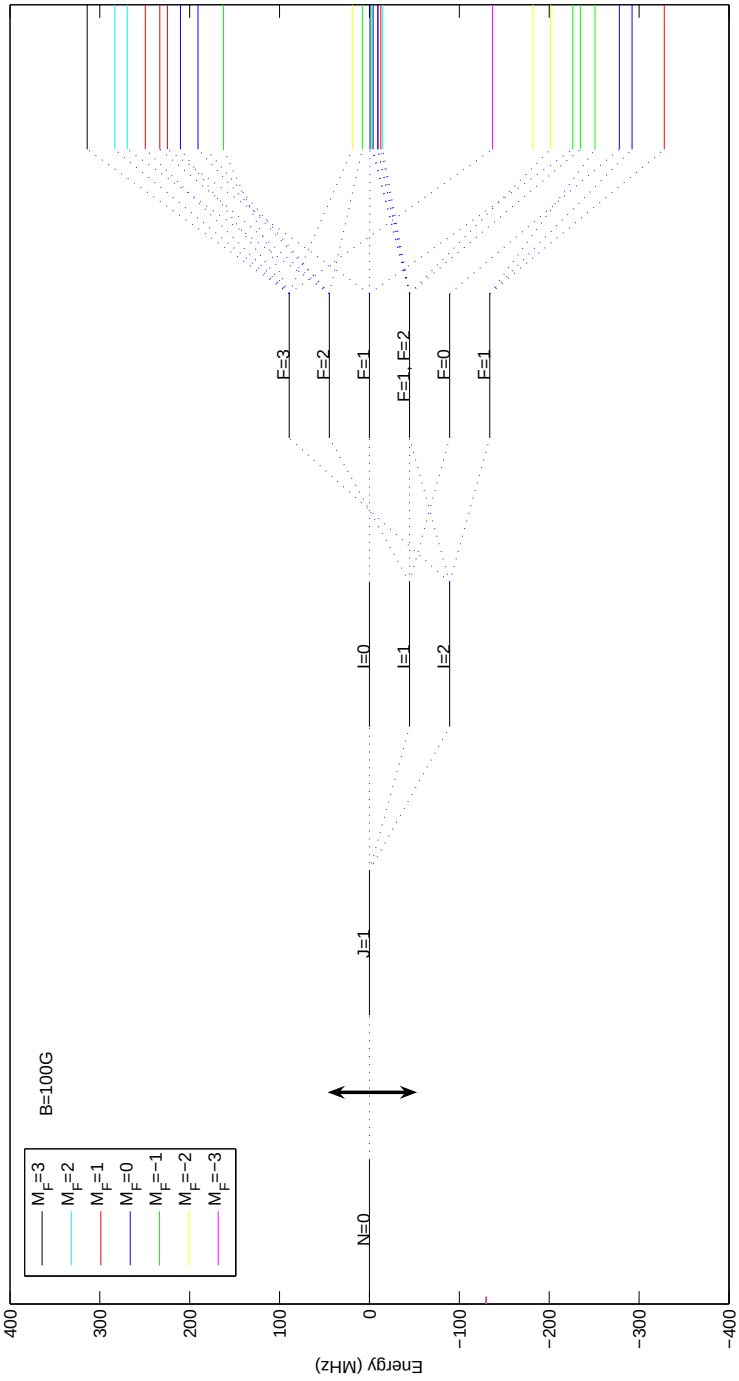

Figure 6.13. *Zeeman levels with $B = 100\mathrm{G}$. See the text for further discussion and explanations.*

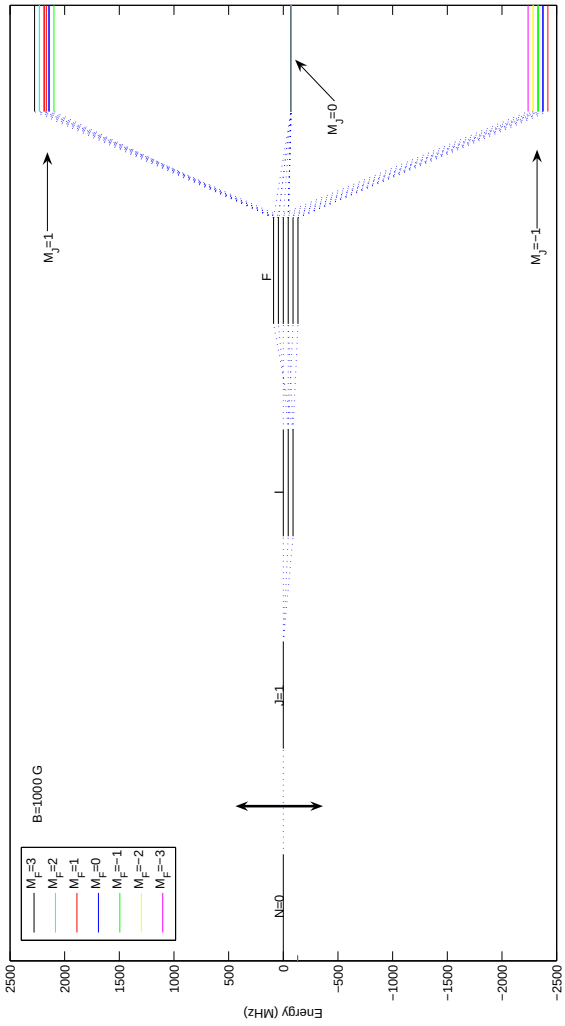

Figure 6.14. *Zeeman levels with* $B = 1000\mathrm{G}$. *See the text for further discussion and explanations.*

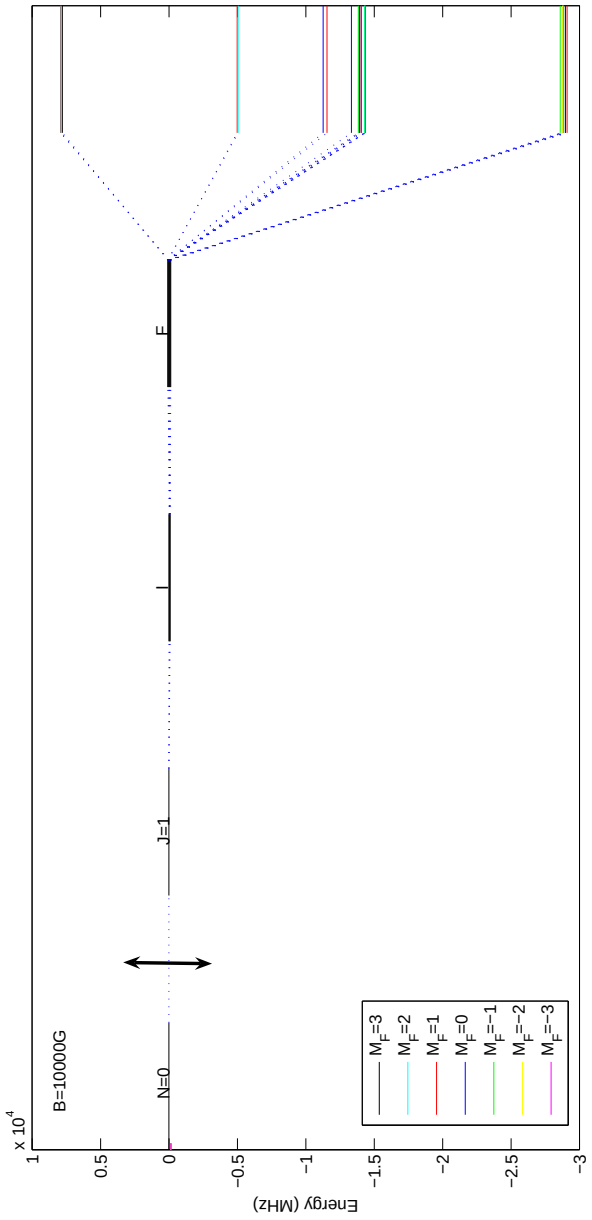

Figure 6.15. *Zeeman levels with* $B = 10000\mathrm{G}$. *See the text for further discussion and explanations.*

Appendix A

Examples of input-files

A.1 Input file for the Hartree-Fock program

Below an input file used in the Hartree-Fock calculations for Li_2. This file specifies the basis used in the calculations.

```
INTEGRALS Li2-basis
3.0,3.0,03.00,40,6,-1
```

Comment: Each line specifies a Slater orbital with the information needed in following order $k, 0.0, , , , m_l, n, l$.

```
4.40,0.0,,,0,1,0
2.30,0.0,,,0,1,0
1.90,0.0,,,0,2,0
0.90,0.0,,,0,2,0
0.50,0.0,,,0,3,0
0.90,0.0,,,0,2,1
0.60,0.0,,,0,2,1
0.35,0.0,,,0,3,1
4.40,0.0,,,0,-1,0
2.30,0.0,,,0,-1,0
1.90,0.0,,,0,-2,0
0.90,0.0,,,0,-2,0
0.50,0.0,,,0,-3,0
0.90,0.0,,,0,-2,1
0.60,0.0,,,0,-2,1
0.35,0.0,,,0,-3,1
1.40,0.0,,,1,2,1
0.90,0.0,,,1,2,1
0.50,0.0,,,1,3,1
0.40,0.0,,,1,3,2
1.40,0.0,,,1,-2,1
0.90,0.0,,,1,-2,1
0.50,0.0,,,1,-3,1
0.40,0.0,,,1,-3,2
1.40,0.0,,,-1,2,1
```

```
0.90,0.0,,,-1,2,1
0.50,0.0,,,-1,3,1
0.40,0.0,,,-1,3,2
1.40,0.0,,,-1,-2,1
0.90,0.0,,,-1,-2,1
0.50,0.0,,,-1,-3,1
0.40,0.0,,,-1,-3,2
0.90,0.0,,,2,3,2
0.50,0.0,,,2,3,2
0.90,0.0,,,2,-3,2
0.50,0.0,,,2,-3,2
0.90,0.0,,,-2,3,2
0.50,0.0,,,-2,3,2
0.90,0.0,,,-2,-3,2
0.50,0.0,,,-2,-3,2
SCF
TEST FOR Li CLOSED SHELL
5,16,8,8,4,4,3.000
3,0,0,0,0,0
500,0,0,0.0
3,0,0,0,0
0.17,0.90,0.0,0.0,0.0,0.0,0.0,0.0,
0.17,0.90,0.0,0.0,0.0,0.0,0.0,0.0
0.19,0.80,0.0,0.0,0.0,0.0,0.0,0.0,
-0.19,-0.80,0.0,0.0,0.0,0.0,0.0,0.0
0.0,-0.19,0.00,0.80,0.0,0.0,0.0,0.0,
0.0,-0.19,0.00,0.80,0.0,0.0,0.0,0.0
TRANSFORM
40,40,1
2.0,2.0,2.0,0.0,0.0,0.0,0.0,0.0,0.0,0.0,0.0,0.0,0.0,0.0,0.0,0.0,0.0,0.0
0.0,0.0,0.0,0.0,0.0,0.0,0.0,0.0,0.0
0.0,0.0,0.0,0.0,0.0,0.0,0.0,0.0,0.0
0.0,0.0,0.0,0.0
0.0,0.0,0.0,0.0
PROPERTY 40
1,2,3,4,5,6,7,8,9,10,11,12,13,14,15,16
17,18,19,20,21,22,23,24
25,26,27,28,29,30,31,32
33,34,35,36
37,38,39,40
1
03.00
PROPERTY-PACKAGE
Li-basis
40,6,0
9,7,38,39,40,6
2.0,2.0,2.0,0.0,0.0,0.0,0.0,0.0,0.0,0.0,0.0,0.0,0.0,0.0,0.0,0.0,0.0,0.0
```

```
0.0,0.0,0.0,0.0,0.0,0.0,0.0,0.0
0.0,0.0,0.0,0.0,0.0,0.0,0.0,0.0
0.0,0.0,0.0,0.0
0.0,0.0,0.0,0.0
FINISH
```

A.2 MultiMOD input file

Below is an input file used to calculate energies for the $^1\Sigma_g^+$ electronic state. This input file has the correct number of symmetries and orbitals to correspond to the Hartree-Fock program input file of section A.1

```
Li gr.tilst.
     NS=  5     NO= 40   NSYM=  2  NKONF= 17   NAUG=  0   IPOT=  0   IHYP=  1
  GIFAK= 0.8219     ASPO1= 5.84280    ASPO2= -14.3139     ZNL= 03.0
  IPRI1=  1  IPRI2=  1  IPRI3= -7 NBOUND= 18  NAUGP=  0
   S2UT=  1   SPUT=  1
 NRO:
  1  2  3  4  5 17 25 18 26  6  7  9 08 10 19 27 20 28 11 21 29 22 30
 12 13 14 15 16 23 31 24 32 33 34 35 36 37 38 39 40
 NBP:
 16  8  8  4  4
 NHO:
  1  1  1  1  1  1  1  1  1  1  1  1  1  1  1  2  2  2  2  2  2  2
  2  3  3  3  3  3  3  3  3  4  4  4  4  5  5  5  5
 MHO:
  1  2  3  4  5  6  7  8  9 10 11 12 13 14 15 16
 17 18 19 20 21 22 23 24
 25 26 27 28 29 30 31 32
 33 34 35 36
 37 38 39 40
 FI:
   1   2   3   4   5  17  25  18  26   6   7   8   9  10  19  27  20  28  (nro)
  11  11  11  00  00  00  00  00  00  00  00  00  00  00  00  00  00  00
  11  11  10  00  01  00  00  00  00  00  00  00
  11  11  00  00  00  00  00  10  01  00
  11  11  00  00  00  10  01  00
  11  11  10  00  00  00  00  00  00  00  01  00
  11  11  00  10  00  00  00  00  00  01  00
  11  11  00  00  00  00  00  00  00  11
  11  11  00  00  10  00  00  00  00  00  01  00
  11  11  10  00  00  00  00  00  00  00  00  00  01
  11  11  00  11  00
  11  11  00  00  11
  11  11  00  10  00  00  00  00  00  00  00  01  00
  11  11  00  00  00  10  00  00  00  00  00  00  00  00  01  00
  11  11  00  00  00  00  10  00  00  00  00  00  00  00  01  00
```

```
  11  11  00  00  00  00  00  00  00  00  11  00
  11  11  00  00  10  00  00  00  00  00  00  01
  11  11  00  00  00  00  00  00  00  10  00  01  00
L,M:
  0  0  1  1  1 -1  2  2  2 -2
 POTNUC=  1.7821
 NEVLIM=  0.02
 DIALIM=  0.05
GRENER1= -14.884033 GRENER2= -14.931550 GRENER3= -000.000
   ETAT= 0.00
  ETATO= 0.01        ETATSI= 0.0
```

A.3 Vibra input file

Vibra input file corresponding to the two potential curves $^1\Sigma_u^+$ and $^1\Sigma_g^+$. This input file also calculates the Franck-Condon factors between the different vibrational level in the two electronic states.

```
   NP= 4  NOP=28 NOBS=27 NMOR= 0NFREK= 0
 RMIN=3.500RMAX=30.00   H=0.0050   MM=90
 FACT=0.179376
VBUNN= 1.655     RE=5.500
 RMIN=1.798RMAX=15.66   H=0.0050   MM=90  NOP=28
 INPUT POT. Li2, 1sigmau-tilstand
  3.40   3.290
  3.90   2.495
  4.20   2.169
  4.70   1.844
  5.05   1.717
  5.20   1.689
  5.50   1.653
  5.70   1.663
  6.00   1.665
  6.50   1.719
  7.00   1.805
  8.00   1.979
  9.00   2.193
  10.0   2.379
  11.0   2.512
  12.0   2.610
  13.0   2.670
  14.0   2.714
  15.0   2.739
  16.0   2.753
  17.0   2.758
  19.0   2.778
  20.0   2.807
```

```
  22.0   2.837
  25.0   2.847
  26.0   2.857
  28.0   2.877
  30.0   2.897
VBUNN= 0.00      RE=5.050
 RMIN=1.693RMAX=15.66   H=0.0050   MM=90  NOP=47
 INPUT POT. Li2, grund tilstand
  3.20   1.366
  3.50   0.842
  3.70   0.429
  4.00   0.248
  4.20   0.157
  4.40   0.107
  4.60   0.049
  4.80   0.014
  5.00   0.00998
  5.05   0.0000
  5.20   0.0136
  5.50   0.0681
  5.70   0.121
  5.90   0.182
  6.10   0.250
  6.40   0.280
  6.70   0.414
  6.90   0.464
  7.10   0.540
  7.30   0.552
  7.50   0.614
  7.80   0.645
  8.00   0.693
  8.20   0.709
  8.50   0.777
  9.00   0.848
  9.50   0.891
  10.0   0.930
  10.5   0.970
  11.0   1.009
  11.5   1.004
  12.0   1.013
  12.5   1.024
  13.0   1.033
  14.0   1.047
  15.0   1.056
  16.0   1.060
  17.0   1.063
  18.0   1.066
```

```
  19.0   1.070
  20.0   1.071
  22.0   1.070
  24.0   1.070
  26.0   1.070
  28.0   1.070
  29.0   1.070
  30.0   1.070
INPUT R-AVH. GAMMAVERDIER
  3.50   1.0
  4.50   1.0
  5.00   1.0
  5.50   1.0
  6.00   1.0
  6.50   1.0
  7.00   1.0
  7.50   1.0
  8.00   1.0
  9.00   1.0
  10.0   1.0
  10.5   1.0
  11.0   1.0
  12.0   1.0
  12.5   1.0
  13.0   1.0
  13.5   1.0
  14.0   1.0
  14.5   1.0
  15.0   1.0
  16.0   1.0
  18.0   1.0
  20.0   1.0
  22.0   1.0
  25.0   1.0
  27.0   1.0
  30.0   1.0
```

Appendix B

Tunneling program

The programs developed to calculate tunneling probabilities are listed below. Version 1.0 is the most general program that calculates continuum $\rightarrow$ potential barrier $\rightarrow$ continuum for any barrier.

Version 2.0 is specialized for the problem at hand, including rotation and not using continuum solutions on both sides of the potential.

Both programs are commented extensively, together with the text in chapter 3 also describing them, this should be sufficient for understanding the code.

Version 1.0

```
% Programmet regner ut tunneleringssannsynligheten for en partikkel,med
% et villkårlig potensial. Vi antar kontiniuum --> kontiuniuum. Potensialet
% leses inn fra fil med formatet kolonne 1: x verdier, kolonne 2:
% potensialbarriæren. Filnavn skal være potensialet uten efternavn. Det er
% ikke antatt at E<V, da et generelt potensiale typisk ikke vil oppfylle
% dette i enkelte områder.

clear all
load potensialet
x=potensialet(1:end,1);
V=potensialet(1:end,2);

m=(6.9*9.38e6)/2; %partikkelmassen i elektronvolt per c^2
%E=0.001 %partikkelens inkommende energi i eV.
%E=4.975e-005;
%**************************************************************************
% Denne koden skal kun tas med hvis potensialet oppgis i a.u.
for i=1 : length(x)
    x(i)=x(i)*5.29e-02;
    V(i)=V(i)-2.89;
    %plot(x,V)
    % Kontrollplot for at potensialet oppfører seg OK.
end
```

```
%************************************************************************

xstart=x(1); %Minste x-verdi for potensial
xslutt=x(length(x)); %Største x-verdi for potensial
n=round((xslutt-xstart)*5000); %antall oppdelinger, kan justeres etter
% behov.
w=(xslutt-xstart)/n; % Bredden på hver oppdeling, holdes konstant her.
xi=[xstart:w:xslutt];
yi=interp1(x,V,xi,'cubic'); % interpolasjon i pot kurven. Bruker spline
% eller cubic. Spline gir en svært glatt kurve, men kan produserer tull
%hvis noen punkter ligger mye nærmere hverandre enn andre. Kan også bruke
%linear.
%hold on
%plot(xi,yi);
Vi=zeros(1,(length(yi))); for i=1 : (length(yi)-1)
    Vi(i)=0.5*(yi(i)+yi(i+1)); %Midtpunkt V for hver bar
end
%************************************************************************
hbar=197.3; %hstrek (egentlig hstrek*c, c'ene skal kanselere "masse c'ene")
kB=8.617e-05; % Brukes for å lage plott av sannsynlighet mot temp.
%************************************************************************
T1=ones(1,400); %Koden mellom stjernestreken over og under skal kun med
E1=ones(1,400); % hvis det ønskes sannsynligheter for en mengde energier.
for h=1:400     % For å plotte
 E1(1,h)=0.001+0.001*(h-1);
 E=E1(1,h)*kB;
%************************************************************************
% alpha og k vil med disse enhentene måles i inverse nm
k=sqrt(2*m*E/hbar^2); alpha=ones(1,length(Vi)); for i=1: length(Vi)
    if(Vi(i)>E) % Tester på områder hvor E<V
      alpha(i)=sqrt((2*m*(Vi(i)-E))/hbar^2);
    else
      alpha(i)=sqrt((2*m*(E-Vi(i)))/hbar^2);
    end
end
%************************************************************************
% Oppretter riktig antall K matriser (tilsvarer K' - en faktor e^(alpha w)
% tas ut så vi ikke får avrundingsfeil til null inne i produktet
% Dette gjøres for hvert "tunneleringssegment -områder E<V.
K=ones(2,2,n); for j=1 : n
    if(Vi(j)>E)
       faktor=2*alpha(j)*w;
       K(1,1,j)=0.5*(1+exp(-faktor));
       K(1,2,j)=(-0.5/(alpha(j)))*(1-exp(-faktor));
       K(2,1,j)=(-alpha(j)/2)*(1-exp(-faktor));
       K(2,2,j)=K(1,1,j);
       if(alpha(j)<0.001)
```

```
          K(1,1,j)=cosh(alpha(j)*w);
          K(1,2,j)=-w-(w^3*(alpha(j))^2)/6-(w^5*(alpha(j))^4)/120;
          K(2,1,j)=-alpha(j)*sinh(alpha(j)*w);
          K(2,2,j)=cosh(alpha(j)*w);
       end
    else
       faktor=alpha(j)*w;
       K(1,1,j)=cos(faktor);
       K(1,2,j)=-(1/alpha(j))*sin(faktor);
       K(2,1,j)=alpha(j)*sin(faktor);
       K(2,2,j)=cos(faktor);
    end
end
% Regner ut produktet av matrisene
for j=1 : (n-1)
   K(:,:,j+1)=K(:,:,j)*K(:,:,j+1);
end
P=K(1,1,n);
Q=K(1,2,n);
R=K(2,1,n);
S=K(2,2,n);
% Konverterer mellom T og T', må regne ut summen over alphaene tatt ut
% tidligere
sumalpha=0; for i=1: n
    if(Vi(i)>E)
      sumalpha=sumalpha+alpha(i);
    end
end G=w*sumalpha;
% Regn ut T og T'
Tmark=4/((P+S)^2+(Q*k-R/k)^2); T=exp(-2*G)*Tmark;
%R=1-T
%*************************************************************************
% Alt under her kan tas med hvis for løkka i linje 46 er aktiv.
T1(1,h)=T; end plot(E1(1,:), T1(1,:))
xlabel('Energy (eV)') %Endres etter behov.
ylabel('Transmission coefficient')
```

Version 2.0

```
% Programmet regner ut tunneleringssannsynligheten for en partikkel,
%  gjennom  et villkårlig potensial. Versjon 2.0 som gjengitt under
% er laget kun med tanke på det spesielle problemet med tunnelering
% gjennom potensialbarriæren for 1PI_u tilstanden i Li2. Potensialet leses
% inn fra fila "potensialet" (både for område I og II)

clear all
```

```
load potensialet
x=potensialet(1:end,1);
V=potensialet(1:end,2);
%************************************************************************
% Denne koden skal kun tas med hvis kjerneavstanden oppgis i a.u.
for i=1 : length(x)
    x(i)=x(i)*5.29e-02;
    V(i)=V(i)-2.89;
    %plot(x,V) % Kontrollplot for at potensialet oppfører seg OK.
end
%************************************************************************
J=; % sett J verdi
xslutt=x(length(x));
xstart=x(1); %Minste x-verdi for potensial
n=round((xslutt-xstart)*100); %antall oppdelinger i region I og II,
%kan justeres etter behov.
w=(xslutt-xstart)/n; % Bredden på hver oppdeling, holdes konstant her (nm).
xi=[xstart:w:xslutt];
yi1=interp1(x,V,xi,'cubic'); % interpolasjon i pot kurven. Bruker 'spline'
% eller 'cubic'. Spline gir en svært glatt kurve, men kan produserer tull
%(ses ved et å begå et plott) hvis noen punkter ligger mye nærmere
% hverandre enn andre. Kan også bruke 'linear'.
%hold on
%plot(xi,yi);

if (J~=0)
    R=sqrt(43*J*(J+1)); % Regner ut minste R hvor ang.mom ledd tas med.
    if(R<15)
        R=15
    end
    n2=round((R-15)/w)+n; %antall oppdelinger totalt (i reg I, II og III)
    yi=ones(1,n2+1);
    hva=length(yi1);
    for i=1: hva
      R=xstart+(i-1)*w;
      yi(1,i)=yi1(1,i) + (0.0043*J*(J+1))/R^2;
    end
    jl=1;
    for i=hva+1 : length(yi)
      R=15.1+w*(jl);
      yi(1,i)=(0.0043*J*(J+1))/R^2;
      jl=jl+1;
    end
else
yi=yi1;
n2=n;
end
```

```
Vi=zeros(1,n2);
for i=1 : n2
    Vi(1,i)=0.5*(yi(1,i)+yi(1,i+1));
end

%*********************************************************************
m= ; %Sett partikkelmassen i elektronvolt per c^2
hbar=197.3; %hstrek (egentlig hstrek*c, c'ene skal kanselere "masse c'ene")
kB=8.617e-5; %Boltzmann konstant (eV per Kelvin)
E1=zeros(1,10);
T1=zeros(1,10);
for h=1: 10
  E1(1,h)=0.1+(h-1)*0.1;
  E=E1(1,h)*kB;
  %E=4.9577e-005; %partikkelens inkommende energi i elektronvolt
  % alpha og k vil med disse enhentene måles i inverse nm
%*************************************************************
  xpos=xstart;
  t=0;
  while xpos<(8*5.29e-2)
    q=1;
    v=sqrt((2*(E-V(1,q)))/m);
    v=v*(3e8);
    t=t+(w*1e-9)/v;
    q=q+1;
    xpos=xpos+w;
  end
%*************************************************************
  k1=sqrt(2*m*E/hbar^2);
  alpha=ones(1,length(Vi));
  for i=1: length(Vi)
   if(Vi(i)>E) % Tester på områder hvor E>V
      alpha(1,i)=sqrt((2*m*(Vi(i)-E))/hbar^2);
   else
      alpha(1,i)=sqrt((2*m*(E-Vi(i)))/hbar^2);
   end
  end
  k=alpha(1,1);
%*********************************************************************
% Oppretter riktig antall K matriser (tilsvarer K' - en faktor e^(alpha w)
% tas ut så vi ikke får avrundingsfeil til null inne i produktet.
%  Dette gjøres for hvert "tunneleringssegment" (områder
% E<VO.)
  K=ones(2,2,n2);
  for j=1 : n2
    if(Vi(j)>E)
       faktor=2*alpha(j)*w;
```

```
        K(1,1,j)=0.5*(1+exp(-faktor));
        K(1,2,j)=(-0.5/(alpha(j)))*(1-exp(-faktor));
        K(2,1,j)=(-alpha(j)/2)*(1-exp(-faktor));
        K(2,2,j)=K(1,1,j);
    else
        faktor=alpha(j)*w;
        K(1,1,j)=cos(faktor);
        K(1,2,j)=-(1/alpha(j))*sin(faktor);
        K(2,1,j)=alpha(j)*sin(faktor);
        K(2,2,j)=cos(faktor);
    end
    if(alpha(j)<0.01)
    K(1,2,j)=w+(w^3*alpha(j)^2)/6;
    end
end
% Regner ut produktet av matrisene
for j=1 : (n2-1)
   K(:,:,j+1)=K(:,:,j)*K(:,:,j+1);
end
P=K(1,1,n2);
Q=K(1,2,n2);
R=K(2,1,n2);
S=K(2,2,n2);
% Konverterer mellom T og T' må regne ut summen over alphaene tatt ut
% tidligere
sumalpha=0;
for i=1: n2
    if(Vi(i)>E)
      sumalpha=sumalpha+alpha(i);
    end
end
G=w*sumalpha;
% Regn ut T og T'
%Tmark=(2*k^2)/(k^2*S^2+R^2+k^2*P^2+k^4*Q^2+cos(2*k*(L2+n2*w))
%*(k^2*S^2-k^2*P^2-R^2+k^4*Q^2)-2*sin(2*k*(L2+n2*w))*(k^2*P*Q+k*R*S));
%Tmark=(2*k1^2)/(k^2*S^2+R^2+k1^2*P^2+k^2*k1^2*Q^2+cos(2*k*(L2+n3*w))*
%(k^2*S^2+k^2*k1^2*Q^2-k1^2*P^2-R^2)-2*sin(2*k*(L2+n3*w))*
%(k1^2*k*P*Q+k*R*S));
%Tmark=(2*k1^2)/(k^2*S^2+R^2+k1^2*P^2+k^2*k1^2*Q^2+cos(2*k*(L2+n2*w))*(k^2*
%S^2-k1^2*P^2-R^2+k^2*k1^2*Q^2)-2*sin(2*k*(L2+n2*w))*(k1^2*k*P*Q+k*R*S));
Tmark=(4*k^2*k1)/(k*((P*k+S*k1)^2+(Q*k*k1-R)^2));
%T1(1,h)=exp(-2*G)*Tmark;
T=exp(-2*G)*Tmark;
T1(1,h)=T;
%R=1-T1(1,i);
end
plot(E1(1,:),T1(1,:),'r')
```

```
xlabel('Energy(eV)')
ylabel('Tunnleing probability')
% RESTEN AV KODEN GIR POSISJONER TIL VIB.NIV.
%hold on
%y=[1,0];
%Energier=[0.4,184,345,465,509,614,676.4,809.4,839.5,1001.3,1038.1,1139.4];
%for i=1:12
%  x=ones(1,2);
%   x(1,1)=Energier(1,i)/8068.3;
%   x(1,2)=Energier(1,i)/8068.3;
%   plot(x,y);
%end
```

Appendix C

Calculating scattering lengths

C.1 Theory- explicit form of M and W matrices

In this appendix we give the exact form of the M matrices defined in chapter 1 in equation (5.85). To do this we need the spherical Bessel and Neumann functions, $j_l(\rho)$ and $n_l(\rho)$ respectively with $\rho = kR$. For programming purposes we introduce polynomials $P_l(x)$ and $Q_l(x)$ such that

$$j_l(\rho) = P_l(1/\rho)\sin\rho + Q_l(1/\rho)\cos\rho, \tag{C.1}$$
$$n_l(\rho) = Q_l(1/\rho)\sin\rho - P_l(1/\rho)\cos\rho, \tag{C.2}$$

and similarly for the derivatives

$$j_l'(\rho) = \bar{P}_l(1/\rho)\sin\rho + \bar{Q}_l(1/\rho)\cos\rho, \tag{C.3}$$
$$n_l'(\rho) = \bar{Q}_l(1/\rho)\sin\rho - \bar{P}_l(1/\rho)\cos\rho. \tag{C.4}$$

In each segment j (see chapter 5 section 5.6) we have a new $\rho_j = \alpha_j R_j$. Some of these may be complex, in these cases α_j is purely imaginary and so is ρ_j. Equations C.1, C.2, C.3 and C.4 must then be modified. Thus, we introduce new polynomials (with tilde above) for the complex case, in analogy with what was done for real ρ_j values,

$$j_l(i\rho) = i^l\left(\tilde{P}_l(1/\rho)\sinh\rho + \tilde{Q}_l(1/\rho)\cosh\rho\right), \tag{C.5}$$
$$n_l(i\rho) = i^{l+1}\left(\tilde{Q}_l(1/\rho)\sinh\rho + \tilde{P}_l(1/\rho)\cosh\rho\right). \tag{C.6}$$

Similarly for the derivatives

$$j_l'(i\rho) = i^{l-1}\left(\tilde{\bar{P}}_l(1/\rho)\sinh\rho + \tilde{\bar{Q}}_l(1/\rho)\cosh\rho\right), \tag{C.7}$$
$$n_l'(i\rho) = i^{l}\left(\tilde{\bar{Q}}_l(1/\rho)\sinh\rho + \tilde{\bar{P}}_l(1/\rho)\cosh\rho\right). \tag{C.8}$$

In the case of real and imaginary α_j (corresponding to real and imaginary ρ_j) we have M matrices $\left(x \equiv \frac{1}{\alpha_j R}$ for real α, and $x \equiv \frac{1}{|\alpha_j| R}$ for complex $\alpha\right)$

$$M_l(R,\alpha) = \sin\alpha R \begin{pmatrix} P_l(x) & Q_l(x) \\ \alpha\bar{P}_l(x) & \alpha\bar{Q}_l(x) \end{pmatrix} + \cos\alpha R \begin{pmatrix} Q_l(x) & -P_l(x) \\ \alpha\bar{Q}_l(x) & -\alpha\bar{P}_l(x) \end{pmatrix}, \tag{C.9}$$

$$M_l(R,i|\alpha|) = i^l \left[\sinh|\alpha|R \begin{pmatrix} \tilde{P}_l(x) & i\tilde{Q}_l(x) \\ |\alpha|\bar{\tilde{P}}_l(x) & i|\alpha|\bar{\tilde{Q}}_l(x) \end{pmatrix} + \cosh|\alpha|R \begin{pmatrix} \tilde{Q}_l(x) & i\tilde{P}_l(x) \\ |\alpha|\bar{\tilde{Q}}_l(x) & i|\alpha|\bar{\tilde{P}}_l(x) \end{pmatrix} \right], \tag{C.10}$$

and the inverse matrices with the same convention on x

$$M_l^{-1}(R,\alpha) = \alpha R^2 \left[\sin\alpha R \begin{pmatrix} \alpha\bar{Q}_l(x) & -Q_l(x) \\ -\alpha\bar{P}_l(x) & P_l(x) \end{pmatrix} + \cos\alpha R \begin{pmatrix} -\alpha\bar{P}_l(x) & P_l(x) \\ -\alpha\bar{Q}_l(x) & Q_l(x) \end{pmatrix} \right], \tag{C.11}$$

$$M_l^{-1}(R,i|\alpha|) = i^{l+1}|\alpha|R^2 \left[\sinh|\alpha|R \begin{pmatrix} i|\alpha|\bar{\tilde{Q}}_l(x) & -i\tilde{Q}_l(x) \\ -|\alpha|\bar{\tilde{P}}_l(x) & \tilde{P}_l(x) \end{pmatrix} + \cosh|\alpha|R \begin{pmatrix} i|\alpha|\bar{\tilde{P}}_l(x) & -i\tilde{P}_l(x) \\ -|\alpha|\bar{\tilde{Q}}_l(x) & \tilde{Q}_l(x) \end{pmatrix} \right]. \tag{C.12}$$

The W matrix introduced in chapter 1 equation (5.86) consists of products of M and M^{-1} matrices

$$W \equiv M_l^{-1}(Nb,k)M_l(Nb,\alpha_N)M_l^{-1}((N-1)b,\alpha_N)\dots M_l(2b,\alpha_2)M_l^{-1}(b,\alpha_2)M_l(b,\alpha_1), \tag{C.13}$$

W is completely defined in terms of this product of 2×2 matrices, but one may define

$$K_l(\alpha_j) \equiv M_l(jb,\alpha_j)M_l^{-1}((j-1)b,\alpha_j). \tag{C.14}$$

This gives one K matrix per α and we can write for W,

$$W = M_l^{-1}(Nb,k)\left(\prod_{j=N}^{2} K_{j,l}\right) M_l(b,\alpha_1). \tag{C.15}$$

This reduces the number of matrices to be multiplied by approximately one half, assuming we use the K matrix elements below instead of M matrices. Again we must separate between imaginary α and real α. We use $x \equiv 1/jb\alpha, y \equiv 1/(j-1)b\alpha, \theta \equiv \alpha b$.

$$K_{j,l}(\alpha)_{11} = (j-1)^2b^2\alpha^2[(-P_l(x)\bar{P}_l(y) - Q_l(x)\bar{Q}_l(y))\sin\theta + (P_l(x)\bar{Q}_l(y) - Q_l(x)\bar{P}_l(y))\cos\theta], \tag{C.16}$$

$$K_{j,l}(\alpha)_{12} = (j-1)^2b^2\alpha[(P_l(x)P_l(y) + Q_l(x)Q_l(y))\sin\theta + (-P_l(x)Q_l(y) + Q_l(x)P_l(y))\cos\theta], \tag{C.17}$$

$$K_{j,l}(\alpha)_{21} = (j-1)^2b^2\alpha^3[(-\bar{P}_l(x)\bar{P}_l(y) + \bar{Q}_l(x)\bar{Q}_l(y))\sin\theta + (\bar{P}_l(x)\bar{Q}_l(y) - \bar{Q}_l(x)\bar{P}_l(y))\cos\theta], \tag{C.18}$$

$$K_{j,l}(\alpha)_{22} = (j-1)^2b^2\alpha^2[(\bar{P}_l(x)P_l(y) + \bar{Q}_l(x)Q_l(y))\sin\theta + (-\bar{P}_l(x)Q_l(y) + \bar{Q}_l(x)P_l(y))\cos\theta]. \tag{C.19}$$

And for the case of complex α

$$K_{j,l}(i|\alpha|)_{11} = (-1)^l(j-1)^2b^2|\alpha|^2[(-\tilde{P}_l(x)\bar{\tilde{P}}_l(y) + \tilde{Q}_l(x)\bar{\tilde{Q}}_l(y))\sinh\theta + (\tilde{P}_l(x)\bar{\tilde{Q}}_l(y) - \tilde{Q}_l(x)\bar{\tilde{P}}_l(y))\cosh\theta], \tag{C.20}$$

$$K_{j,l}(i|\alpha|)_{12} = (-1)^l(j-1)^2b^2|\alpha|[(\bar{\tilde{P}}_l(x)\bar{\tilde{P}}_l(y) - \bar{\tilde{Q}}_l(x)\bar{\tilde{Q}}_l(y))\sinh\theta + (-\bar{\tilde{P}}_l(x)\bar{\tilde{Q}}_l(y) + \bar{\tilde{Q}}_l(x)\bar{\tilde{P}}_l(y))\cosh\theta], \tag{C.21}$$

$$K_{j,l}(i|\alpha|)_{21} = (-1)^l(j-1)^2b^2|\alpha|^3[(-\bar{\tilde{P}}_l(x)\tilde{P}_l(y) + \bar{\tilde{Q}}_l(x)\tilde{Q}_l(y))\sinh\theta + (\bar{\tilde{P}}_l(x)\tilde{Q}_l(y) - \bar{\tilde{Q}}_l(x)\bar{P}_l(y))\cosh\theta], \tag{C.22}$$

$$K_{j,l}(i|\alpha|)_{22} = (-1)^l(j-1)^2b^2|\alpha|^2[(\tilde{P}_l(x)\tilde{P}_l(y) - \tilde{Q}_l(x)\tilde{Q}_l(y))\sinh\theta + (-\tilde{P}_l(x)\tilde{Q}_l(y) + \tilde{Q}_l(x)\tilde{P}_l(y))\cosh\theta]. \tag{C.23}$$

The eight polynomials $P, \bar{P}, \tilde{P}, \bar{\tilde{P}}, Q, \bar{Q}, \tilde{Q}, \bar{\tilde{Q}}$ are defined in equations (C.1)-(C.8), and we may use the recurrence relation for the spherical Bessel and Neumann functions to find the following recurrence relations for the eight polynomials

$$P_l(x) = (2l-1)xP_{l-1}(x) - P_{l-2}(x), \tag{C.24}$$

$$\bar{P}_l(x) = \frac{lP_{l-1}(x) - (l+1)P_{l+1}}{2l+1}. \tag{C.25}$$

Similarly recurrence relations are found for Q_l and $\bar{Q}_l$ (the recurrence relations are the same, but the polynomials are different since P_0 and P_1 do not equal Q_0 and Q_1).

The relation between $P_l(x)$ and $\tilde{P}_l(x)$ and between $Q_l(x)$ and $\tilde{Q}_l(x)$ follows from the substitution $\rho \to i|\rho|$

$$\tilde{P}_l(x) = i^{1-l}P_l(-ix), \tag{C.26}$$

$$\tilde{Q}_l(x) = i^{-l}Q_l(-ix). \tag{C.27}$$

The corresponding recurrence relations in the complex case

$$\tilde{P}_l(x) = -(2l-1)x\tilde{P}_{l-1}(x) + \tilde{P}_{l-2}(x), \tag{C.28}$$

$$\bar{\tilde{P}}_l(x) = \frac{l\tilde{P}_{l-1}(x) + (l+1)\tilde{P}_{l+1}(x)}{2l+1}. \tag{C.29}$$

Notice that equation (C.29) is different from the formula in [51], it is a quite obvious misprint in their equation 28 confirmed by calculations. To generate polynomials with the recurrence relations we use

$$P_0(x) = x, \qquad Q_0(x) = 0, \tag{C.30}$$

$$P_1(x) = x^2, \qquad Q_1(x) = -x. \tag{C.31}$$

These polynomials are found by matching to the respective spherical Bessel and Neumann functions. For our purpose $l = 0$ is the most interesting, therefore we list the 6 not previously listed $l = 0$ polynomials (P_0 and Q_0 are in equation (C.30))

$$\bar{P}_0(x) = -x^2, \qquad \bar{Q}_0(x) = x, \tag{C.32}$$

$$\tilde{P}_0(x) = x, \qquad \tilde{Q}_0(x) = 0, \tag{C.33}$$

$$\bar{\tilde{P}}_0(x) = -x^2, \qquad \bar{\tilde{Q}}_0(x) = x. \tag{C.34}$$

C.2 Computer code

The program used to calculate the scattering lengths is listed here. The program has few comments, but based on the information given in chapter 1 section 1.6 and previously in this appendix, it should be possible to understand.

Eight functions are used to calculate the different polynomials needed. These are listed after the main program.

```
%alle lengder i a0
clear all
%*****************************************************************
%                   INNDATA OG KONSTANTER                        *
%*****************************************************************
l=0; %partial bølge
N=400000; % Antall segmenter
a=500; % Oppgi cutoff R
mu=2.82199495545; %redusert masse
E=2.721e-7; % måles i eV
hbar=197.3*18.8726; %hstrek i eVa_0
FAC=(2*mu)/hbar^2;
k=sqrt(2*mu*E)/hbar;
middelpot=ones(1,N);
middx=ones(1,N);
alpha=zeros(1,N);
%*****************************************************************
%     LES INN POTENIALET - INTERPOLASJON I POTKURVEN              *
%*****************************************************************
load potensialkurvedata %denne datafila inneholder pot. punkter
R=potensialkurvedata(1:end,1);
E1=potensialkurvedata(1:end,2); % singlet grundtilstand
E1=(E1-1.0719909);
b=(a-R(1))/N;
xi=R;
yi=E1;

%xi=[R(1):b:R(length(R))+b];
%yi2=interp1(R,E1,xi,'cubic');
%p1=polyfit(R,E1,10);
%yi=polyval(p1,xi);
%plot(xi,yi);

p=floor((R(length(R))-R(1))/b);
a0=R(1)+(p+1)*b;
x=[a0:b:a];
C6=1388*27.2114;
C8=83230*27.2114;
C10=7348000*27.2114;
```

```
V=-C6./x.^6-C8./x.^8-C10./x.^10-0*0.01288*(x.^(4.558)).*exp(-1.259.*x);
%plot(r,V); %Kontrollplot
r2=[R(1):b:p*b+R(1)];
p1=polyfit(R,E1,9);
yi=polyval(p1,r2);
%yi=interp1(R,E1,r2,'spline');
lengde=length(V)+length(yi);
EPOT=ones(1,lengde);
j=1;
beta=length(yi);
for i=1:lengde
    if(i<=beta)
       EPOT(1,i)=yi(i);
    else
       EPOT(1,i)=V(j);
       j=j+1;
    end
end
r=[R(1):b:a];
%plot(r,EPOT)
%yi=interp1(R,EPOT(1,:),r,'spline');
for q=1:N
    middelpot(1,q)=0.5*(EPOT(q)+EPOT(q+1));
    middx(1,q)=R(1)+b/2+(q-1)*b;
end
plot(middx(1,:),middelpot(1,:))
%*****************************************************************
%         UTREGNING alpha, 2X MMATRISE OG WMATRISER               *
%*****************************************************************
for j=1:N
    if(k^2>=(FAC*middelpot(1,j)))
        alpha(1,j)=sqrt(k^2-FAC*middelpot(1,j));
    else
        alpha(1,j)=sqrt(FAC*middelpot(1,j)-k^2);
    end
end

% Opprettelse av matriser og vektorer
KNY=eye(2);
K=eye(2);
faseskift=ones(1,N);
faseskift(1,1)=0;
teller=0;
if(k^2>=(FAC*middelpot(1,1)))
    s=0;
else
    s=1;
```

```
end

M2=MMATRISE(R(1)+b,alpha(1,1),l,0,s);

% Utregninger og multiplikasjon av K-matriser
for i=2 : N
    x=1/(i*b*alpha(1,i));
    y=1/((i-1)*b*alpha(1,i));
    sigma=b*alpha(1,i);
    if(k^2>=(FAC*middelpot(1,i)))
       KNY(1,1)=(i-1)^2*b^2*alpha(1,i)^2*((-POL(x,l)*POLSTREK(y,l)
                -QOL(x,l)*QOLSTREK(y,l))*sin(sigma)+(POL(x,l)
                *QOLSTREK(y,l)-QOL(x,l) *POLSTREK(y,l))*cos(sigma));
       KNY(1,2)=(i-1)^2*b^2*alpha(1,i)*((POL(x,l)*POL(y,l)+QOL(x,l)
                *QOL(y,l))*sin(sigma)+(-POL(x,l)*QOL(y,l)+QOL(x,l)
                *POL(y,l))*cos(sigma));
       KNY(2,1)=(i-1)^2*b^2*alpha(1,i)^3*((-POLSTREK(x,l)*POLSTREK(y,l)-
                QOLSTREK(x,l)*QOLSTREK(y,l))*sin(sigma)+(POLSTREK(x,l)
                *QOLSTREK(y,l)-QOLSTREK(x,l)*POLSTREK(y,l))*cos(sigma));
       KNY(2,2)=(i-1)^2*b^2*alpha(1,i)^2*((POLSTREK(x,l)*POL(y,l)
                +QOLSTREK(x,l)*QOL(y,l))*sin(sigma)+(-POLSTREK(x,l)
                *QOL(y,l)+QOLSTREK(x,l)*POL(y,l))*cos(sigma));
    else
       KNY(1,1)=(-1)^l*(i-1)^2*b^2*alpha(1,i)^2*((-POLTILDE(x,l)
                *POLTILDESTREK(y,l)+QOLTILDE(x,l)*QOLTILDESTREK(y,l))
                *sinh(sigma)+(POLTILDE(x,l)*QOLTILDESTREK(y,l)
                -QOLTILDE(x,l)*POLTILDESTREK(y,l))*cosh(sigma));
       KNY(1,2)=(-1)^l*(i-1)^2*b^2*alpha(1,i)*((POLTILDESTREK(x,l)
                *POLTILDESTREK(y,l)-QOLTILDESTREK(x,l)*QOLTILDESTREK(y,l))
                *sinh(sigma)+(-POLTILDESTREK(x,l)*QOLTILDESTREK(y,l)+
                QOLTILDESTREK(x,l)*POLTILDESTREK(y,l))*cosh(sigma));
       KNY(2,1)=(-1)^l*(i-1)^2*b^2*alpha(1,i)^3*((-POLTILDESTREK(x,l)
                *POLTILDE(y,l)+QOLTILDESTREK(x,l)*QOLTILDE(y,l))
                *sinh(sigma)+(POLTILDESTREK(x,l)*QOLTILDE(y,l)
                -QOLTILDESTREK(x,l)*POLTILDE(y,l))*cosh(sigma));
       KNY(2,2)=(-1)^l*(i-1)^2*b^2*alpha(1,i)^2*((POLTILDE(x,l)
                *POLTILDE(y,l)-QOLTILDE(x,l)*QOLTILDE(y,l))
                *sinh(sigma)+(-POLTILDE(x,l)*QOLTILDE(y,l)
                +QOLTILDE(x,l)*POLTILDE(y,l))*cosh(sigma));
    end

    K=KNY*K;
    M1=MMATRISE(R(1)+i*b,k,l,1,0);
    FASESKIFT= M1*(K*M2);
    delta=- FASESKIFT(2,1)/FASESKIFT(1,1);
    faseskift(1,i)=atan(delta);
```

```
    if(faseskift(1,i)<faseskift(1,i-1))
        teller=teller+1; %teller brukes hvis faseskift ikke mod pi ønskes.
    end
end %avslutter for løkka

M1=MMATRISE(a,k,l,1,0);
FASESKIFT= M1*(K*M2);
delta=-(FASESKIFT(2,1)/FASESKIFT(1,1));
faseskiften=pi*teller+atan(delta);

a1=(1/(-k*cot(faseskiften)+0.5*0*66*k^2))
```

Listing of the function MMATRISE that can be used to calculate any M or M^{-1} for both real and imaginary α's and for all l values. The function must be called with input parameters position r, wavevector k, partial wave l together with two parameters i and s. i controls calculation of $M(i=0)$ or $M^{-1}(i=1)$. $s=0$ if α is real, and $s=1$ if α is complex.

```
function MAT=MMATRISE(r,k,l,i,s)
%r er posisjon, k er alpha, l er partial bølgen, i tar verdiene 0 og
%1 avhengig av hva man ønsker. 1 for å kalkulere inverse M matrisa.
%0 for M matrisa. s =0 hvis k^2>~FAC*midpoint og s=1 hvis motsatt.

x=1/(r*k);
M=eye(2);

if(s==0)
    if(i==0)
     M(1,1)=sin(k*r)*POL(x,l)+cos(k*r)*QOL(x,l);
     M(1,2)=sin(k*r)*QOL(x,l)-cos(k*r)*POL(x,l);
     M(2,1)=sin(k*r)*k*POLSTREK(x,l)+cos(k*r)*k*QOLSTREK(x,l);
     M(2,2)=sin(k*r)*k*QOLSTREK(x,l)-cos(k*r)*k*POLSTREK(x,l);
    else
     M(1,1)=k*r^2*(sin(k*r)*k*QOLSTREK(x,l)-cos(k*r)*k*POLSTREK(x,l));
     M(1,2)=k*r^2*(-sin(k*r)*QOL(x,l)+cos(k*r)*POL(x,l));
     M(2,1)=k*r^2*(-sin(k*r)*k*POLSTREK(x,l)-k*cos(k*r)*QOLSTREK(x,l));
     M(2,2)=k*r^2*(sin(k*r)*POL(x,l)+cos(k*r)*QOL(x,l));
    end
else
    if(i==0)
     M(1,1)=(complex(0,1))^l*(sinh(k*r)*POLTILDE(x,l)+cosh(k*r)
            *QOLTILDE(x,l));
     M(1,2)=(complex(0,1))^l*(sinh(k*r)*complex(0,1)
            *QOLTILDE(x,l)+cosh(k*r)*complex(0,1)*POLTILDE(x,l));
     M(2,1)=(complex(0,1))^l*(sinh(k*r)*k*POLTILDESTREK(x,l)+cosh(k*r)
            *k*QOLTILDESTREK(x,l));
     M(2,2)=(complex(0,1))^l*(sinh(k*r)*k*complex(0,1)*QOLTILDESTREK(x,l)
            +cosh(k*r)*k*complex(0,1)*POLTILDESTREK(x,l));
    else
```

```
     M(1,1)=(complex(0,1))^(l+1)*k*r^2*(sinh(k*r)*k*QOLTILDESTREK(x,l)
            *complex(0,1)+cosh(k*r)*k*complex(0,1)*POLTILDESTREK(x,l));
     M(1,2)=(complex(0,1))^(l+1)*k*r^2*(-sinh(k*r)*QOLTILDE(x,l)
            *complex(0,1)-cosh(k*r)*complex(0,1)*POLTILDE(x,l));
     M(2,1)=(complex(0,1))^(l+1)*k*r^2*(-sinh(k*r)*k
            *POLTILDESTREK(x,l)-k*cosh(k*r)*QOLTILDESTREK(x,l));
     M(2,2)=(complex(0,1))^(l+1)*k*r^2*(sinh(k*r)*POLTILDE(x)
            +cosh(k*r)*QOLTILDE(x,l));
    end
end
MAT=M;
```

Function for calculating $P_l(x)$

```
function P=POL(x,l)

f0=x;
f=f0;
if (l>0)
f1=x*x;
f=f1;
end
if (l>1)
    for j=2:l
        f1=f;
        f=(2*j-1)*f1*x-f0;
        f0=f1;
    end
end
P=f;
```

Function for calculating $Q_l(x)$

```
function Q=QOL(x,l)
f0=0;
f=f0;
if (l>0)
    f1=-x;
    f=f1;
end
if (l>1)
    for j=2:l
        f1=f;
        f=(2*j-1)*f1*x-f0;
        f0=f1;
    end
end
Q=f;
```

Function for calculating $\bar{P}_(x)$

```
function PSTREK=POLSTREK(x,l)
if (l==0)
  f=-POL(x,1);
else
  f=(l*POL(x,l-1)-(l+1)*POL(x,l+1))/(2*l+1);
end
PSTREK=f;
```

Function for calculating $\bar{Q}_(x)$

```
function QSTREK=QOLSTREK(x,l)
if (l==0)
  f=-QOL(x,1);
else
  f=(l*QOL(x,(l-1))-(l+1)*QOL(x,l+1))/(2*l+1);
end
QSTREK=f;
```

Function for calculating $\tilde{P}_l(x)$

```
function PTILDE=POLTILDE(x,l)
PTILDE=complex(0,1)^(1-l)*POL(-complex(0,1)*x, l);
```

Function for calculating $\tilde{Q}_l(x)$

```
function QTILDE=QOLTILDE(x,l)
QTILDE=complex(0,1)^(-l)*QOL(-complex(0,1)*x,l);
```

Function for calculating $\bar{\tilde{P}}_l(x)$

```
function PTILDESTREK=POLTILDESTREK(x,l)
if (l==0)
  f=POLTILDE(x,1);
else
  f=(l*POLTILDE(x,l-1)+(l+1)*POLTILDE(x,l+1))/(2*l+1);
end
PTILDESTREK=f;
```

Finally, function for calculating $\bar{\tilde{Q}}_l(x)$

```
function PTILDESTREK=POLTILDESTREK(x,l)
if (l==0)
  f=POLTILDE(x,1);
else
  f=(l*POLTILDE(x,l-1)+(l+1)*POLTILDE(x,l+1))/(2*l+1);
end
PTILDESTREK=f;
```

Appendix D

Condensation temperature T_C

We assume an ideal Bose-Einstein gas. The number of atoms are given by the integral over the density of states $g(E)$ times the Bose-Einstein distribution,

$$N = \int_0^\infty g(E) \frac{1}{e^{(E-\mu)/(k_B T)} - 1} \mathrm{d}E. \tag{D.1}$$

To find T_C we put $\mu = 0$, and use $g(E) = \frac{2}{\sqrt{\pi}} \left(\frac{2\pi m}{h^2}\right)^{3/2} V\sqrt{E}$. m is particle mass and V is volume.

$$N = \frac{2}{\sqrt{\pi}} \left(\frac{2\pi m}{h^2}\right)^{3/2} V \int_0^\infty \frac{\sqrt{E}}{e^{E/k_B T_C} - 1} \mathrm{d}E = \frac{2}{\sqrt{\pi}} \left(\frac{2\pi m k_B T_C}{h^2}\right) V \underbrace{\int_0^\infty \frac{\sqrt{x}}{e^x - 1} \mathrm{d}x}_{=2.315}. \tag{D.2}$$

Thus we find

$$N = 2.612 \left(\frac{2\pi m k_B T_C}{h^2}\right)^{3/2} V \Leftrightarrow T_C = \frac{1}{k_B} 0.527 \left(\frac{h^2}{2\pi m}\right) \left(\frac{N}{V}\right)^{2/3} \tag{D.3}$$

Below T_C there is an accumulation of atoms in the lowest level. For a much more thorough treatment, see Finn Ravndal: *Lecture notes on Statistical Physics, 2003*. Available at http://www.fys.uio.no/ flekkoy/fys3130/kompendium.pdf.

Bibliography

[1] L. D. Landau and E. M. Lifshitz. "Quantum Mechanics." Elsevier Ltd. (1977).

[2] C. J. Foot. *Atomic Physics*. Oxford University Press, (2004).

[3] H. J. Metcalf and P. van der Straten. *Laser Cooling and Trapping*. Springer-Verlag, (1999).

[4] P. Lett, R. Watts, C. Westbrook, W. Phillips, P. Gould and H. Metcalf. "Observation of Atoms Laser Cooled below the Doppler Limit." Phys. Rev. Lett. **61**, 169 (1988).

[5] J. Dalibard and C. Cohen-Tannoudji. "Laser Cooling Below the Doppler Limit by Polarization Gradients - Simple Theoretical-Models." J. Opt. Soc. Am. B **6**, 2023 (1989).

[6] K. B. Davis, M. O. Mewes, W. Ketterle. "An analytical model for evaporative cooling of atoms. App. Phys. B **60**, 155-159 (1995).

[7] V. Bagnato, D. E. Pritchard and D. Kleppner. "Bose-Einstein Condensation in an External Potential." Phys. Rev. A **35**, 4354 (1987).

[8] M. H. Andersen, J. R. Ensher, M. R. Matthews, C. E. Wieman and E. A. Cornell. "Observation of Bose-Einstein Condensation in Dilute Atomic Vapor." Science **269**, 198 (1995)

[9] R. deCarvalho, J. M. Doyle, B. Friedrich, T. Guillet, J. Kim, D. Patterson and J. D. Weinstein. *Buffer-gas loaded magnetic traps for atoms and molecules: A primer*. The European Phyiscal Journal D **7**, 289 (1999).

[10] V. Vuletic and S. Chu. "Laser cooling of atoms, ions or molecules by coherent scattering." Phys. Rev. Lett. **84**, 3787 (2000).

[11] R. Wynar, R. S. Freeland, D. J. Han, C. Ryu and D. J. Heinzen. "Molecules in a Bose-Einstein condensate." Science **287**, 1016 (2000).

[12] A. J. Kerman, J. M. Sage, S. Sainis, T. Bergeman and D. DeMille. "Producion and state-selective detection of ultracold RbCs molecules." Phys. Rev. Lett **92**, 153001 (2004).

[13] C. A. Regal, C. Ticknor, J. L. Bohn and D. S. Jin. "Creation of ultracold molecules from a Fermi gas of atoms." Nature **424**, 47 (2003).

[14] J. D. Weinstein, R. deCarvalho, T. Guillet, B. Friedrich and J. M. Doyle. "Magnetic trapping of calcium monohydride molecules at millikelvin temperatures." Nature **395** 148 (1998).

[15] D. Egorov, J. D. Weinstein, D. Patterson, B. Friedrich and J. M. Doyle. "Spectroscopy of laser-ablated buffer-gas-cooled PbO at 4K and the prospects for measuring the electric dipole moment of the electron." Phys. Rev. A **63**, R030501 (2001)

[16] M. R. Tarbutt, H. L. Bethlem, J. J. Hudson, V. K. Ryabov, V. A. Ryzhov, B. E. Sauer, G. Meijer and E. A. Hinds. "Slowing heavy, ground-state molecules using an alternating gradient decelerator." Phys. Rev. Lett **92**, 173002 (2004).

[17] E. Nikitin, E. Dashveskaya, J. Alnis, M. Auzinsh, E. R. I. Abraham, B. R. Furneaux, M. Keil, C. McRaven, N. Shafer-Ray, R. Waskowsky. "Measurement and prediction of the speed-dependent throughput of a magnetic octupole velocity filter including nonadiabatic effects." Phys. Rev. A **68**, 023403 (2003).

[18] M. S. Elioff, J. J. Valentini, D. W. Chandler. "Subkelvin Cooling NO "Molecules via "Billiard like" Collisions with Argon." Science **302**, 1940 (2003).

[19] K. Xu, T. Mukaiyama, J. R. Abo-Shaeer, J. K. Chin, D. E. Miller and W. Ketterle. "Formation of Quantum-Degenerate Sodium Molecules." Phys. Rev. Lett **91**, 210402 (2003).

[20] M. W. Mancini, G. D. Telles, A. R. L. Caires, V. S. Bagnato and L. G. Marcassa. "Observation of Ultracold Ground-State Heteronuclear Molecules." Phys. Rev. Lett **92**, 133203 (2004).

[21] P. Sannes. Cand. scient thesis :*Et program for beregning av elektroniske energinivåer i atomer og toatomige molekyler basert på perturbasjonsteori for generelle modellrom.* (1996).

[22] U. Kaldor. *Many-Body methods in Quantum Chemistry.* Springer (1989).

[23] G. Hose. "Multireference-state Rayleigh-Scrödinger perturbation theory applied to the electronic states $X^1\Sigma_g^+$ and EF $^1\Sigma_g^+$ of H_2." J. Chem. Phys. **84**, 4505 (1986).

[24] G. Hose and U. Kaldor "Diagrammatic many-body perturbation theory for general model spaces." J. Phys. B, **12**, 3827 (1979)

[25] G. Hose and U. Kaldor "A general-model-space diagrammatic many-body perturbation theory." Phys. Scr. **21**, 357 (1980)

[26] G. Hose and U. Kaldor. "Quasidegenerate perturbation theory." J. Phys. Chem. **86**, 2133 (1982).

[27] L. Veseth. Compendium: "Forelesninger i molekylarfysikk." (1975)

[28] C. C. J. Roothan. "Self-Consistent Field Theory for Open Shells of Electronic Systems." Rev. Mod. Phys. **32**, 179 (1960).

[29] K. Fægri, Jr. and R. Manne. "A new procedure for Roothan's symmetri restricted open-shell SCF-method." Mol. Phys. **31**, 1037 (1976).

[30] E. Clementi and C. Roetti. *Atomic data and nuclear data tables.* **14**, Number 3-4 (1974).

[31] A. Szabo and N. S. Ostlund. *Modern Quantum Chemistry: Introduction to Advanced Electronic Structure Theory.* Macmillan Publishing Co (1982).

[32] M. Born and R. Oppenheimer. Ann. Phys. **84**, 457 (1927).

[33] Torsheim H. R, J. Weiner and P. S. Julienne. "Laser-induced photoassociation of ultracold sodium atoms." Phys. Rev. Lett. **58**, 2420 (1987).

[34] J. M. Leinaas. "Non Relativistic Quantum Mechanics." Lecture notes for FYS4110, (2004). Available at *http://www.uio.no/studier/emner/matnat/fys/FYS4110/h05/ undervisningsmateriale/LectureNotes.pdf*

[35] A. N. Nikolov, E. E. Eyler, X. T. Wang, J. Li, H. Wang, W. C. Stwalley and P. L. Gould. "Observation of Ultracold Ground-State Potassium Molecules." Phys. Rev. Lett. **82**, 703 (1999).

[36] J. T. Bahns, P. L. Gould and W. C. Stwalley. "Formation of cold molecules." Adv. in atomic, molecular and opitcal physics **42**, 171 (2000).

[37] R. Napolitano, J. Weiner, C. J. Williams and P. S. Julienne. "Line shapes of high resolution photoassociation spectra of optically cooled atoms." Phys. Rev. Lett **73**, 1352 (1994).

[38] Y. B. Band and P. S. Julienne. "Ultracold-molecule production by laser-cooled atom photoassociation." Phys. Rev. A. **51**, R4317 (1995).

[39] D. D. Konowalow and J. L. Fish. "Long range interactions of $\mathrm{Li}(n = 2)$ states with each other and the long-range interaction of $\mathrm{Li}(2s^2S)$ with $\mathrm{Li}(3s^2S)$." Chem. Phys **77**, 435 (1983).

[40] D. D. Konowalow and J. Fish. "The molecular electronic structure of the twenty six lowest lying states of Li_2 at short and intermediate internuclear separation." Chem. Phys. **84**, 463 (1984).

[41] L. B. Ratcliff, J. L. Fish, D. D. Konowalow. "Electronic Transition Dipole Moment Functions for Transitions among the Twenty-Six Lowest-Lying States of Li_2." Journal of molecular spectroscopy **122**, 293 (1987).

[42] "Observation and analysis of the $A^1\Sigma_u^+$ state of $^6\mathrm{Li}_2$ from $v = 0$ to the dissociation limit." Journal of molecular spectroscopy, **175**, 340 (1996).

[43] R. Côté and A. Dalgarno. "Mechanism for the Production of $^6\mathrm{Li}_2$ and $^7\mathrm{Li}_2$ Ultracold Molecules." Journal of Molecular Spectroscopy **195**, 236 (1999).

[44] R. Côté and A. Dalgarno. "Photoassociation intensities and radiative trap loss in lithium." Phys. Rev. A **58**, 498 (1998).

[45] T. M. Kalotas and A. R. Lee. "A new approach to one-dimensonial scattering." Am. J. Phys **59**, 48 (1990).

[46] Abraham E. R. I., W. I. McAlexander, J. M. Gerton and R. G. Hulet. "Triplet s-wave resonance in $^6\mathrm{Li}$ collisions and scattering lengths of $^6\mathrm{Li}$ and $^7\mathrm{Li}$." Phys. Rev. A, **55** R3299, 1997.

[47] L.P.Pitaevskii and S.Stringari. *Bose-Einstein condensation in dilute gases*. Oxford University Press, (2003).

[48] R. Côte, A. Dalgarno and M. J. Jamieson. "Elastic scattering of two ^{7}Li atoms." Phys. Rev. A **50**, 399 (1994).

[49] R. Côte and A. Dalgarno. "Elastic scattering of two Na atoms." Phys. Rev. A **50**, 4827 (1994).

[50] Unknown author. "Dispersion coefficients for alkali-metal dimers". http://cfa-www.harvard.edu/dvrinceanu/Mircea/AlkaliMetal.html.

[51] T. M. Kalotas, A. R. Lee and V. E. Howard. "Exact partial wave analysis for scattering by a segmented potential". Am. J. Phys. **59**, 225 (1991).

[52] G. F. Gribakin and V. V. Flambaum. "Calculation of the scattering length in atomic collisions using the semiclassical approximation". Phys. Rev. A **48**, 546(1993).

[53] E. R. I. Abraham, W. I. McAlexander, J. M. Gerton, R. G. Hulet,R. Côte and A. Dalgarno. "Singlet s-wave scattering lengths of ^{6}Li and ^{7}Li. Phys. Rev. A **53**, R3713 (1996).

[54] C. J. Joachain. *Quantum Collision Theory* (North-Holland Publishing Company, 1975.) Chapter 4, Chapter 11 and Appendix B.

[55] P. C. Hemmer. *Kvantemekanikk* (Tapir akademisk forlag, 2000.)

[56] R. Shankar. *Principles of Quantum Mechanics* (Plenum Press,1980, 1994.)

[57] Riley, Hobson and Bence. *Mathematical methods for physics and engineering* (Cambridge University Press 1998.)

[58] J. M. Blatt and J. D. Jackson. *On the Interpretation of Neutron-Proton Scattering Data by the Schwinger Variational Method*. Phys.Rev **76**, 18 (1949).

[59] B. H. Bransden and C. J. Joachain. *Physics of Atoms and Molecules*. (Pearson Education Limited, 1983, 2003.) *Bose-Einstein condensation in dilute gases*. Oxford University Press, (2003).

[60] J. L. Bohn and P. S. Julienne. "Semianalytic theory of laser-assisted resonant cold collisions." Phys. Rev. A **60**, 414 (1999).

[61] S. L. Cornish, N. R. Claussen, J. L. Roberts, E. A. Cornell and C. E. Wieman. "Stable ^{85}Rb Bose-Einstein Condensates with Widely Tunable Interactions." Phys. Rev. Lett. **85**, 1795 (2000).

[62] A. J. Moerdijk, B. J. Verhaar and A. Axelsson. "Resonances in ultracold collisions of ^{6}Li,^{7} Li, and ^{23}Na. Phys. Rev. A **51**, 4852 (1995).

[63] Cindy A. Regal, Christopher Ticknor, John L. Bohn and Deborah S. Jin. "Creation of ultracold molecules from a Fermi gas of atoms." Nature **423**, 47 (2003).

[64] J. Cubizolles, T. Bourdel, S. J. J. M. F. Kokkelmans, G. V. Shlyapnikov and C. Salomon. "Production of Long-Lived Ultracold Li_2 Molecules from a Fermi gas." Phys. Rev. Lett. **91**, 240401 (2003).

[65] E. Tiesinga, B. J. Verhaar and H. T. C. Stoof. " Threshold and resonance phenomena in ultracold ground-state collisions." Phys. Rev. A **47**, 4114 (1993).

[66] P. Nozieres and S. Schmitt-Rink. "Bose Condensation in an Attractive Fermion Gas: From Weak to Strong Coupling Superconductivity." J. Low-Temp. Phys. **59**, 195 (1985).

[67] M. Randeria, *Bose-Einstein Condensation*. Cambridge Univ., (1995), pages 355-392.

[68] M. Marini, F. Pistolesi and G. C. Strinati. "Evolution from BCS superconductivity to Bose condensation: Analytic results for the crossover in three dimensions. Eur. Phys. J. B **1**, 151 (1998).

[69] S. Jochim, M. Bartenstein, A. Altmeyer, G. Hendl, S. Riedl, C. Chin, J. Hecker Deschlag and R. Grimm. "Bose-Einstein Condensation of Molecules". Science **302**, 2101 (2003).

[70] Markus Greiner, Cindy A. Regal and Deborah S. Jin. "Emergence of a molecular Bose-Einstein condensate from a Fermi gas". Nature **426**, 537 (2003).

[71] M. W. Zwierlein, C. A. Stan, C. H. Schunck, S. M. F. Raupach, S. Gupta, Z. Hadzibabic and W. Ketterle. "Observation of Bose-Einstein Condensation of Molecules". Phys. Rev. Lett **91**, 250041 (2003).

[72] D. S. Petrov, C. Salomon and G. V. Shlyapnikov. Preprint available at http://arxiv.org/abs/cond-mat/0309010.

[73] Golubitsky and Dellnitz. *Linear Algebra and Differential Equations*. Brooks/Cole Publishing Company, 1999.

[74] C. C. Bradley, C. A. Sackett, J. J. Tollett and R. G. Hulet. "Evidence of Bose-Einstein Condensation in an Atomic Gas with Attractive Interactions." Phys. Rev. Lett. **75**, 1687 (1995).

[75] C. A. Sackett, J. M. Gerton, M. Welling and R. G. Hulet. "Measurements of Collective Collapse in a Bose-Einstein Condensate with Attractive Interactions." Phys. Rev. Lett. **82**, 876 (1999).

[76] J. Carlson, S. Y. Chang, V. R. Pandharipande and K. E. Schmidt. "Superfluid Fermi gases with large scattering length." Phys. Rev. Lett. **91**, 050401 (2003)

[77] G. E. Astrakharchik, J. Boronat, J. Casulleras and S. Giorgini. "Equation of state of a Fermi gas in the BEC-BCS crossover: A quantum Monte Carlo study." Phys. Rev. Lett **93**, 200404 (2004).

[78] P. Kristiansen and L. Veseth. "Many body calculations of hyperfine constants in diatomic molecules." J. Chem. Phys. **84**(5), 2711 (1986).

[79] T. Bourdel, J. Cubizolles, K. Khaykovich, K. M. F. Magalhães, S. J. J. M. F. Kokkelmans, G. V. Shlapnikov and C. Salomon. "Measurement of the interaction energy near a Feshbach resonance in a ^{6}Li Fermi Gas." Phys. Rev. Lett. **91**, 020402 (2003).